

**Modeling struvite precipitation in a batch reactor using a population balance
model in a 3-D computational fluid dynamic (CFD) framework**

Seyyed Ebrahim Mousavi

A Thesis

In

The Department of

Building, Civil and Environmental Engineering

Presented in partial fulfillment of the requirement
For the Degree of Master of Applied Science (Civil Engineering) at
Concordia University
Montreal, Quebec, Canada.

March 2017

© Seyyed Ebrahim Mousavi, 2017

CONCORDIA UNIVERSITY
School of Graduate Studies

This is to certify that the thesis prepared

By: Seyyed Ebrahim Mousavi

Entitled: Modeling struvite precipitation in a batch reactor using a population balance model in a 3-D computational fluid dynamic (CFD) framework

and submitted in partial fulfillment of the requirements for the degree of

Master of Applied Science (Civil Engineering)

complies with the regulations of the University and meets the accepted standards with respect to originality and quality.

Signed by the final Examining Committee:

Dr. S. SAMUEL LI	Chair
Dr. MEHDI HOJJATI	Examiner
Dr. AMRUTHUR S. RAMAMURTHY	Examiner
Dr. SAIFUR RAHAMAN	Supervisor

Approved by _____

Date _____

Abstract

Modeling struvite precipitation in a batch reactor using a population balance model in a 3-D computational fluid dynamic (CFD) framework

Seyyed Ebrahim Mousavi

Discharge of significant amounts of phosphate from nutrient-rich wastewater is problematic considering the potential risk for contamination of groundwater and eutrophication of recipient water bodies. On the other hand, phosphorus is a limited, non-renewable resource with total reserves that may be depleted in the near future. As a result, phosphorus recovery is receiving increased attention as an environmental concern. The recovery of phosphorus using a precipitation technique is one proven solution for this issue. In this work, the precipitation of Magnesium Ammonium Phosphate (Struvite) as an alternative method for the recovery of phosphorous is modeled in a batch stirred tank reactor. The aim of this work is to link Computational Fluid Dynamics (CFD) with Population Balance Modeling (PBM) to develop a 3-D CFD model that can predict the Crystal Size Distribution (CSD) of struvite. In the simulation, the CFD flow field was solved through a Eulerian multiphase approach and RNG k- ϵ turbulence model, using a commercial CFD package, ANSYS Fluent 17.1. The population balance equation was solved using the discrete method, implementing 25 different size classes. The size-independent growth rate as a function of the supersaturation index (SI) was employed in the model through User Defined Function (UDF). A series of experiments were conducted utilizing synthetic wastewater in a stirred tank reactor agitated with a Rushton impeller to confirm the simulation results. The model successfully predicted the variation in crystal size distribution as well as SI values over the experiment time period.

ACKNOWLEDGMENTS

I owe my deepest gratitude to my supervisor, Dr. Saifur Rahaman, for granting me an opportunity to pursue my graduate studies at Concordia University. I really appreciate his motivation, enthusiasm, immense knowledge, and his patience reviewing my writing. I would definitely have not reached this point without his support and encouragement. It was a privilege to work with such an extraordinary and patient supervisor like him.

DEDICATION

This thesis work is dedicated to my lovely wife, Somayeh, for her love and encouragement during the challenges of this work and over our whole life together. It is really fortunate to have someone who believes in you more than yourself.

This work is also dedicated to my parents who stood by my side with their spiritual support.

Table of Contents

Table of Contents	v
List of Figures	vii
List of Tables	ix
NOMENCLATURE	x
1. INTRODUCTION	1
1.1 Motivation	1
1.2 Phosphorous recovery	1
1.3 What is Struvite?	2
1.4 Struvite as a Fertilizer	3
1.5 Methods for struvite recovery	4
1.5.1 Electrochemical method.....	4
1.5.2 Ion exchange method	4
1.5.3 Biomineralisation method.....	5
1.5.4 Chemical precipitation method.....	5
1.6 Research Objectives	6
2 LITERATURE REVIEW	7
2.1 Hydrodynamic-oriented models.....	7
2.2 Thermodynamic-oriented models	9
2.3 Kinetic-oriented models	12
3 MATERIALS AND METHODS	14
3.1 Experimental Works.....	14
3.1.1 Introduction.....	14
3.1.2 Solubility Curve and Metastable Zone	14
3.1.3 Experimental setup.....	19
3.1.4 Materials	20
3.1.5 Seed Preparation	20
3.1.6 Measurements	21
3.1.6.1 Crystal Size Distribution Measurement	21
3.1.6.2 pH Measurement	23
3.1.7 Experimental procedure	23
3.2 Numerical Simulation	24

3.2.1	Introduction.....	24
3.2.2	Governing Equation.....	24
3.2.2.1	Two phase flow.....	24
3.2.2.2	Continuity Equation.....	25
3.2.2.3	Momentum equation.....	25
3.2.2.4	Interface momentum exchange.....	26
3.2.2.5	Turbulence modeling – RNG k- ϵ model.....	28
3.2.2.6	Species transport equation.....	29
3.2.3	Model Development.....	29
3.2.3.1	Reactor Geometry.....	29
3.2.3.2	Impeller rotation modeling.....	30
3.2.4	Method of solution.....	31
3.3	CFD-PBM Coupling Theory and Implementation.....	34
3.3.1	Introduction.....	34
3.3.2	Governing Equations.....	36
3.3.3	Precipitation Kinetics: previews works.....	37
3.3.4	Growth rate.....	39
3.3.5	Implementation of PBM in Fluent.....	39
4	RESULTS AND DISCUSSION.....	41
4.1	Grid sensitivity results.....	41
4.2	Flow Pattern Prediction.....	41
4.2.1	Power Number Prediction.....	42
4.2.2	Overall Flow Pattern.....	44
4.2.3	Velocity Magnitude Distribution.....	46
4.3	Supersaturation Prediction.....	46
4.4	Crystal Size Distribution (CSD).....	50
4.5	Average Crystal Size.....	56
5	CONCLUSIONS AND RECOMMENDATIONS FOR FUTURE WORKS.....	57
6	REFERENCES.....	59
	Appendices.....	64

List of Figures

Figure 1 Determination of different saturation state zones for Struvite	18
Figure 2 Photographic (A) and Schematic (B) view of crystallizer.....	19
Figure 3 Number-based Crystal Size Distribution of seeds, (A) random samples and (B) average used in the CFD model	21
Figure 4 Photographic view of particle size analyzer	22
Figure 5 Schematic view of the reactor geometry and impeller used for this study.....	30
Figure 6 3D Schematic view of the reactor domain showing MRF zone.....	31
Figure 7 Three different positions selected for comparing liquid phase velocity, A: near the top, B near the tip of impeller, and C near the reactor bottom.....	34
Figure 8 Schematic diagram of Multiphase CFD-PBM model	36
Figure 9 Comparison of experimental and CFD model (single phase and multiphase) predicted impeller power number	43
Figure 10 Comparison of (A) experimental results by Costes and Couderc [105] flow pattern with (B) flow pattern prediction obtained by the CFD model for a vertical plane containing a baffle($\theta = 0^\circ$).....	44
Figure 11 Comparison of (A) experimental results by Costes and Couderc [105] flow pattern with (B) flow pattern prediction obtained by the CFD model for a vertical plane between baffles($\theta = 45^\circ$).....	45
Figure 12 Velocity contours on a horizontal plane at the middle of impeller	46
Figure 13 pH and SI variation with time for different initial conditions experiments	48
Figure 14 Experimental pH variation with the time	49
Figure 15 Experimental and CFD model predicted Supersaturation index	50
Figure 16 Experimental averaged and CFD model predicted CSD at time = 0 (seed) - Number based distribution.....	51
Figure 17 Experimental average and CFD model predicted CSD at time = 3min - Number based distribution.....	51
Figure 18 Experimental averaged and CFD model predicted CSD at time = 10 min - Number based distribution.....	52
Figure 19 Experimental averaged and CFD model predicted CSD at time = 20 min - Number based distribution.....	52

Figure 20 Experimental averaged and CFD model predicted CSD at time = 30 min - Number based distribution	53
Figure 21 Experimental averaged and CFD model predicted CSD at time = 40 min - Number based distribution	53
Figure 22 Experimental averaged and CFD model predicted CSD at time = 50 min - Number based distribution	54
Figure 23 Experimental averaged and CFD model predicted CSD at time = 60 min - Number based distribution	54
Figure 24 Experimental and CFD predicted crystal size results – number fraction weighted average size	56

List of Tables

Table 1 SEM of different struvite crystal shapes.....	3
Table 2 Equilibrium Constant for complexes	15
Table 3 Initial concentration and pH of the experiments.....	23
Table 4 Different Applied Grids and Number of Cells.....	33
Table 5 Recent studies related to Precipitation kinetic and predicted coefficients.....	38
Table 6 List of selected bins and related diameters	40
Table 7 Results of grid independency.....	41

NOMENCLATURE

List of Abbreviations

CFD	Computational Fluid Dynamic
CSD	crystal size distribution
DDT	Double Draft Tube
DI water	Di-ionized water
DTM	Draft Tube Magma
FL	Fluidized bed
IAP	Ion Activity Product
LD	Laser diffraction
LDV	Laser Doppler Velocimetry
MAP	magnesium ammonium phosphate
MRF	Multiple Reference Frame
PBE	Population Balance Equation
PBM	Population Balance Model
PDF	Probability Density Function
Re	Reynolds Number
RNG	Renormalized group
RPM	Revolutions Per Minute
Sc	Schmidt number
SEM	Scanning Electron Microscope
SI	Supersaturation Index

SM	Sliding Mesh
TUI	Text user interface
UDF	User Defined Function
UN	United Nations

List of Symbols

A	Debye-Huckel constant
$a(V, V')$	Aggregation kernel (m^3/s)
B_{agr}	Birth rate due to aggregation
B_{brk}	Birth rate due to breakage
C_i	Ionic concentration
C_D	Drag coefficient
$C_{1\varepsilon}$	Constant
$C_{2\varepsilon}$	Constant
C_μ	Constant
$\{C_i\}$	Ion activity of ion C_i
D	Diameter (m)
D_{agr}	Death rate due to aggregation
D_{brk}	Death rate due to breakage
D_m	Molecular diffusion
D_t	Turbulent diffusivity
d_j	Diameter of solid particles
d_{32}	Sauter mean diameter (m)

\vec{F}_i	Centrifugal forces
f	Drag function
$G_{k,m}$	Generation of turbulent kinetic energy
\vec{g}	Gravitational acceleration (9.81 m/s ²)
G(t)	Growth rate
g(V')	Breakage frequency (s ⁻¹)
I	Bulk fluid ionic strength
\bar{I}	Unit tensor
Kg	Kinetic parameter
KSp	Struvite solubility constant
K _{ij}	Interphase momentum exchange coefficient
k	Turbulent kinetic energy (m ² /s ²)
M	Torque (Nm)
N	Kinetic parameter
Np	Impeller power number
\vec{N}	Angular velocity (rad/s)
n(V, t)	Number density of particle of size V at time t
P	Pressure
P	Impeller power (w)
R _i	Production rate of ith species
\vec{r}	Position vector
\vec{R}_i	Interphase momentum exchange

S_i	Source rate
\vec{U}	Velocity vector
\vec{v}_i	Phase velocity
V	Volume
Y_i	Mass fraction of each species
Z_i	Valency of corresponding elements

Greek Letter

α	Phase volume fraction
$\beta (V V')$	probability density function
γ_i	activity of solution
σ_k	Constant
σ_ε	Constant
ε	rate of turbulent energy dissipation (m^2/s^3)
θ	Azimuthal angle (degree)
μ	viscosity (kg/m.s)
$\bar{\tau}_{eff_i}$	Reynolds stress tensor (N/m^2)
v	Number of daughter particles
ρ	Phase density
τ_j	Particulate relaxation time

Subscripts

agr	Aggregation
brk	Breakage

<i>l</i>	Liquid phase
<i>lam</i>	Laminar
<i>m</i>	Mixture
<i>s</i>	Solid phase
<i>t</i>	Turbulent

1. INTRODUCTION

In this chapter the background and motivation for research into struvite precipitation are presented.

1.1 Motivation

Discharge of significant amounts of phosphate from nutrient-rich wastewater is problematic considering the potential for contamination of groundwater and eutrophication of recipient water bodies. On the other hand, phosphorus is a limited, non-renewable resource with total reserves that may be depleted in the near future. As a result, phosphorus recovery is receiving increased amounts of attention as an environmental concern. The recovery of phosphorus using a precipitation technique is one proven solution for this issue. On the other hand, computer modeling of such a process provides a useful tool to understand complex aspects of this process before designing any pilot or industrial scale crystallizer. In this work, the precipitation of Magnesium Ammonium Phosphate (Struvite) as an alternative method for the recovery of phosphorous is modeled in a batch stirred tank reactor.

1.2 Phosphorous recovery

With an expected 40% rise in the world's population by 2050 (UN, 2014), food consumption will increase rapidly in the near future, with consumption rates growing by 3.1% annually [1]. Without a doubt, naturally occurring phosphorous—found in the soil—cannot support this rapid growth in food demands. Consequently, augmenting soils with phosphorous-based fertilizers plays an indispensable role in permitting more food growth. Commercial fertilizers are produced primarily from rock phosphorous reserves. However, it has been predicted that the global supply of phosphorous will be exhausted in less than 70 years [2]. Among all of the different industries using phosphorous, agro-ecosystems consume the greatest proportion, with 41.8 Mt of P used annually as fertilizers [1].

Due to runoff and inefficient biological processes, significant levels of phosphate are released in wastewater, offering a potential source of high volumes of phosphate. Recovering phosphate from wastewater not only provides a source of phosphate, but facilitates more efficient treatment

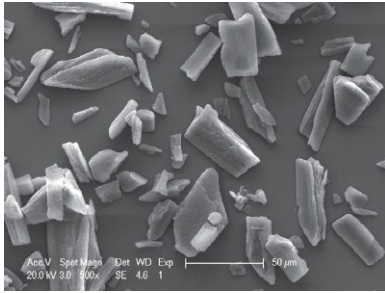
of wastewater in downstream process by removing, therefore limiting the phosphate content able to enter later stages of water treatment.

In recent years, struvite precipitation has gained attention as a method for phosphorus recovery. Known to provide a cheaper source of both P and N from wastewater, struvite makes an interesting alternative in the fertilizer industry.

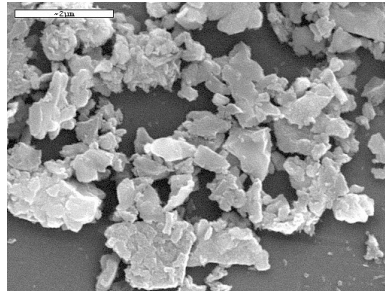
1.3 What is Struvite?

Struvite is a common industrial name for the mineral magnesium ammonium phosphate hexahydrate ($MgNH_4PO_4 \cdot 6H_2O$) or MAP which can be formed by equimolar amounts of magnesium, ammonium, and phosphate with six molecules of water for hydration. Struvite crystals exist in white (pure struvite) to yellowish or brownish-white pyramidal form. Struvite crystals may appear as the aggregate of fine crystal, star-like particles, irregular, or unshaped coarse crystals. Table 1 shows Scanning Electron Microscope (SEM) images of different crystal shapes taken by different researchers.

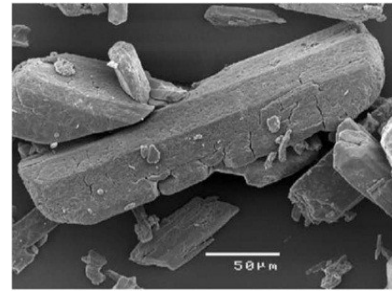
Table 1 SEM of different struvite crystal shapes



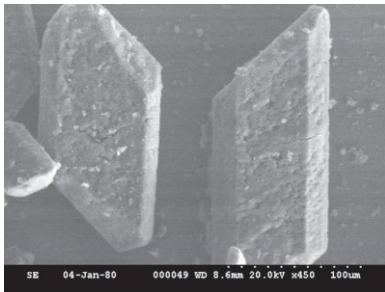
Prismatic shape crystals [3]



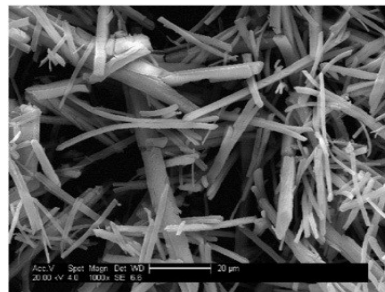
Shapeless crystals [4]



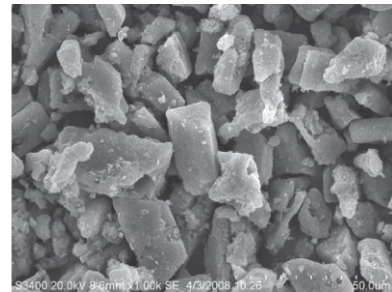
Irregular shape crystals [5]



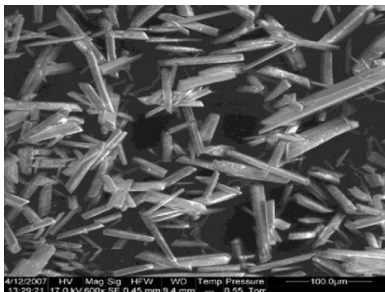
Cube like crystals [6]



Rod like crystals [7]



Cube like irregular coarse crystals [8]



Needle like crystals [9]

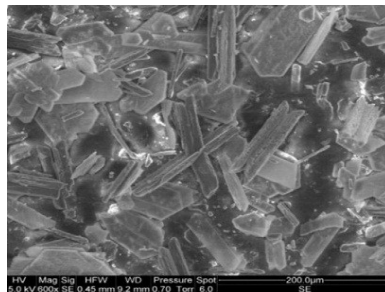
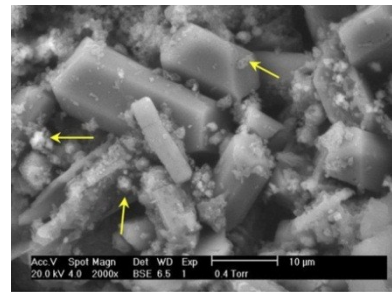


Plate like crystals [9]



Coffin like crystals [10]

Struvite crystal size can vary from 1 μm to 3 mm. Struvite is a soft mineral with 1.5-1.7 softness value on the Mohs scale [11], low density of 1730 kg/m³ [12] and molecular weight of 245.5 g/mol. Struvite is easily soluble in acid yet hardly soluble in neutral and alkaline conditions. Formation of this crystal is the primary source of kidney stones in animals and humans, which are readily precipitated in the urine.

1.4 Struvite as a Fertilizer

The agricultural benefits of struvite have been discussed by the researchers. According to its compositional structure, struvite acts as a slow release P fertilizer as it contains 13% phosphorus and composed of 6% nitrogen it could be considered a source of nitrogen and has been found to be as efficient as monocalcium phosphate (MCP). It can also increase the pH of the soil and

serves as an appropriate fertilizer for acidic soils. [13]. Since struvite has a low in-water solubility (0.018 gr per 100 ml water at 25°C), it can be considered a slow release fertilizer which making it suitable for growing without the danger of burning the roots of the plant.[14]. As struvite is a soft mineral, it can resist against rainfall washout effect which makes it suitable for flooded areas [15]. Since the demand for struvite has increased in recent years, commercial struvite recovery units are in operation in different full scale plants around the world such as: Pearl[®] Technology (North America, UK), Phospaq[™] (The Netherlands), Phosnix (Japan), Seaborne (Germany), AirPrex[™] (Germany, Netherlands) and Multiform (USA) [2]. Since use as a commercial fertilizer is the most common use of struvite, it is essential to produce it in a size-controlled manner to provide distinct grades for specific applications.

1.5 Methods for struvite recovery

There are four major methods for struvite recovery: Electrochemical, ion exchange, biomineralisation, and chemical precipitation. Although the basic principals of these methods are similar, there are differences in energy consumption and costs between these methods.

1.5.1 Electrochemical method

In the electrochemical method, Mg^{2+} , NH_4^+ and PO_4^{3-} ions forms an analyte solution and struvite deposition takes place on the cathode. The electrochemical cell contains an anode formed of inert material such as graphite, platinum, or other metals covered with carbon, and a cathode of nickel or steel plates. In this method, reduction of water or oxygen takes place at the cathode, releasing the hydroxide ion that will cause an increase in pH in the vicinity of the cathode and will help rapid precipitation of struvite. The advantage of this method is no need to add chemicals for pH adjustment, while a disadvantage of this method is the energy required for the reduction of water. This method has been studied by [16-19].

1.5.2 Ion exchange method

In the ion exchange method, the aforementioned ions are selectively exchanged in an ion exchanger and through adjustment of Mg and pH, struvite precipitation occurs. In this method, NH_4^+ is commonly exchanged for Na^+ ions in a zeolite based exchanger and PO_4^{3-} ions are

exchanged for Cl^- ions in a carboxylic-based exchanger. Co-precipitation of impurities and low-availability of anion exchangers for PO_4^{3-} ions are limitations of this method, while quick precipitation of struvite is an advantage of this method. For further information about this method, refer to [20-25].

1.5.3 Biomineralisation method

In the biomineralisation method, the minerals are deposited by microorganisms in a natural process. In the microbial production of struvite, certain bacterial strains, such as *Staphylococcus aureus* or *Myxococcus xanthus*, can precipitate struvite in a medium containing Mg and PO_4^{3-} . Microbial metabolism of the nitrogenous compound releases, NH_4^+ which is required for this process, and at the same time increases the pH which is helpful for better precipitation of struvite. This method has been studied by [26-29].

1.5.4 Chemical precipitation method

In the chemical precipitation method, struvite is precipitated from the wastewater by adding the adequate amounts of Mg in the reactor in order to reach the 1:1:1 ratio and by adjusting pH to create alkaline conditions suited for struvite precipitation. For relatively small scale plants, stirred tank reactors are used as they are easy to run and control ([30-33] [8, 34-38]) and for larger scale plants, fluidized bed reactors are used as they can provide higher reactive surface area and better solution turbulence ([39-43]). The chemical precipitation method is the most widely used due to its operational simplicity while the other mentioned techniques have some limitations, for example, electrochemical precipitation needs energy to apply required potential, and in the ion exchange method finding a suitable anion exchanger, especially for PO_4^{3-} , is the main restraint of the method [2].

Several laboratory and pilot-scale studies have been carried out to investigate the potential of such a method in the recovery of phosphorous and production of struvite as a reusable product. The technologies for struvite precipitation can be classified in one of two main categories, based on reactor design:

1. Precipitation in fluidized bed reactors (FBRs) or air-agitated reactors
2. Precipitation in a stirred reactor

FBR is the most common technology used for struvite precipitation. In FBR, which operates on fluidized flow principles, crystals grow while they are suspended in an upward flowing supersaturation solution. The absence of a stirrer limits breakage and primary nucleation in this technique, and suspended crystals are allowed to grow until a favorable size is achieved.

In stirred tank reactors struvite is crystallized by adjusting the suitable molar ratio Mg:P:N through addition of chemicals, usually MgCl_2 . An impeller is used to mix the solution while the pH is adjusted, by addition of NaOH, to reach the appropriate alkalinity. However, stirred reactors are not the best type of reactor for precipitation as compared to other types of reactors, yet they are simple for laboratory scale operation and require less complicated apparatus. In this study a batch stirred reactor is used for a number of reasons, such as: simplicity in setting up the experimental apparatus, shorter time required for each round of experimentation and less reactant requirements.

1.6 Research Objectives

Reviewing struvite precipitation literature shows lack of a holistic model that includes all of the above-mentioned aspects, hydrodynamic, thermodynamic and kinetic, in one model. For systems, such as crystallizers, in which steady-state performance, dynamic behavior, and control and optimization depends on mixing and flow behavior, developing such a comprehensive model will provide a powerful tool which could lead to significant industrial benefits. This study presents a CFD model that integrates the kinetic rates resulting from the population balance equation with flow hydrodynamic equations. Since crystal size is a cornerstone in controlling the quality of produced struvite, it should be well predicted in the suggested model. The main contribution of this work is to coupling CFD with a population balance model (PBM) to develop a 3-D CFD model which could predict crystal size distribution (CSD) in a struvite precipitation system.

2 LITERATURE REVIEW

Struvite precipitation phenomena depends on a variety of complex aspects such as fluid hydrodynamics, solution thermodynamics, mass transfer, and precipitation kinetics including the nucleation, growth, aggregation, and attrition of crystals [41, 44-46]. Design and operation of an industrial scale crystallizer requires a reliable knowledge of these aspects, which have mostly been obtained from lab scale experiments. By scaling up the lab scale results and apply them at an industrial scale, an effective model that can predict different aspects of the process and optimize reactor outputs has to be advised. In order to achieve this goal, it is important to develop a model that combines these mechanisms all in one unit, which to the authors' knowledge, has not been presented by the researchers yet.

Struvite precipitation modeling falls into three major categories: hydrodynamic-oriented models, thermodynamic-oriented models, and kinetic-oriented models.

2.1 Hydrodynamic-oriented models

Hydrodynamics-oriented models involve the design of a struvite crystallizer and attempting to predict and optimize different parameters affecting hydrodynamics such as type and speed of agitation, and reactor configuration.

General configuration of the crystallizers depends on the scale chosen for study: laboratory scale (stirred batch reactor), pilot scale (agitated batch or fluidized bed continuous reactor), and full scale (fluidized bed continuous reactor). The main challenges in designing crystallizers are determining the crystal size distribution (CSD), and predicting the effect of the impeller type and speed, reactor size and geometry, operating condition, and influence of scale on the process. Modeling the crystallizer configuration by considering the flow hydrodynamics has been widely studied by the researchers.

Kramer et al. [47] studied evaporative forced circulation crystallizer using a compartment approach. They showed that a large supersaturation profile is present in the crystallizer, which

has effect on the dynamic CSD behavior of the crystallizer. They also showed that only a part of the crystallizer volume is effectively used for crystal growth. Rousseaux et al. [48] simulated a sliding-surface mixing device with the CFD method and showed the effect of feed location, reactor geometry, rotation speed, and reagent concentration on the CSD. They found the best agreement between experiments and CFD model using a growth rate dependent on particle size and presented their model as a tool to estimate the mean particle size at the outlet of the crystallizer.

Wang et al. [49] simulated the precipitation process in a continuous stirred tank crystallizer using CFD equations, in combination with the moment equations for crystal population balance, to study the effect of feed location and concentration, impeller speed, and residence time. They showed that higher impeller speed, lower feed concentration, stronger turbulence at the feed location and longer residence times will favor larger sized crystals. Logashenko et al. [50] studied a continuous stirred crystallizer and showed the results of velocity, concentration, temperature, and crystal sizes at different time intervals coupled with the population dynamics of the crystals with the flow in the tank. Sha et al. [51] investigated a size-dependent classification function calculated based on the local particle size distribution and the factors affecting this function by CFD simulation of a mixing crystallizer. They showed that the mixing intensity, product removal location, and the particle size are the most important factors affecting this classification. Also, it is indicated that different reactor geometries have different classification profile.

Zhu and Wei [52] studied the effect of different types of impellers and different tank dimensions used in the crystallization of ammonium sulphate to observe the changes in the flow field in order to obtain an optimal crystallizer. They found that the velocity distribution did not significantly change when the particle phase was involved. They also demonstrated that a draft tube baffled crystallizer with an axial impeller could provide a suitable flow field for vacuum evaporation crystallization, a reference required to build an industrial crystallizer. Wantha and Flood [53] studied the influence of hydrodynamics in the crystallizer, as characterized by the momentum source strength and fines removal flow on the flow characteristics and the classification of crystals. They showed that increasing the axial momentum source can strongly

increase the overall magnitude of liquid velocity within the crystallizer while the fines removal flow rate has a very slight effect on the overall magnitude of liquid velocity within the crystallizer. For the vapor phase, the overall magnitude of the velocity can be slightly increased by the axial momentum source and only slightly influenced by the fines removal flow rate. Plewik et al. [54] modeled multiphase flow of mono-dispersed suspensions in different types of crystallizers (DTM, DDT and FL) using CFD methods. They concluded that the multiphase computation method is a very useful tool for such analysis. Further, they found that hydraulic conditions in industrial crystallizers are far from ideal.

Rahaman and Mavinic [55] investigated the hydrodynamic behavior of the fluidized bed crystallizer to determine segregation state of different sizes of struvite crystals. They observed the effect of flow velocity on relative distribution of different crystal sizes within the reactor. They also investigated the time-averaged distribution of solid volume fraction on radial positions and obtained a similar trend with experimental results. Al-Rashed et al. [56] simulated a Oslo fluidized bed crystallizer with the CFD technique to investigate scaling up of fluidized bed crystallizers. They showed that scaling up a fluidized bed crystallizer is a very complex task. Their simulation results confirmed that assuming flow as a plug flow in a fluidized bed may not be reliable in this kind of modeling. They also reported that the CSD strongly depends not only on vertical coordinates but also on horizontal ones. In addition, their model showed that scaling up directly from laboratory to industrial conditions is risky due to the dramatic changes in suspension bed behavior, especially at the beginning of the scaling up process. More information about CFD simulation of crystallizers can be found in Rane et al. [57].

2.2 Thermodynamic-oriented models

Thermodynamic-oriented models study and predict the conditions under which struvite will form. These models are used to design the phosphorous recovery reactors and/or to suggest methods for reducing precipitation in wastewater treatment pipelines and other industrial equipment. Since study of struvite precipitation without considering the thermodynamic aspect is nothing more than mixing chemicals without having any understanding of what is really happening, most efforts in the field of struvite precipitation contain thermodynamic studies. Different researchers have studied the thermodynamic aspect of this process using various

thermodynamic solvers. Ohlinger et al. [58] developed an improved method for predicting struvite precipitation potential in anaerobic digestion and post-digestion processes. Their study improved earlier struvite precipitation thermodynamic methods by consideration of ionic strength effects on ion activities, magnesium phosphate complexation effects on ion speciation, and experimentally derived struvite solubility constant using MINEQL+ thermodynamic solver. They reported a struvite solubility constant, K_{SO} , equal to $10^{-13.26}$ which confirmed that struvite is less soluble than previously reported. Bouropoulos and Koutsoukos [59] investigated the spontaneous precipitation of struvite in aqueous supersaturation solutions containing stoichiometric concentrations of Mg^{2+} , NH_4^+ and PO_4^{3-} ions in a batch stirred reactor using ChemEQL code solver. They found that past a threshold relative supersaturation value of 2.0, the precipitation was mostly homogenous. They showed a second-order dependence between precipitation rate and solution supersaturation suggesting a surface diffusion controlled mechanism. Also, their work suggests that aggregation may be favored at higher magnesium concentrations.

Harada et al. [60] predicted that struvite formation from human urine with development of a new equilibrium model, which considered the formation of numbers of different kinds of precipitates including struvite, with effects of ionic strength and temperature using iterative Newton's method. Their model confirmed that precipitates formed in urine in struvite-recovery conditions were composed mainly of struvite and contained little Ca precipitate. This model also predicted the optimum pH to form struvite (pH=9.4-9.7). Çelen et al. [61] investigated the usefulness of a chemical equilibrium model, Visual Minteq, for determining the modifications needed to maximize struvite precipitation from liquid swine manure and thus reduce the orthophosphate phosphorus concentration. They showed that by only increasing pH in swine wastewater, it was possible to significantly reduce the quantity of orthophosphate. This research also indicated that the addition of extra source Mg^{2+} is required for the optimum recovery of orthophosphate. They reported that by entering the actual ion concentration, alkalinity, and pH as input data into the model, it is easy to conduct iterative analyses for the various amendments to optimize orthophosphate removal.

Rahaman et al. [62] developed a mathematical model solved by MATLAB software which predicted species concentration decrease with increasing bed height. Their model also predicted increments of bed voidage, and decreasing crystal size as crystal bed height increased. Gadekar and Pullammanappallil [63] developed a mathematical model using physicochemical equilibrium expressions, charge, and mass balance equations for the constituent ions to predict struvite precipitation to within a 1.6% to 9% error range. An iterative residual procedure was used to solve the model in Maple solver software. They found that the optimal pH for struvite concentration depends on the initial ratio of the constituent ions. They also reported that to obtain pure struvite, extra ammonia in the solution is necessary and an equimolar stoichiometric ratio of constituent ions is not ideal. Hanhoun et al. [64] proposed a thermodynamic model using the Newton-Raphson iterative algorithm, which was implemented in MATLAB environment to demonstrate the conversion rate of phosphate and as well as the value of struvite solubility product at a specific temperature range. Their model can quantitatively and qualitatively predict the precipitated struvite, the final state of the solution, phosphate conversion rate, and pH values. Lee et al. [65] developed an equilibrium model to predict phosphorus recovery and amount of struvite using an iterative procedure in MATLAB and Visual MINTEQ software. Their model predicts P recovery amounts with high accuracy ($R^2 > 95\%$) and Mg concentration in reasonable agreement with experimental data. Lee et al. [66] investigated struvite precipitation under different ionic concentration and pH levels using a computational model solved by MATLAB. Phosphorus removal, decrease in the pH level, effect of N/P ratio, and the precipitate amounts as a function of reaction time and initial ionic conditions are the parameters which their model successfully predicted. They reported that in a high nitrogen concentration condition, more P removal occurs due to pH buffering and struvite precipitation becomes sustainable in this condition. Furthermore, higher N concentration is desirable for maintaining the struvite purity, while the inclusion of Ca^{2+} in the precipitation process has the reverse effect. Recently, Barnes and Bowers [67] developed a struvite solubility model based on a probabilistic approach using a Monte Carlo method—solved by MATLAB—to understand the effect of uncertainty on potential struvite precipitation over a range of pH, temperatures, and ionic strengths. Their model confirmed that using equilibrium parameters involved in struvite precipitation such as solubility product of struvite (K_{sp}) without considering the uncertainty of this inputs, are not acceptable

enough for accurate prediction of solubility. The results of their model show that precipitation can be accurately modeled within a range of values.

2.3 Kinetic-oriented models

Kinetic-oriented models attempt to determine the rate of struvite precipitation, which is the rate at which struvite constituent ions (magnesium, ammonium and phosphate) are consumed and struvite produced. This can predict the variation of crystal size—as a final product—with the time and/or optimized residence time and reactor volume. One of the main approaches for studying the kinetic rate of struvite precipitation is selecting a limiting reactant—which controls the precipitation rate—and defining kinetic equations based on its concentration, as in the case of struvite, phosphate typically is chosen. Based on the aforementioned approach, researchers suggested first order kinetics and second order kinetics for struvite precipitation [33, 59, 68-75]. One drawback of this approach is that the nucleation and growth effect can not be differentiated from the kinetic model and has an unknown combination of the growth and nucleation.

Another effective approach for studying precipitation kinetics is based on assuming that growth rate is the dominant phenomena and the effect of other phenomena such as nucleation, breakage, and aggregation are minimal. This assumption is valid when the crystallization is occurred within the metastable zone (discussed in 3.1.2). In this approach it is assumed that any mass transfer between phases or any changes in crystal sizes occurs only due to the growth of seed population [44, 76, 77].

In other studies, researchers investigated the precipitation kinetics based on assuming growth rate or in a few cases, nucleation and/or aggregation rate as a function of supersaturation state of the solution and reported order-dependency of the equation [46, 78-81]. (Discussed in 3.3.3).

Few researchers have presented a holistic model that covers more than one aspect of the process. Since this work focuses more on crystal size prediction, papers that predict crystal size distribution have been reviewed.

Ali and Schneider [44] estimated the crystal growth rate considering the thermodynamic aspect and power relation between growth rate, supersaturation index, and supersaturation ratio. By using their estimated coefficients, they predicted average particle size with 10% error, which is an acceptable level of prediction. Their work has limitations including ignoring the

hydrodynamic behavior of the system and a lack of size distribution prediction. Hanhoun et al. [46] proposed kinetic rates for growth and nucleation using a population balance-based model coupled with a thermodynamic model. They predicted crystal size distribution using a reconstruction model. Their results under-predicted the CSD with a significant percentage of error. Ignoring flow effects on the process, overlooking aggregation and breakage, and a high degree of numerical deviation are the main limitations of this study. Rahaman et al. [41] presented a comprehensive mathematical model for a fluidized bed crystallizer including aspects of thermodynamics, precipitation kinetics, and reactor hydrodynamic in one model. Their results predicted removal efficiencies of constituent ions in an acceptable level of agreement with the experimental data. They also predicted average crystal size within a 20-30% error range. Lack of size distribution prediction is a major drawback for their work. Galbraith et al. [80] estimated the coefficient values for nucleation, growth, and aggregation rate using a data set generated from 14 batch experiments. This model covers solution thermodynamics and particle development tracking by applying a population balance model. They predicted the time varying CSD by employing estimated kinetics rates. Prediction of the size distribution within a 20-30 % error range, as well as predicting the most common size at every time interval are important achievements of their work. Ignoring the complexity of hydrodynamic effects is the main limitation of their study.

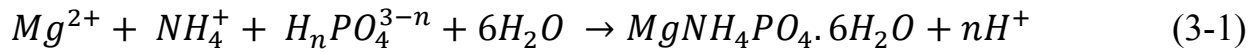
3 MATERIALS AND METHODS

3.1 Experimental Works

This section outlines the experimental method used for data collection for struvite precipitation. In these experiments, parameters for struvite crystal growth were measured to validate the CFD results. Finally, the seed preparation method is described.

3.1.1 Introduction

Magnesium Ammonium Phosphate (MAP) hexahydrate ($MgNH_4PO_4 \cdot 6H_2O$), commonly known as struvite, is a white crystalline substance containing equimolar amounts of magnesium, ammonium, and phosphate with six hydrating water molecules per formula unit. The simplified chemical reaction detailing the formation of struvite is as follows:



Meanwhile, any precipitation phenomena, which could be defined as the production of any solid phase form in an aqueous solution, are governed by solution thermodynamics. Hence, characterization of solution thermodynamics seems a separable piece of such a study. This section focuses on the key thermodynamic and chemical aspects of this problem.

3.1.2 Solubility Curve and Metastable Zone

Supersaturation of a solution is key to any precipitation. Supersaturation describes a solution where the solute concentration is greater than the equilibrium concentration and as such is a necessity for precipitation. This parameter depends on solution pH and concentration of reactive species. As multiple ions are involved in supersaturation in this case, defining solute concentration can be complex. To overcome this issue and to have a parameter to describe the state of supersaturation, solute concentration is defined in terms of the ion activity product (IAP), as detailed in the following equation:

$$IAP = \{Mg^{2+}\}\{NH_4^+\}\{PO_4^{3-}\} \quad (3-2)$$

$\{C_i\}$ represents the ion activity of ion C_i .

By defining IAP, the degree of supersaturation as defined with the supersaturation index (SI) is as follows:

$$SI = \log\left(\frac{IAP}{K_{sp}}\right) \quad (3-3)$$

where K_{sp} is the solubility product which shows the equilibrium state.

Therefore, when the IAP is less than K_{sp} , the solution is unsaturated and when IAP is more than K_{sp} , the system is supersaturated and nucleation or/and growth can occur and over time the system will ultimately return to equilibrium state. The equilibrium solubility product used in this work is $K_{sp} = 13.26$ [58] fixed at 25° C and standard atmospheric pressure.

The estimation of IAP for struvite has been made from the total initial molar concentrations of magnesium, ammonia, phosphate, and measured equilibrium pH. For this calculation, these twelve species must be considered [41]: $MgPO_4^-$, $MgHPO_4$, $MgH_2PO_4^+$, Mg^{2+} , $MgOH^+$, $H_2PO_4^-$, HPO_4^{2-} , PO_4^{3-} , NH_4^+ , H^+ , OH^- , and $NH_3(aq)$. The corresponding equilibrium equations as well as the values of thermodynamic constant for these ions and complexes are provided in Table 2:

Table 2 Equilibrium Constant for complexes

Equilibrium	pk (25° C)	Reference
$[Mg^{2+}][PO_4^{3-}]/[MgPO_4^-]$	4.92	[82]
$[Mg^{2+}][H_2PO_4^-]/[MgH_2PO_4^+]$	0.45	[83]
$[Mg^{2+}][HPO_4^{3-}]/[MgHPO_4]$	2.9	[84]
$[Mg^{2+}][OH^-]/[MgOH^+]$	2.56	[83]
$[H^+][H_2PO_4^-]/[H_3PO_4]$	2.15	[85]
$[H^+][HPO_4^{2-}]/[H_2PO_4^-]$	7.198	[85]
$[H^+][PO_4^{3-}]/[HPO_4^{2-}]$	12.375	[85]
$[NH_3][H^+]/[NH_4^+]$	9.3	[86]
$[H^+][OH^-]/[H_2O]$	13.997	[85]

Since analytical determination of magnesium, ammonia, and phosphate provide the total concentration of these species in solution, it is necessary to calculate ion activity by utilizing the appropriate activity coefficient and dissociation constants. The activity coefficient can be determined using a variety of empirical equations. Here, the Davies equation has been used to

calculate the activity coefficient, since it is capable of performing activity calculations for higher ionic strengths[87]:

$$-\log \gamma_i = AZ_i^2 \left[\frac{I^{1/2}}{1+I^{1/2}} \right] - 0.3I \quad (3-4)$$

where γ_i is the activity of solution, Z_i is the valency of corresponding elements, and A is the Debye-Huckel constant, which has a value of 0.509 at 25°C [87].

I is the bulk fluid ionic strength which can be calculated by the following defined relation, based on each species of ionic concentration, C_i (Mg^{2+} , NH_4^+ and PO_4^{3-}) and its respective charge, Z_i :

$$I = \frac{1}{2} \sum C_i Z_i^2 \quad (3-5)$$

Solving the above equations must be done with a numerical approach due to their complexity and non-linear nature. Different researchers used different tools for solving thermodynamic equations, as discussed in section 2.2. A number of specialized water chemistry computational solvers such as PHREEQC, MINTEQA2, MINEQL+, and VisualMINTEQ can be used to solve the above equations together. Also, in-house code using MATLAB or other programming languages has been used in some other studies.

In this work, a commercial spreadsheet software was used to solve all of the equilibrium equations and constants in table 2 along with the equations (3-2) to (3-5), based on iterative calculations for a given pH or SI.

Solubility and saturation are the parameters describing the potential for crystal formation in a solution. Considering struvite as a salt, the solubility at a given temperature depends on two major factors: species concentration and solution pH. Based on the aforementioned factors, three zones of precipitation are possible:

1) Unsaturated zone: crystals dissolve when added to the solution, and therefore, precipitation is impossible.

2) Metastable zone: the solution is saturated and crystal growth can occur by seed addition, but the amount of Gibbs free energy is not enough for spontaneous nucleation. Therefore, the growth phenomenon is predominant in this zone.

3) Labile zone or unstable zone: the solute concentration exceeds the equilibrium value considerably and spontaneous nucleation can occur. Crystal growth can be rapid in this region.

For identification of the metastable zone, the minimum and maximum pH range needs to be defined. The minimum pH (lower-limit) of the zone shows the pH for minimum struvite solubility and it is predicted by solving all the thermodynamic equations described earlier. The maximum pH range (upper-limit) shows the threshold for the beginning of spontaneous nucleation, as derived from a series of experiments conducted by Ali and Schneider [5]. In these series of experiments, a synthetic solution of Mg^{2+} , NH_4^+ , and PO_4^{3-} was made at low pH. Then the pH was increased to the saturation limit by adding NaOH. Then the solution was monitored by a laser light scattering device in a dark room to detect the first appearance of crystal cloud in the solution. The experiment was conducted at different initial concentrations of ions at a ratio of 1:1:1. The result of Ali and Schneider [5] experiments together with thermodynamic predictions are presented in figure 1 illustrating the three above named zones for struvite:

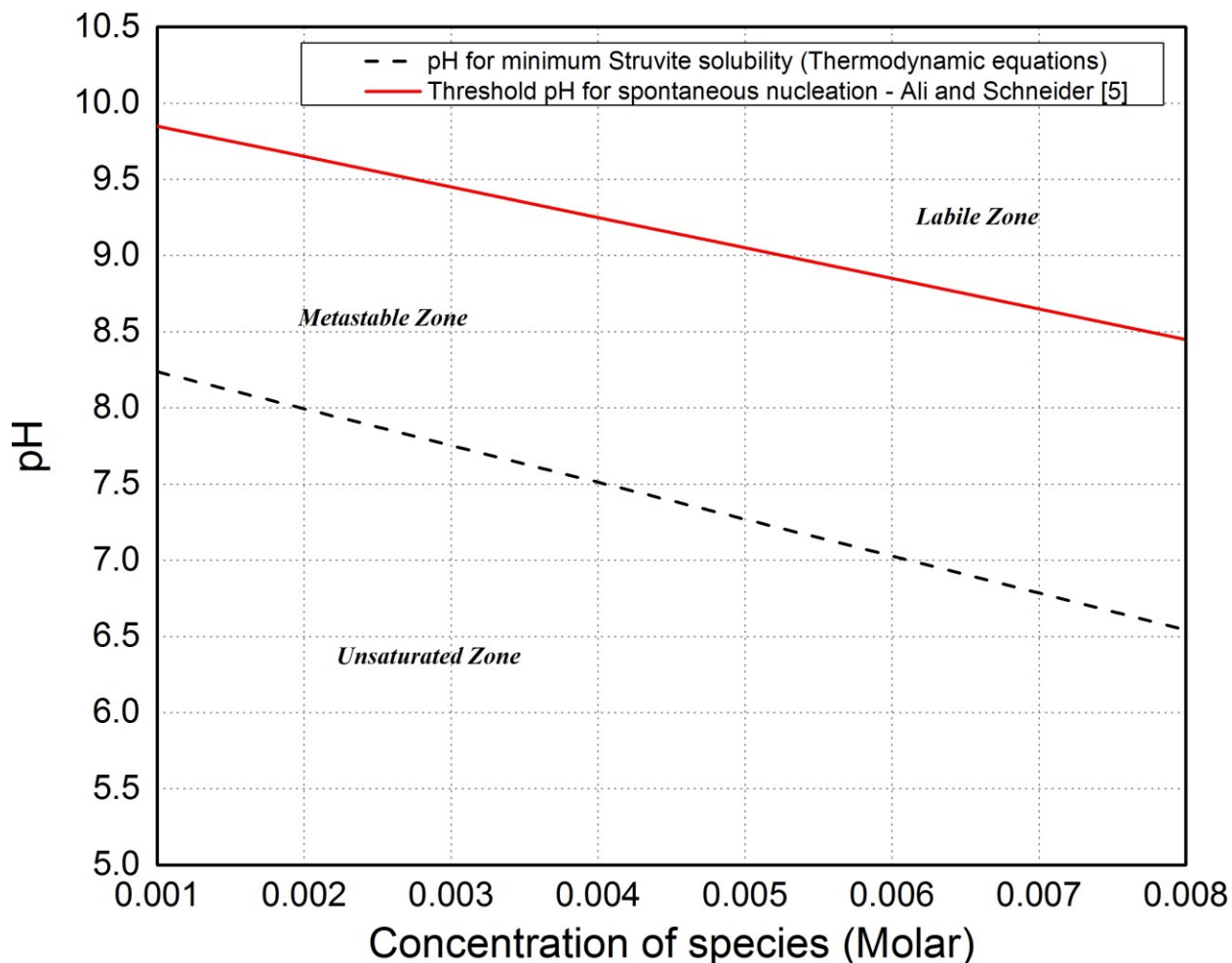


Figure 1 Determination of different saturation state zones for Struvite

The middle zone, zone between the red line and dashed line, in figure 1, shows the operating zone for precipitation. The pH range between the minimum and maximum limit shows the metastable zone where the precipitation within this range will be heterogeneous.

In this study, the initial molar concentration of species and pH were chosen in such a way that the initial state of solution stayed in the metastable zone. Precipitation occurring in this zone mean that crystal growth is the dominant mechanism of precipitation [76]. Also choosing the lowest possible pH in this zone will hinder crystal aggregation, as it has been reported that with increasing supersaturation, crystals are more adhesive and, accordingly, there is a higher chance of crystal aggregation [88]. This approach assumes that mass transfer between liquid phase and solid phase, which appears as change in crystal size, occurs due to the growth of initial seeds and other phenomena, such as nucleation, aggregation, and breakage, have minimal effect.

3.1.3 Experimental setup

The eventual goal of this experiment is to provide accurate and repeatable results to investigate the accuracy of PBM-coupled CFD model. The experimental works aim to determine the crystal size distribution at different time intervals. Batch experiments were performed, as it is easier in regards to parameter control.

The batch experiments were carried out in a 1-L glass reactor with a round bottom and baffled with four removable, equidistant stainless steel baffles. Using baffles improve the fluid mixing to avoid the creation of a dead zone occurring in the reactor and also help quick dynamic pH response. The reactor was well mixed with a Rushton impeller at a constant speed of 100 rpm in all experiments. A photograph and corresponding schematic diagram of the experimental apparatus are provided in Figure 2 A and B, respectively.

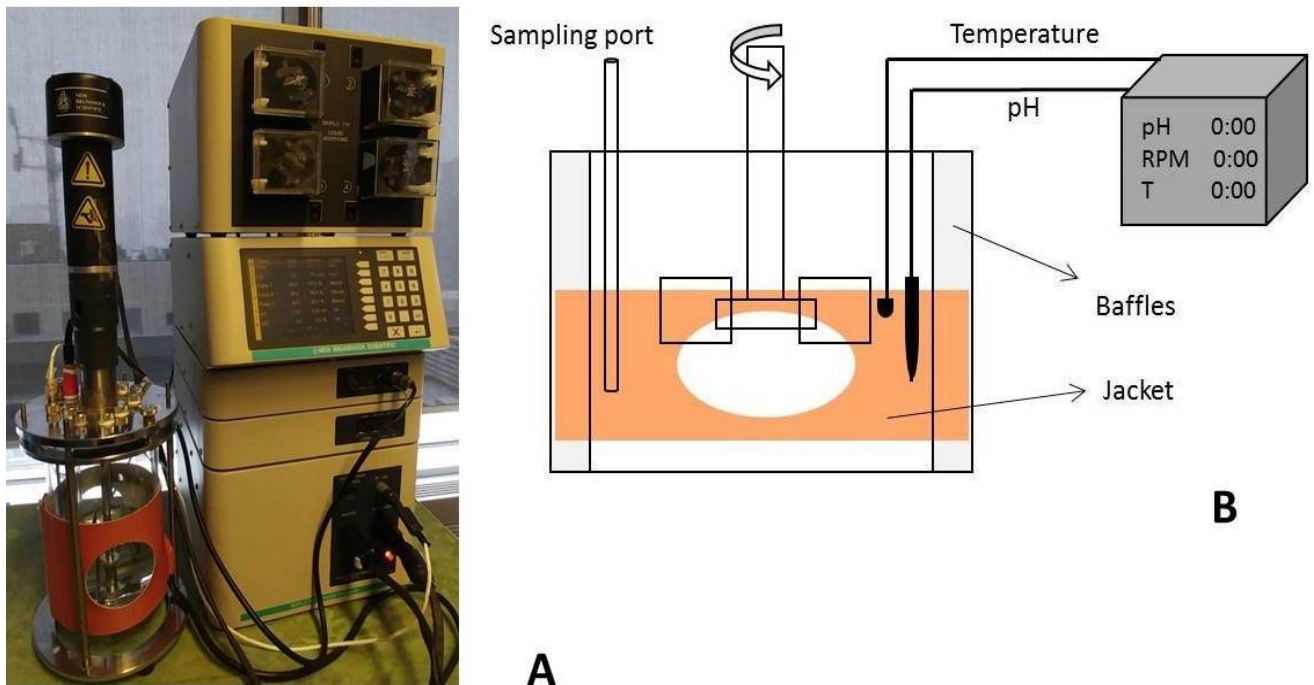


Figure 2 Photographic (A) and Schematic (B) view of crystallizer

3.1.4 Materials

In this study, synthetic solution containing the constituent ions of struvite was used. The reagents used in preparation of the synthetic solution were Sigma ACS reagent grade $\text{NH}_4\text{H}_2\text{PO}_4$ and $\text{MgCl}_2 \cdot 6\text{H}_2\text{O}$, and Mili-Q distilled water. Also 0.5 M NaOH solution used to adjust the pH. The temperature was held at 25°C in all experiments. The PH probe was calibrated with pH 7 ± 0.01 and 4 ± 0.01 buffer solutions before every experiment. As discussed before, SI is highly pH dependent as found in previous studies. When pH increases, the concentration of phosphate ion increases while the concentration of Mg and NH_4^+ decreases, and consequently ion activity product increases. Therefore, the supersaturation index can be increased by increasing the pH of solution, or by increasing the concentration of struvite constituent ions. In this work, the initial value of the supersaturation index was adjusted by changing the pH of the solution.

3.1.5 Seed Preparation

As the initial solution is in the metastable zone, it is expected that growth governs the precipitation process. Therefore, the experiments were seeded to limit primary nucleation. To uniformly disperse seeds, wet seeding was chosen. To prepare the seed, first 0.005 mol of $\text{NH}_4\text{H}_2\text{PO}_4$ and $\text{MgCl}_2 \cdot 6\text{H}_2\text{O}$ were dissolved in 1L DI water and the whole system was stirred with a magnetic stirrer. Then, the pH was brought up by adding 0.5M NaOH until the first crystals precipitated. To avoid producing big crystals, adding of NaOH was stopped at this point. Then the solution was filtered and the crystals were dried overnight. In order to measure the distribution of seed crystal size, which shows the initial particle size distribution, 4 random samples were collected from the dried seed stock and then dispersed in 4 tubes containing DI water with a pH of 8. With the objective of ascertaining the lack of aggregation between seed particles, they were sonicated for 5 min. CSD measurement was performed for all four of the random samples. Figure 3 shows the results and the average chosen as the initial size distribution for seed.

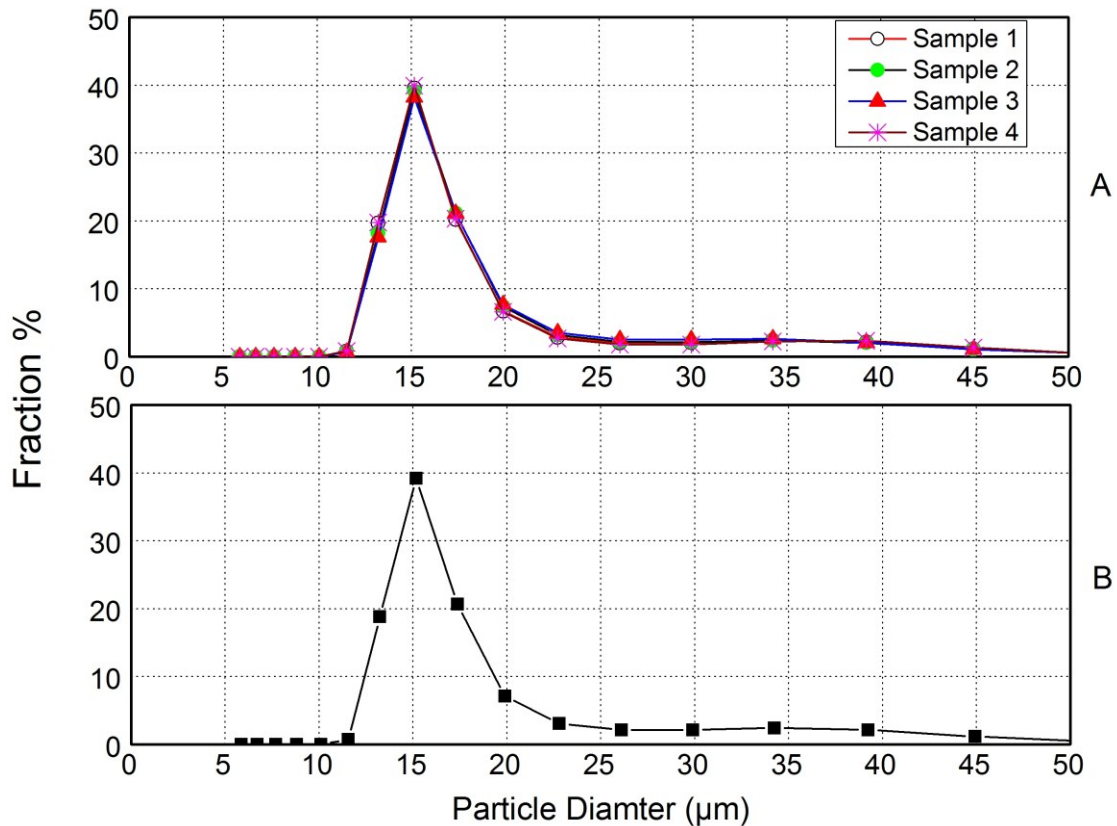


Figure 3 Number-based Crystal Size Distribution of seeds, (A) random samples and (B) average used in the CFD model

As can be seen from figure 3A, the CSD results for all four samples are similar and thus the taken average CSD is representative of the seed stock. Figure 3B, shows the average value of the seed CSD.

3.1.6 Measurements

Two key measurements in this study are crystal size distribution (CSD) and pH. This is because CSD is the ultimate goal of this work and pH is an easily applicable parameter to measure and control the experiment in real life.

3.1.6.1 Crystal Size Distribution Measurement

Measuring crystal size distribution with high accuracy is critical as distribution is predicted by the CFD model. Laser diffraction (LD) is the most common technique of experimentally determining the particle size distribution. This technique measures the size distribution indirectly by measuring the total particle volume in each size interval by fitting a volume-based distribution

to a back-scattering pattern. This technique assumes that all particles are spherical. This LD method is widely used for measuring CSD of struvite. [5, 45, 89-92]. As mentioned earlier, one obstacle in using this method is that this technique measures the volume-based size distribution. Converting the volume-based distribution to length-based or number-based distribution will cause numerical inaccuracy.

In this work, the crystal size distribution measurements were performed by a laser scattering particle size distribution analyzer from HORIBA (Model partica LA-950V2), figure 4. The detection range of the machine ranges from 10 nm to 3 mm, which covers the expected particle size range.



Figure 4 Photographic view of particle size analyzer

3.1.6.2 pH Measurement

As discussed in previous sections, the importance of solution pH on struvite solubility in water makes the pH a significant parameter in struvite precipitation. In the precipitation process, as the magnesium, ammonium, and phosphate ions in liquid phase are converted to struvite crystals in solid phase, the speciation of the solution changes and consequently, the pH changes (decreases in this case). Therefore, pH is a parameter that shows the state of supersaturation and the dynamic pH measurement provides another measurement option for monitoring the process. In this work, pH measurement was performed by a Mettler Toledo pH probe (Model 405-DPAS-SC-K8S/225).

For assuring the accuracy and repeatability of the measurements, the pH probe was calibrated with pH 7 ± 0.01 and pH 4 ± 0.01 buffer solutions before each experiment.

3.1.7 Experimental procedure

As discussed, the initial state of the batch reactor was held at the metastable zone to limit nucleation and aggregation. To do this, different initial values of SI were selected to conduct the experiment. First, the constituent ions were prepared by dissolving 0.005 M of Mg, N, and P in 1 L DI water. Through adjusting the pH by addition of 0.5 M NaOH, different initial pH and SI values were obtained. Initial conditions for these experiments are shown in table 3.

Table 3 Initial concentration and pH of the experiments

Exp. NO	Total Concentration (mol/L)			Starting pH	Starting SI
	Mg	N	P		
1	0.005	0.005	0.005	7.76	0.696
2	0.005	0.005	0.005	7.85	0.788
3	0.005	0.005	0.005	8	0.939
4	0.005	0.005	0.005	8.3	1.230
5	0.005	0.005	0.005	8.39	1.314

Five different experiments with different initial pH were conducted to select the best initial pH for the main experiment. Once the pH reached the most desirable value, the solution was seeded.

For each experiment, the seed was prepared with the same steps as described in seed preparation section. The seed had a solid concentration of 3 g/L and was sonicated for 5 min.

In order to analyze the CSD, samples of the crystals produced during the experiment had to be taken at different time intervals. Having proper agitation in the reactor assures that each sample CSD is representative of the reactor. Sampling was performed by a pipette with a large enough inlet size and a consistent and accurate sample volume (50 ml). Each sample was analyzed by Particle Size Analysis immediately after removal from the reactor.

3.2 Numerical Simulation

3.2.1 Introduction

Computational Fluid Dynamics (CFD) is a powerful tool for the study of the hydrodynamic portions of most of the processes. Using CFD solves complex partial differential equations governing conservational laws of mass and energy. In the CFD technique, the flow domain is divided into a finite number of grids or cells and differential equations of continuity, momentum, and energy conservation are discretized and solved at any determined position within or at the center of these cells. Then, by defining the initial and boundary conditions, these equations are solved. Additionally, certain parameters can be defined and set for solution convergence, stability, and accuracy control. In this method, considering the shape of reactor, it is possible to predict the flow field as well as local concentration of species and precipitation state. CFD has been previously applied successfully to predict the behavior of different types of crystallizers [57]. Although some existing CFD models have limitations to their applicability, it is still one of the most powerful simulation techniques available.

3.2.2 Governing Equation

3.2.2.1 Two phase flow

As in the precipitation process, there are two phases to deal with and the model must solve the conservation equations of continuity and momentum for each phase. For the modeling of a two-phase flow, there are two main approaches: Euler-Euler and Euler-Lagrange. In the Euler-Euler approach, the two phases are considered mathematically as interpenetrating continua. As the two phases occupy separate volumes, the concept of volume fraction is valid and these two sets of

equations are closed by constitutive relations or by the application of kinetic theory. In the Euler-Lagrange approach, also known as discrete phase approach, the predominant phase (e.g. liquid phase) is treated as a continuous phase by solving the Navier-Stokes equations, whereas the secondary phase is handled by solving an equation for a large number of particles. The Euler-Euler approach is more popular since memory storage requirements and computer power demand depends on the number of computational cells considered instead of the number of particles. Due to this, the Euler-Euler approach was chosen for this work, as the secondary phase volume fraction is high and varies by time.

3.2.2.2 Continuity Equation

Most of the processes taking place in a stirred tank reactor are under a turbulent regime. Therefore, the Reynolds averaged mass and momentum equations must be considered. The Reynolds averaged equations are primarily used to describe turbulent flow. In these equations, the solution variables in the instantaneous (exact) Navier-Stokes equations are decomposed into the mean (time-averaged) and fluctuating components. The continuity equation for each phase is as follows:

a) For liquid phase:

$$\frac{\partial}{\partial t}(\rho_l \alpha_l) + \nabla \cdot (\rho_l \alpha_l \vec{U}_l) = 0 \quad (3-6)$$

b) For solid phase:

$$\frac{\partial}{\partial t}(\rho_s \alpha_s) + \nabla \cdot (\rho_s \alpha_s \vec{U}_s) = 0 \quad (3-7)$$

where α_l is the volume fraction of liquid phase, α_s is the volume fraction of solid phase, ρ is the density, and \vec{U} is the velocity vector.

The liquid phase l and solid phase s are assumed to share the whole space in proportion to their volume such that sum of their volume fractions is equal to one:

$$\alpha_l + \alpha_s = 1 \quad (3-8)$$

3.2.2.3 Momentum equation

The momentum conservation equation for each phase is written as:

a) For liquid phase:

$$\frac{\partial}{\partial t}(\rho_l \alpha_l \vec{U}_l) + \nabla \cdot (\rho_l \alpha_l \vec{U}_l \vec{U}_l) = \alpha_l \nabla p + \nabla \cdot \bar{\bar{\tau}}_{effl} + \vec{R}_l + \vec{F}_l + \rho_l \alpha_l \vec{g} \quad (3-9)$$

b) For solid phase:

$$\frac{\partial}{\partial t}(\rho_s \alpha_s \vec{U}_s) + \nabla \cdot (\rho_s \alpha_s \vec{U}_s \vec{U}_s) = \alpha_s \nabla p + \nabla \cdot \bar{\bar{\tau}}_{effs} + \vec{R}_s + \vec{F}_s + \rho_s \alpha_s \vec{g} \quad (3-10)$$

where p is the pressure shared by the two phases and \vec{R}_i represents the interphase momentum exchange terms. The interphase momentum transfer is due to interfacial forces acting and interactions between water and solid particles.

The term \vec{F}_i represents the centrifugal force and Coriolis acceleration force term applied rotation and is written as:

$$\vec{F}_i = -2\alpha_i \rho_i \vec{N} \times \vec{U}_i - \alpha_i \rho_i \vec{N} \times (\vec{N} \times \vec{r}) \quad (3-11)$$

The Reynolds stress tensor $\bar{\bar{\tau}}_{effi}$ is based on the mean velocity gradients using the Boussinesq hypothesis:

$$\begin{aligned} \bar{\bar{\tau}}_{effi} &= \alpha_i (\mu_{lam,i} + \mu_{t,i}) (\nabla \vec{U}_i + \nabla \vec{U}_i^T) \\ &- \frac{2}{3} \alpha_i (\rho_i k_i + (\mu_{lam,i} + \mu_{t,i}) \nabla \cdot \vec{U}_i) \vec{I} \end{aligned} \quad (3-12)$$

where $\mu_{lam,i}$ is the laminar viscosity of i th phase and $\mu_{t,i}$ is the turbulent viscosity of i th phase.

3.2.2.4 Interface momentum exchange

The two phases interact through momentum transfer term [equations (3-9) and (3-10)]. This momentum exchange occurs through interfacial forces acting on liquid and solid. These forces-considered as sources or sinks in the momentum equation-must be formulated separately. They include the following forces: drag, lift, virtual mass, wall lubrication, and turbulence dispersion. Between these forces, the most important one is drag, which acts on the solid particles, resulting from the mean relative velocity between the two phases and also an additional variable derived from turbulent fluctuations in the volume fraction due to momentum equation averaging. Other forces have not been included in this work.

In this work a simple form of interaction has been used to solve the interphase force:

$$\sum_{j=1}^n \overline{R}_{ji} = \sum_{i=1}^n K_{ji} (\overline{v}_i - \overline{v}_j) \quad (3-12)$$

Where \overline{v}_i and \overline{v}_j are the phase velocities and $K_{ji} = K_{ij}$ is the interphase momentum exchange coefficient, which can be written in the following equation:

$$K_{ji} = \frac{\alpha_i \alpha_j \rho_j f}{\tau_j} \quad (3-13)$$

where τ_j is particulate relaxation time defined as:

$$\tau_j = \frac{\rho_j d_j^2}{18\mu_i} \quad (3-14)$$

where d_j is the diameter of solid particles.

And f is the drag function, which contains the drag coefficient C_D . There are different drag models used throughout the literature and the difference between them relies on the difference between the way they are calculating this f function. Between different drag models, Syamlal-O'Brien offers more accurate results in this type of study as compared to the other methods [93].

The Syamlal-O'Brien model:

$$f = \frac{C_D Re_s \alpha_l}{24v_{r,s}^2} \quad (3-15)$$

Drag equation derived by Dalla Valla:

$$C_D = \left(0.63 + \frac{4.8}{\sqrt{Re_s/v_{r,s}}} \right)^2 \quad (3-16)$$

In this model, based on measurements of the terminal velocities of particles in settling or fluidized beds, the relative Reynolds number can be derived, which has a correlation with volume fraction:

$$Re_s = \frac{\rho_l d_s |\overline{v}_s - \overline{v}_l|}{\mu_l} \quad (3-17)$$

where l is for the liquid phase, s is for the solid phase, and d_s is the diameter of the solid phase particles.

3.2.2.5 Turbulence modeling – RNG k-ε model

In this work, the renormalized group k-ε model was used. The RNG k-ε model was derived using a statistical technique called renormalization group theory and this model is similar in form to the standard k - ε model, but following refinements make it more accurate and reliable for a wider range of flows especially mixed tank reactor flows:

- 1) The RNG model has an additional term in its equation that improves the accuracy for rapidly strained flows.
- 2) The effect of swirl on turbulence is included in the RNG model, enhancing accuracy for swirling flows.
- 3) The RNG theory provides an analytical formula for turbulent Prandtl numbers, while the standard k-ε model uses user-specified constant values.
- 4) While the standard k-ε model is a high-Reynolds number model, the RNG theory provides an analytically-derived differential formula for effective viscosity that accounts for low-Reynolds number effects. Effective use of this feature does, however, depend on an appropriate treatment of the near-wall region.

Although this model increases the time taken for the calculation stability, it is more accurate than the standard k-ε model. For the continuous phase—liquid phase in this study—the RNG k-ε model was used and the governing equations are written as below:

$$\frac{\partial}{\partial t}(\rho_m k) + \nabla \cdot (\rho_m \overline{v_m} k) = \nabla \cdot \left(\frac{\mu_{t,m}}{\sigma_k} \nabla k \right) + G_{k,m} - \rho_m \varepsilon \quad (3-18)$$

$$\frac{\partial}{\partial t}(\rho_m \varepsilon) + \nabla \cdot (\rho_m \overline{v_m} \varepsilon) = \nabla \cdot \left(\frac{\mu_{t,m}}{\sigma_\varepsilon} \nabla \varepsilon \right) + C_{1\varepsilon} G_{k,m} - C_{2\varepsilon} \rho_m \varepsilon \quad (3-19)$$

where $G_{k,m}$ is generation of turbulent kinetic energy due to the mean velocity gradients. The effective turbulent transport varies with the effective Reynolds number (or eddy scale) allowing the model to better handle low-Reynolds number and near-wall flows. In the high-Reynolds number, as used this work, turbulence viscosity of the *i*th phase calculated form

$$\mu_{t,m} = \rho_m C_\mu \frac{k^2}{\varepsilon} \quad (3-20)$$

where C_μ is constant. Other fundamental turbulent flows model constant values have been determined from previous experiments. The most widely accepted standard values for these constants are as follows:

$$C_{1\varepsilon} = 1.44, C_{2\varepsilon} = 1.92, C_\mu = 0.09, \sigma_k = 1.0, \sigma_\varepsilon = 1.3$$

3.2.2.6 Species transport equation

The conservation equation for the i th species is

$$\frac{\partial}{\partial t}(\rho Y_i) + \nabla \cdot (\rho V_k Y_i) = \nabla \cdot \left(\rho D_m + \frac{D_t}{Sc_t} \right) \nabla Y_i + R_i + S_i \quad (3-21)$$

where Y_i is the i th species mass fraction, Sc_t is turbulent Schmidt number, D_t is the turbulent diffusivity, D_m is molecular diffusion, R_i is the rate of species i production by chemical reaction, and S_i is the rate of addition by any extra sources. The default Sc_t number is 0.7 [94].

3.2.3 Model Development

The reactor geometry and model configuration, impeller rotation modeling, as well as the method of solution used in the CFD modeling are described in this section.

3.2.3.1 Reactor Geometry

The same reactor, as used in the experiment, was modeled in simulation. The reactor was built of glass and had a diameter of 124 mm and a height of 90 mm. The reactor was agitated by a standard six-blade Rushton turbine impeller. The clearance between the centrally located impeller and the bottom of reactor was held at 35 mm. Further geometrical details are given in Figure 5.

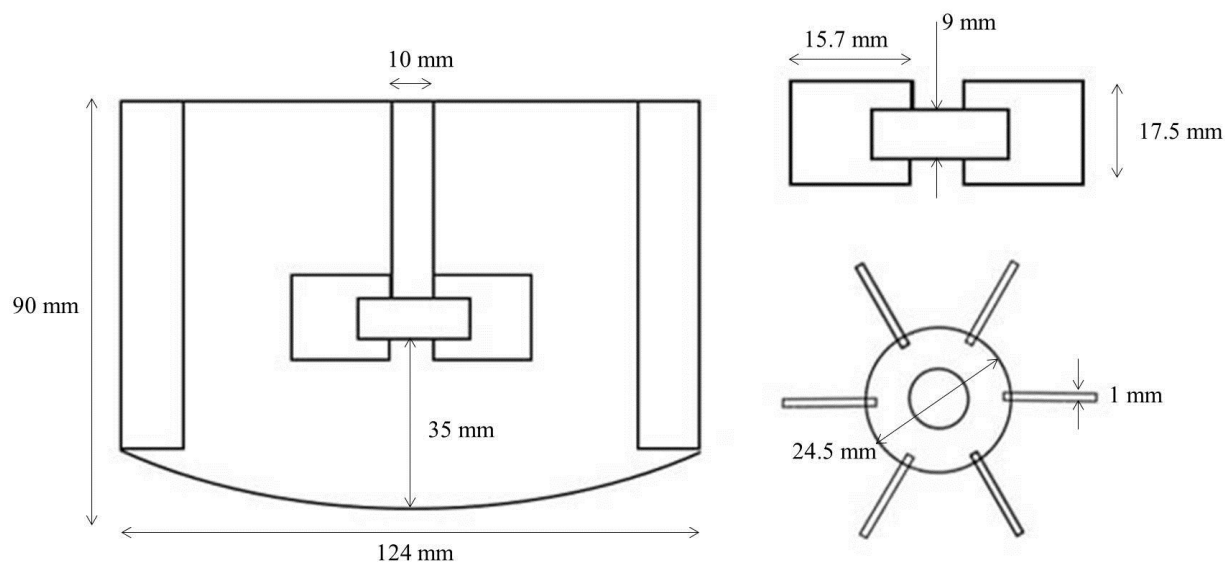


Figure 5 Schematic view of the reactor geometry and impeller used for this study

To baffle the flow, there are four removable stainless steel baffles positioned at equal distances from each other in the reactor. The reactor was mixed at a constant rate of 100 RPM. The combination of baffles and the impeller improves both the mixing uniformity as well as the quick and dynamic pH response.

3.2.3.2 Impeller rotation modeling

Modeling the impeller rotation is complex as there is relative motion between the stationary baffles and rotating impeller blades. The two most common approaches for this type of modeling are the Multiple Reference Frame (MRF) and Sliding Mesh (SM) models. In these models, the solution domain is divided into two main regions: (1) Rotor: inner region containing the rotating impeller and (2) Stator: outer region containing the stationary baffles and vessel walls. For the MRF model, steady-state calculations are performed with a rotating frame of reference in the impeller region and a stationary frame of reference in the outer region. For the SM model, the impeller region slides relative to the outer region in discrete time steps and time-dependent calculations are performed using implicit or explicit interpolation of data at consecutive time-points. Although the SM method is more accurate for the modeling of actual phenomenon such

as impeller rotation as it is time dependent, it is computationally demanding. In this work, the MRF method was used and the MRF zone was created around the Rushton blades and the shaft as shown in figure 6.

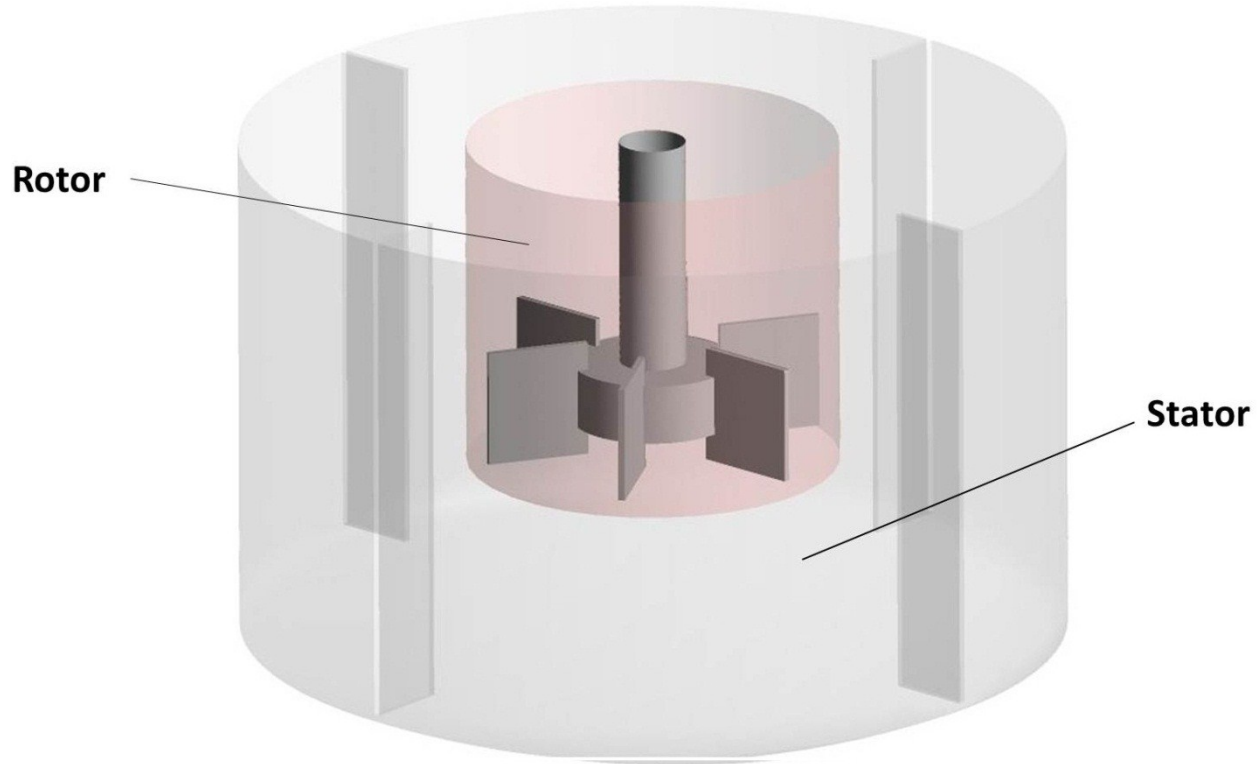


Figure 6 3D Schematic view of the reactor domain showing MRF zone

3.2.4 Method of solution

In this work, all the computational work was performed in double precision mode using the commercially available CFD code package, ANSYS Fluent 17.1. The pressure-based solver is used to numerically solve the continuity and momentum equations for the velocity and pressure fields. A coupled SIMPLE scheme was chosen for the pressure-velocity coupling method. This algorithm uses a relationship between velocity and pressure correction to enforce conservation of continuity and to attain the required pressure field. All governing equations, described earlier, were discretized by ANSYS Fluent software using the finite volume approach with a First-Order upwind discretization scheme. Then, an Eulerian multiphase method implemented in the software was applied. Liquid phase was considered the continuous phase (primary phase) and the

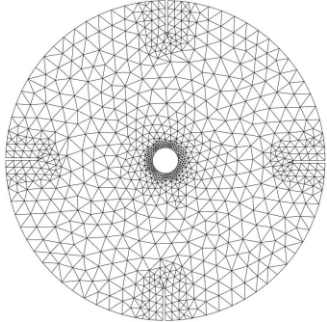
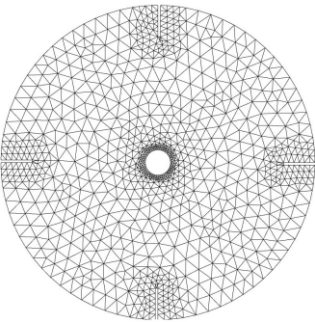
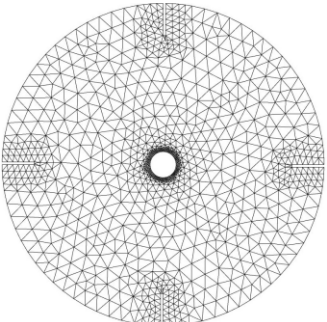
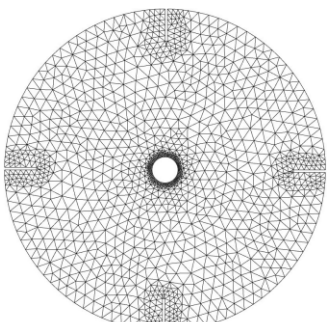
solid was considered the dispersed phase (secondary phase). The pressure outlet boundary condition was set to the reactor outlet. All walls were assumed as no-slip wall boundaries. The time step size used in the model was initially 0.001s and, as the solution converged, the time step size was gradually increased to 0.01s to save computational time. The simulation was performed for a time span of 3600s. All computations were performed with 48 paralleled processors. (For more numerical settings, see table A1)

3.2.5 *Grid study*

As it is important in such modeling to employ an adequate number of computational cells, the geometry divided into more than 2×10^5 3-D tetrahedral computation discrete control volumes or cells by the commercial grid generation tool, ANSYS Workbench 17.1.

To assure that the results were independent of the mesh size four different tetrahedral grid configurations were chosen to check mesh independency. Also, in order to capture the complex flow behavior around both the impeller tip and at the baffle edges, a refinement factor was used in these regions. The difference between these four grids resulted from the grid size and the refinement factor used, as can be seen in Table 4:

Table 4 Different Applied Grids and Number of Cells

Grid NO.	Number of cells	Grid size (mm)	Refinement factor	
1	1.9×10^5	5.5	Around Baffles: 1 Around Impeller:1	
2	2.2×10^5	5	Around Baffles: 1 Around Impeller:1	
3	3.5×10^5	5	Around Baffles: 1 Around Impeller:2	
4	4.5×10^5	4	Around Baffles: 1 Around Impeller:2	

The liquid phase velocity at three different points (points A, B and C) shown in figure 7 and the volume averaged liquid phase velocity over the whole domain were chosen to study the grid sensitivity of the model.

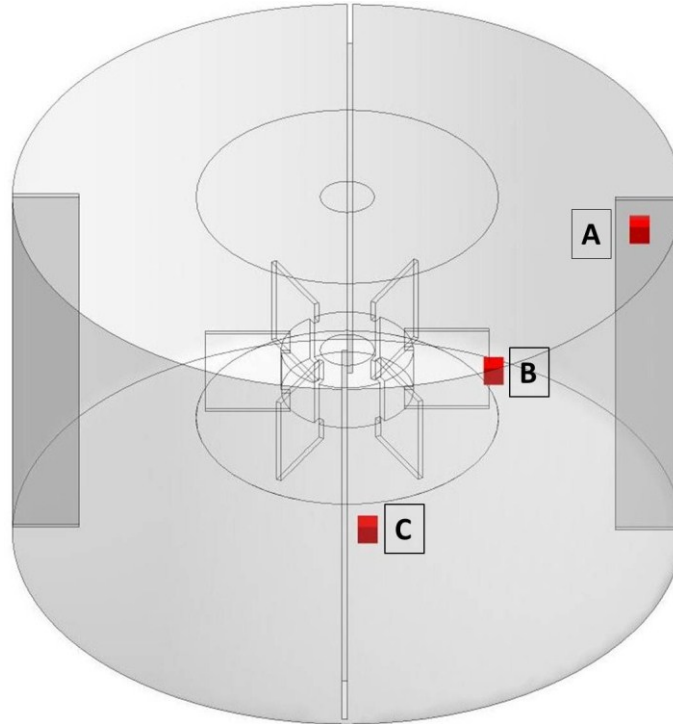


Figure 7 Three different positions selected for comparing liquid phase velocity, A: near the top, B near the tip of impeller, and C near the reactor bottom

3.3 CFD-PBM Coupling Theory and Implementation

3.3.1 Introduction

The Population Balance Model (PBM) is a well-established mathematical framework for dynamic modeling of systems containing a number of particles such as those in precipitation, polymerization, etc.[95]. In crystallization systems, PBM characterizes the transformation of crystal identities by forming a balanced equation to calculate the number of crystals in the system. Solving these balance equations defines the distribution of the number of particles in the time frame or spatial frame, as well as the characteristic size of the crystals.

CFD and Population Balance Model (PBM) have some limitations when used independently. In a solid-liquid two phase CFD simulation, a two-fluid model is generally applied, while a constant

Sauter mean diameter represents the different sizes of the particles in the dispersed phase. In the case of widely ranging particle size, this approach is more likely to fail. Also, particle size changes, due to aggregation or breakage, are not considered in CFD models. On the other hand, PBM needs some flow information, such as particle velocity and energy input, which are generally considered in highly simplified forms in pure PBM models. In the real world, any changes in particle size could affect the hydrodynamic behavior of the model and these effects should be considered dynamically. Undoubtedly, a constant diameter cannot express these effects. Accordingly, coupling CFD with PBM seems beneficial for the predictive strength of both of them.

A CFD-PBM coupling technique was born at the beginning of twentieth century and at this point has gained a high degree of attention. Today, coupled CFD-PBM models are widely used, especially in gas-liquid two-phase simulations and scarcely in the solid-liquid two phase simulations. Coupling PBM with CFD divides particle size distribution into N discrete size classes, assuming that all the particles in each of the classes share a common velocity field. In fact, in each time step, the solid volume fraction and particle velocity obtained by solving the mass and momentum conservation equations are applied to calculate the particle growth and aggregation kernels (if applicable) in PBM. Then by solving the PBM, the Sauter diameter is attained and used to solve for interphase forces in CFD code and provides an initial guess for the next time step. Figure 8 shows this interrelation schematically.

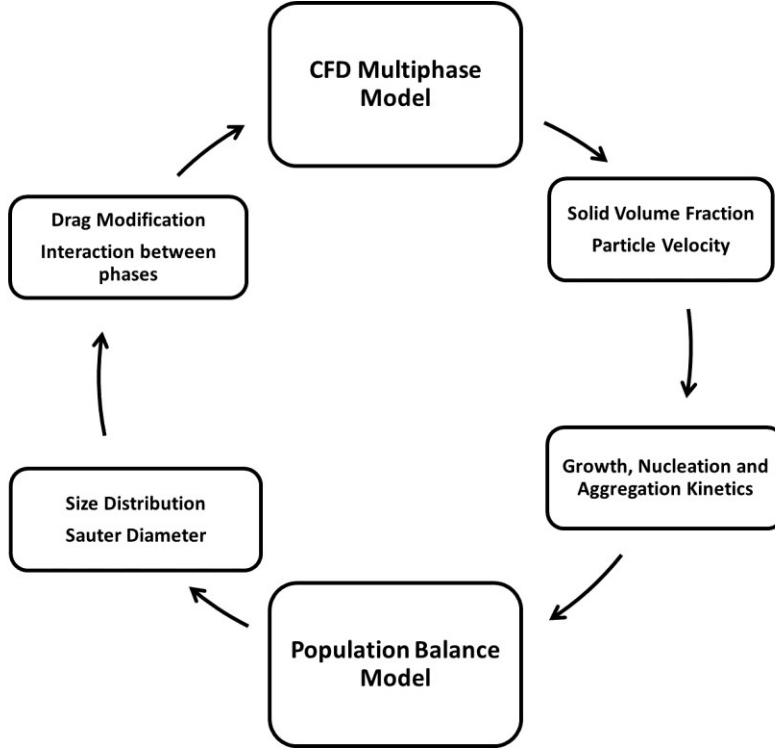


Figure 8 Schematic diagram of Multiphase CFD-PBM model

3.3.2 Governing Equations

The population balance equation (PBE) provides a simple form of population continuity for any phenomena. It can be derived as a balance for particles in a physical space. The general form of PBE is defined as:

$$\frac{\partial}{\partial t} [n(V, t)] + \nabla \cdot [\vec{u}n(V, t)] = B_{agr} - D_{agr} + B_{brk} - D_{brk} \quad (3-22)$$

where D_{agr} and B_{agr} are death rate and birth rate of particles, respectively, of volume V due to aggregation, while D_{brk} and B_{brk} represent the death rate and birth rate of particles of volume V due to breakage, respectively. Aggregation rate and breakage rate are defined as follows:

$$B_{agr} = \frac{1}{2} \int_0^V a(V - V', V') n(V - V') n(V') dV' \quad (3-23)$$

$$D_{agr} = \int_0^\infty a(V, V') n(V) n(V') dV' \quad (3-24)$$

$$B_{brk} = \int_{\Omega_v} v g(V') \beta(V|V') n(V') dV' \quad (3-25)$$

$$D_{brk} = g(V) n(V) \quad (3-26)$$

As D_{agr} and B_{agr} describes the aggregation kernel and D_{brk} and B_{brk} describes the breakage kernel. As discussed above, to link population balance modeling of the secondary phase with fluid dynamics, Sauter mean diameter (d_{32}) will be used to represent the particle diameter of the solid (secondary phase) in each calculation step. Sauter mean diameter can be obtained from:

$$d_{32} = \frac{\sum n_i d_i^3}{\sum n_i d_i^2} \quad (3-27)$$

which illustrates the diameter of the sphere that has the same “*volume/surface area*” ratio as the average particles.

3.3.3 Precipitation Kinetics: previews works

Precipitation phenomena are generally well described by the population balance model. Precipitation processes may involve nucleation, crystal growth, aggregation, and also breakage of existing crystals.

Finding the appropriate kinetic parameters for struvite precipitation is an important part of such phenomena. To the best of the author’s knowledge, a number of studies have been performed regarding the kinetic aspect of the struvite precipitation process. Some studies presented a first-order kinetic model for struvite growth while neglecting nucleation and aggregation mechanisms. A few other studies investigated more complex equations for precipitation kinetics, especially growth and, sporadically, nucleation. Based on the different experimental methods and different assumptions, different kinetic rates have been shown. Table 5 presents a summary of recent related studies.

Table 5 Recent studies related to Precipitation kinetic and predicted coefficients

Experimental Condition	Mathematical Method/Solver	Growth Rate	Nucleation Rate	Aggregation Rate	Ref.
Synthetic & real urine	Turbidity measurement/ least square method/ PBM discretization	k=1.5-2 (µm/s) n=1.15-2	A = 3.4-6.7×10 ⁹ (#/m ³ s)	–	[78]
Synthetic solution/continuous and batch reactor	gPROMS process simulation software	k=45-59 (µm/h) n=1.45-1.68	–	–	[44]
Synthetic solution/batch reactor	gPROMS process simulation software	k=12.49 (µm/ min) n=5.062	k=8.5× 10 ⁷ (#/L min) n=1.680	k=3.721×10 ⁻⁷ (L /min) n=5.259	[80]
Synthetic solution/batch reactor	Reconstruction of crystal size distribution/Laplace transform method	kg=10 ⁻⁷ -10 ⁻³ (m/ s) g=1-2	A = 10 ⁶ -10 ¹³ B = 0-10	–	[46]
Synthetic solution/batch reactor	Experimental method First order and second order kinetic	kg=0.5 – 10×10 ⁻⁹ (m/ s) g=1.05-1.47	–	–	[73]

Finding the dominant phenomena in struvite precipitation and the effect of each phenomenon on production of crystals has been studied by researchers. Le Corre et al. [96] showed that aggregation and breakage phenomena are insignificant in struvite precipitation. Other researchers [88, 97] also found out that the lower the solution supersaturation, the lower the chance of aggregation and by decreasing the pH and the solution supersaturation, aggregation will be hindered. In this work, as explained earlier, the initial solution was prepared to somewhat limit nucleation and aggregation. Therefore, the kinetic model has been selected based on the

assumption that nucleation and aggregation are negligible and a size-independent growth kernel was used.

3.3.4 Growth rate

Crystal growth rate can be described as a function of the solution supersaturating index SI (defined earlier) as follows:

$$G(t) = \frac{dL}{dt} = k_g SI^n \quad (3-28)$$

where k and n are the kinetic coefficients. In this work, the coefficient estimated by Ali and Schneider[44] was used and growth rate is added into the simulation through User Defined Function (UDF) (See Appendix III).

3.3.5 Implementation of PBM in Fluent

In ANSYS Fluent, the population balance model is provided as an add-on module which could be loaded through a text user interface (TUI) (see appendix II) offering three different solution methods to the population balance equation: discretized population balance, standard method of moments, and quadrature method of moments. In the present study the discretized method, also known as the method of classes or sectional method, which was developed by Ramkrishna [95], Hounslow et al. [98] and Lister et al.[99], is implemented.

In this method, the continuous particle population is discretized into a finite number of size intervals or bins. Although this approach has the advantage of computing the particle size distribution directly, it requires a priori knowledge of the bin sizes and may need a large number of classes to cover the whole range of particle sizes. In this work, 25 size classes were used as “Bins” to cover the entire range of particles. Table 6 shows these bins and relevant diameter of each bin.

Table 6 List of selected bins and related diameters

Bin index	0	1	2	3	4	5	6	7	8	9	10	11	12
Size (µm)	152	133	116	101	88.6	77.3	67.5	59	51.5	44.9	39.2	34.3	29.9
Bin index	13	14	15	16	17	18	19	20	21	22	23	24	-
Size (µm)	26.1	22.8	19.9	17.4	15.2	13.3	11.6	10.1	8.82	7.7	6.72	5.86	-

After performing different experiments with differing initial SI values and measuring the CSD at different time intervals, these 25 size classes were chosen as they covers the entire detected size range. It is important to note that the particle size analyzer never detected any particle outside of this size range in any of the experiments. This indicates that selected ranges cover all of the existing particles. One possible source of error in discretizing the size range could be selecting different intervals as PSA selected intervals. To avoid this error, the exact same bins, as reported by the machine, have been applied to the model through a probability density function (PDF) file.

4 RESULTS AND DISCUSSION

4.1 Grid sensitivity results

Four simulations were carried out to understand the influence of mesh configuration on the flow prediction. The detailed profile for each grid case and the grid study results are presented in table 7.

Table 7 Results of grid independency

Case Number	Number of Cells	Liquid phase velocity at point A (m/s)	Liquid phase velocity at point B (m/s)	Liquid phase velocity at point C (m/s)	Average Liquid phase velocity (m/s)
1	1.9×10^5	0.0153	0.233	0.0680	0.0619
2	2.2×10^5	0.0266	0.256	0.0764	0.0623
3	3.5×10^5	0.0282	0.259	0.066	0.0624
4	4.5×10^5	0.0288	0.260	0.0571	0.0625

As shown in table 7, the results are grid independent. The grid independence check was done to find the optimized number of computational grids. In this test, the liquid phase (primary phase) was a mixture of water with the struvite constituent ions, and the solid phase (secondary phase) was struvite particles. By monitoring the average liquid velocity over the reactor volume, it was shown that the system stabilized and solution converged. As the difference between numerical results in grid 2, 3 and 4 were non-significant; grid 2 was chosen for the simulation as it runs faster.

4.2 Flow Pattern Prediction

For any CFD simulation, it is desirable to validate the CFD prediction of the flow field before commencing any further steps. The best way for this validation is to measure the velocity of fluid from different locations of the reactor by experimental techniques such as “Laser Doppler Velocimetry (LDV)” and comparing the results with velocity predicted by the model. As using these techniques were not accessible in this work, this validation was performed by other experiments of other researchers, as this is a commonly used method for model validation.

Impeller power value, overall flow pattern, and velocity magnitude distribution were chosen as parameters to validate the hydrodynamic behavior of the CFD model.

4.2.1 Power Number Prediction

The impeller power number N_p has been commonly used to check the validity of CFD simulation of single phase flow in stirred tanks [100-102]. In this work simulation was conducted for both single phase flow (water) and multiphase flow (mixture) as a validation technique for multi-phase flow, and power results were compared with experimental values reported by Rushton et al. [103]. Power numbers were calculated from the model prediction torque for a wide range of Reynolds numbers, from laminar to turbulent flow regimes, and based on the following equations:

$$Re = \frac{\rho N D_I^2}{\mu} \quad (4-1)$$

where ρ is the density (kg/m^3), μ is viscosity (kg/m.s), D_I is the tip-to-tip impeller diameter and N is the impeller speed (s^{-1}).

$$P(W) = 2\pi N (s^{-1}) M (Nm) \quad (4-2)$$

where P is the power needed for rotating the impeller (W), N is the speed of rotation (s^{-1}) and M is the torque (Nm). The power numbers were then calculated as dimensionless numbers to generalize power factor for any case as follows:

$$Po = \frac{P (W)}{\rho (Kgm^{-3}) N (s^{-1})^3 D (m)^5} \quad (4-3)$$

where ρ is the fluid density (Kgm^{-3}) and D is impeller diameter (m). It should be pointed out that for Reynolds number less than 10, equation (4-3) is not valid.

To cover a complete range of fluid regimes, the simulation starts with Reynolds = 10 and a corresponding speed of 0.2 rpm. The other Reynolds numbers were simulated by changing the speed of agitation. Reynolds number of 10, 100, 200, 1000, 5000, 10000, 25000, and 50000 were simulated. For the turbulent regime the RNG k- ϵ model was chosen, as it is used for further

steps, and for Reynolds numbers lower than 200, laminar flow was chosen since $Re = 200$ is the boundary of laminar flow in stirred tanks with Rushton impellers [104].

The results for this comparison are shown in figure 9.

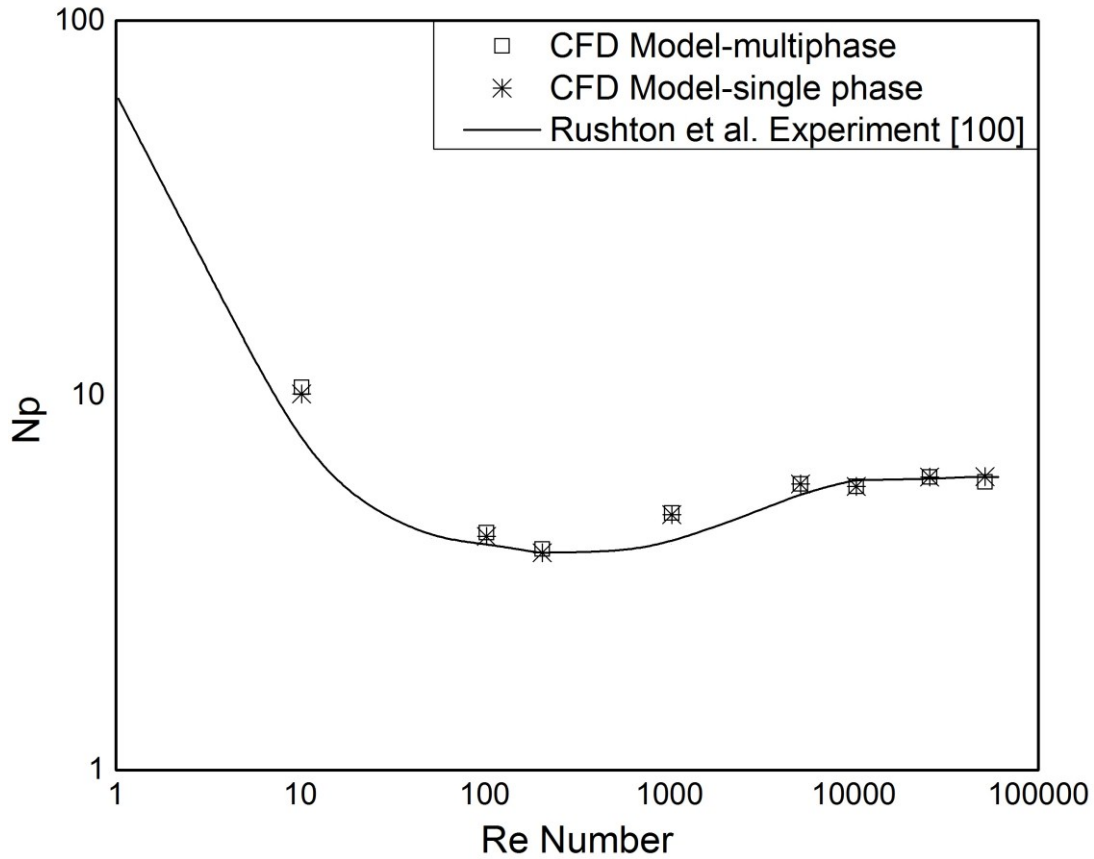


Figure 9 Comparison of experimental and CFD model (single phase and multiphase) predicted impeller power number

As is obvious, the model prediction for single phase flow is in agreement with the Rushton et al. [103] experimental data. Similar results obtained for multiphase flow show satisfactory agreement with the single-phase results, as well as experimental data. This correspondence in the single phase and multiphase flow results was expected since the solid volume fraction in this work is in the range of 10^{-4} . The highest percentage of error ($\sim 17\%$) occurs at $Re = 10$. A possible reason for this discrepancy is the effect of baffles used for development of mixing conditions which can disturb the laminar flow regime in $Re = 10$.

4.2.2 Overall Flow Pattern

An assessment of the accuracy of the CFD model to predict flow field could be conducted by comparing the velocity vector configuration with the LDV results of previous studies. Costes and Couderc [105] investigated the hydrodynamic characteristics of the flow induced by a standard Rushton impeller. They reported mean velocities in two vertical planes; the median plane between two baffles ($\theta = 45^\circ$) and the plane of the baffles ($\theta = 0^\circ$). Figure 10 and 11 show the CFD model velocity prediction in comparison with Costes and Couderc [105] results in the plane of baffles and in a median plane between two baffles, respectively.

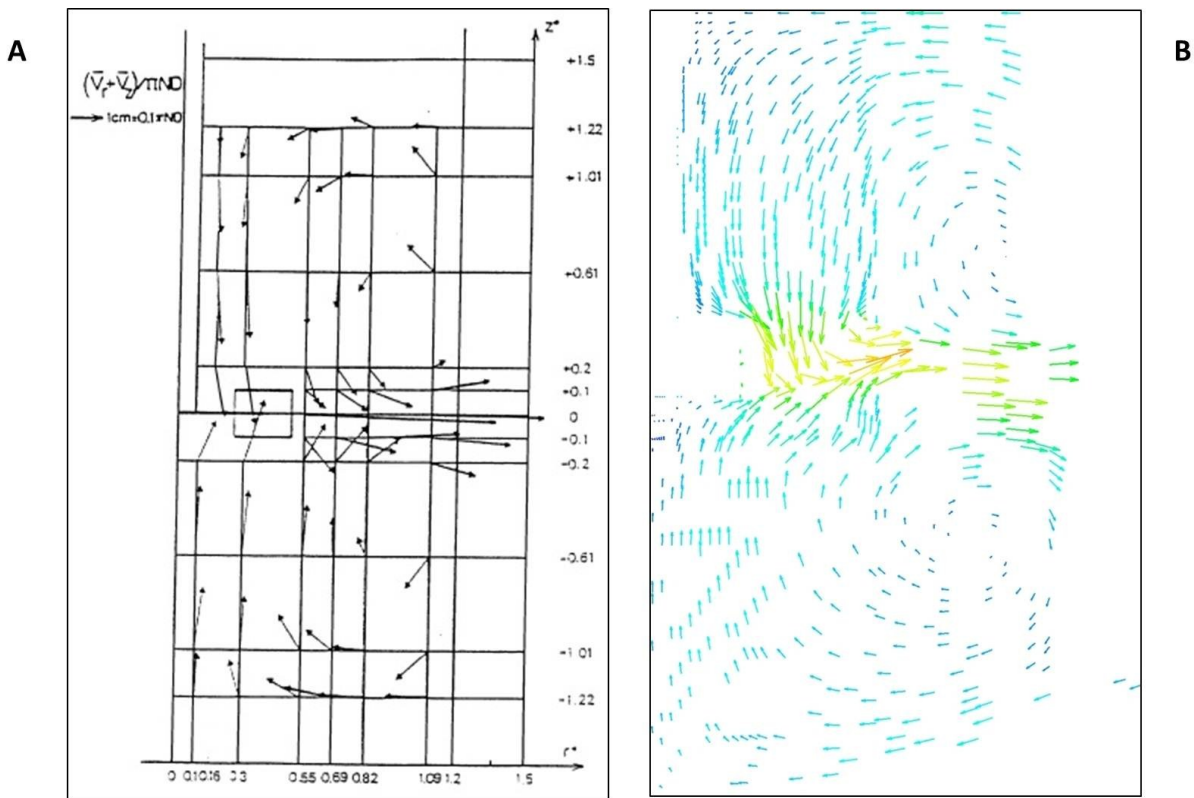


Figure 10 Comparison of (A) experimental results by Costes and Couderc [105] flow pattern with (B) flow pattern prediction obtained by the CFD model for a vertical plane containing a baffle ($\theta = 0^\circ$).

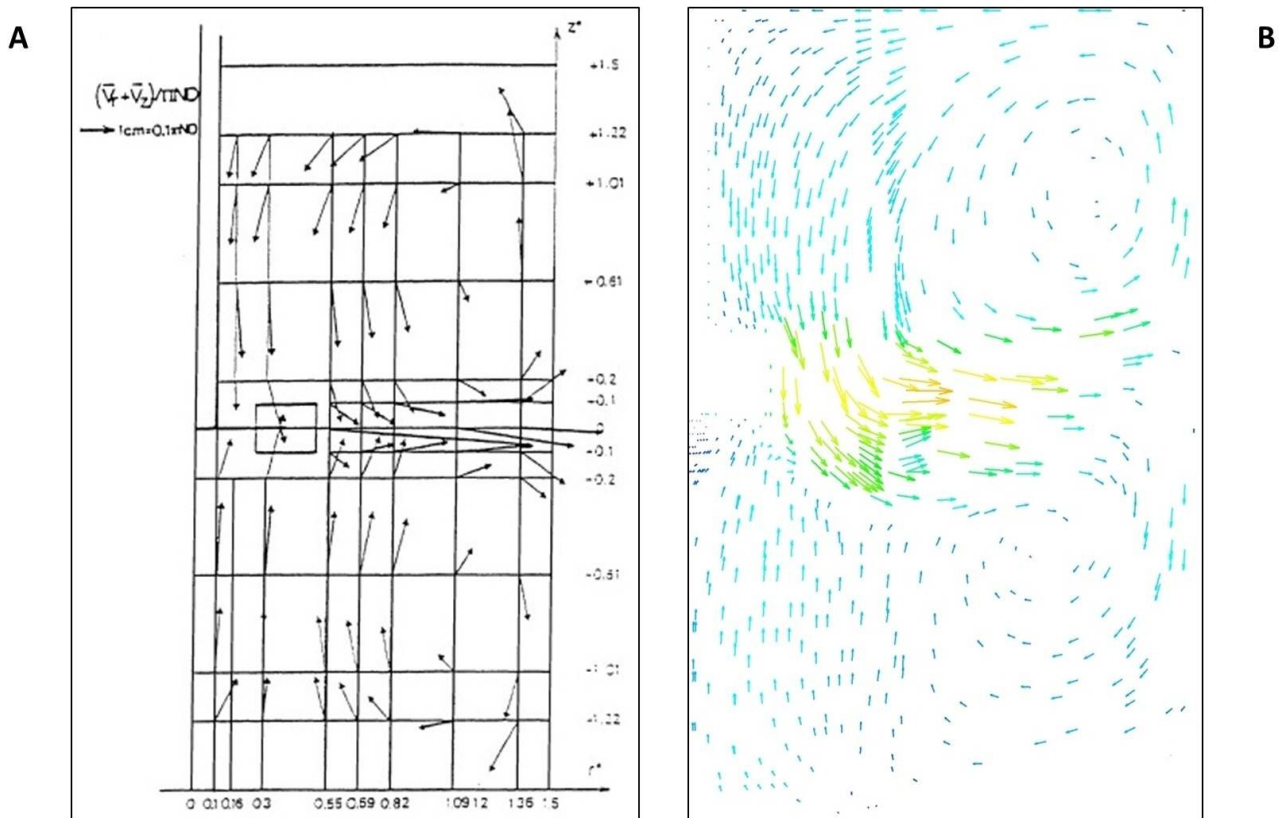


Figure 11 Comparison of (A) experimental results by Costes and Couderc [105] flow pattern with (B) flow pattern prediction obtained by the CFD model for a vertical plane between baffles ($\theta = 45^\circ$).

The circulation pattern of the flow is correctly reproduced. The position of the recirculation centers is in accordance with the experimental results, showing that as we expected, Rushton turbine is a radial flow type of impeller, as the axial velocity components are almost vertical at the top of the blades. Also, the intensity and direction of the radial flow jets from impeller tip toward the reactor walls are also correctly predicted.

It is important to note that the flow pattern and recirculation arrangement are quite independent of the stirrer speed and of the size of the reactor as reported by Costes and Couderc [105] and also the qualitative nature of the multiphase flow field around the impeller and shape of the flow jet is similar to that of single phase flow, especially for low solid concentration as investigated by Wadnerkar et al. [106].

4.2.3 Velocity Magnitude Distribution

Another parameter which a CFD model should be able to predict is the velocity magnitude distribution in a stirred tank. Here, the contour for the velocity is shown in figure 12, which presents the velocity profile as predicted with the CFD model.

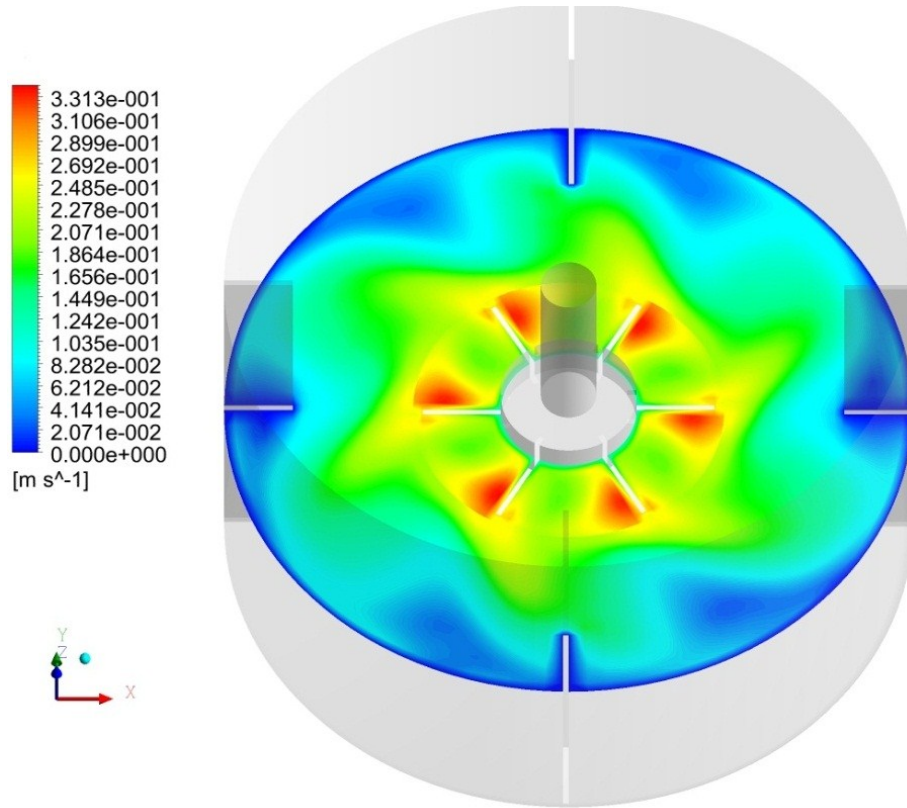


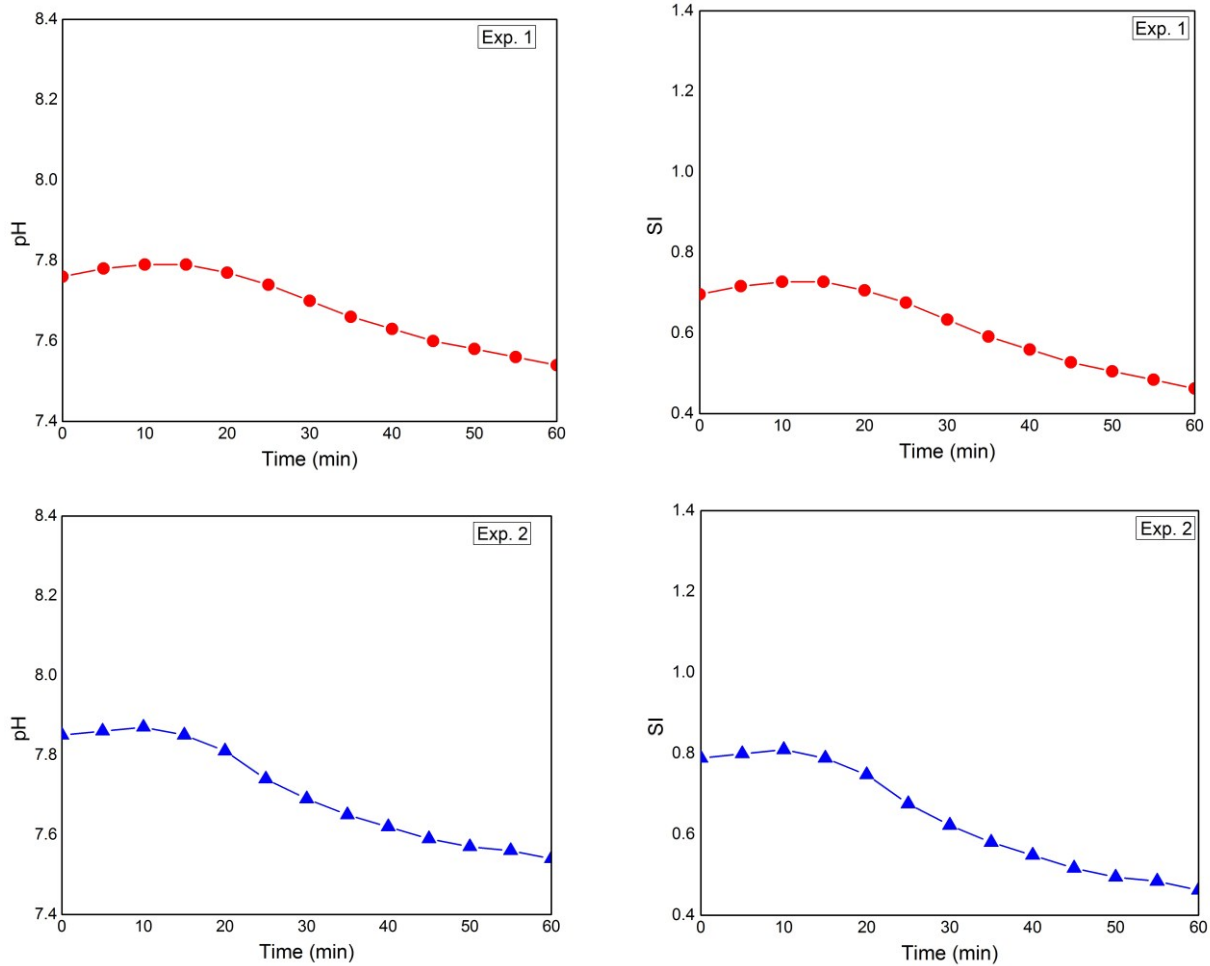
Figure 12 Velocity contours on a horizontal plane at the middle of impeller

As can be seen, velocity magnitude decreases according to the increased radius and the highest magnitude velocity occurs at the impeller tip, as expected.

4.3 Supersaturation Prediction

In this section, the results of supersaturation index variation over time will be compared with the values predicted by CFD model. First, to find a suitable initial pH in the metastable zone, as discussed earlier, five different experiments with different initial pH were conducted to select the best initial pH for main experiment. To find the SI values at every experimental time interval, pH measurement was the best method as the total concentration of Mg, N, and P are constant and

any change in the pH will affect the value of SI. Therefore, the value of pH was measured every 5 min from $t = 0$ (seeding moment) to $t = 60$ min in all experiments mentioned in table 3. Then the SI value for each data was calculated by the thermodynamic model. The pH and SI variation with time for all experiments are shown in figure 13.



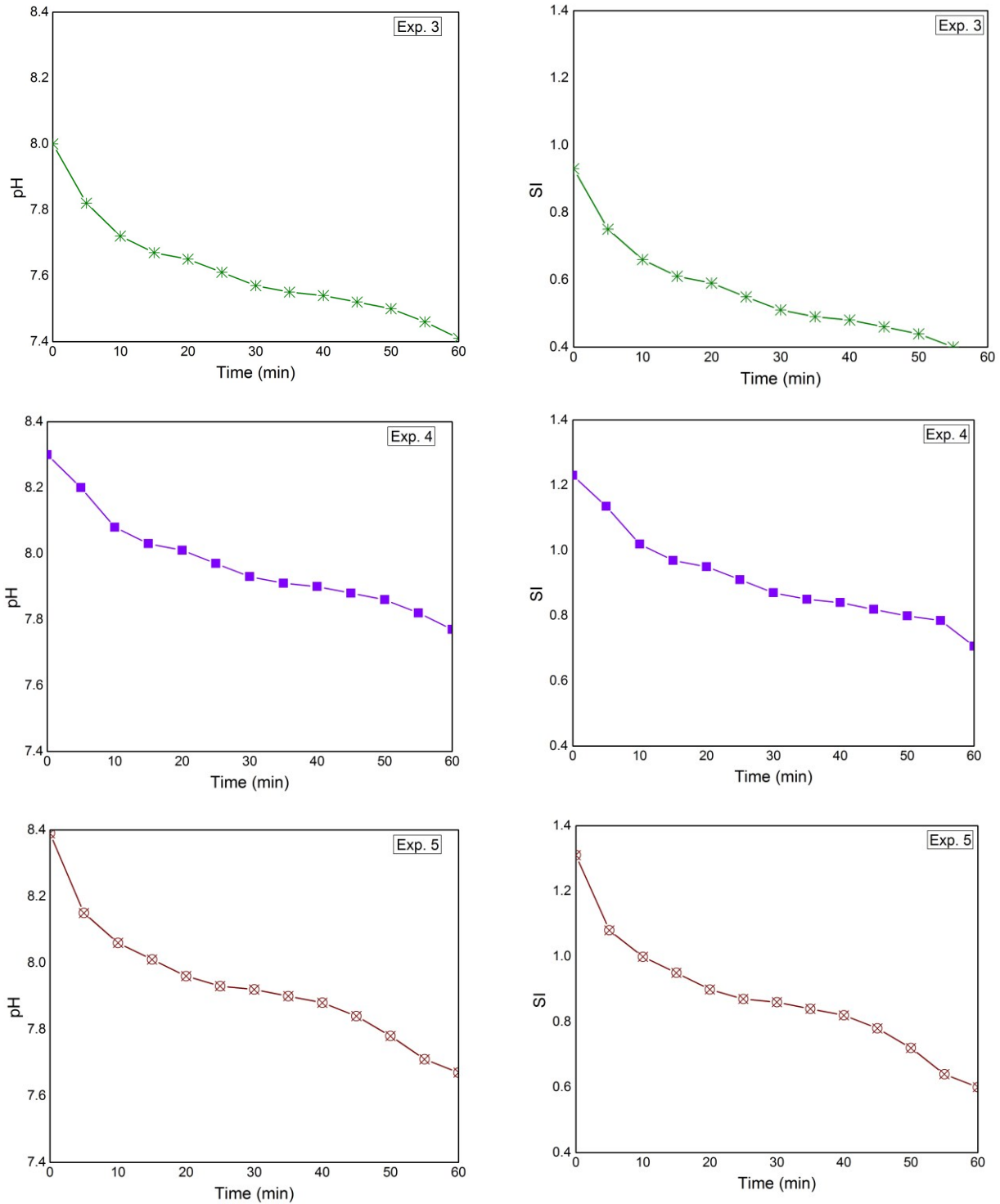


Figure 13 pH and SI variation with time for different initial conditions experiments

As figure 13 shows, in experiments number 1 and 2, pH stayed constant or even increased for about 20 min from the beginning of experiment. In experiments number 4 and 5, SI also dropped

very fast and, as discussed earlier, there is higher chance of aggregation in these two experiments. Therefore, experiment number 3 was chosen as the main experiment. Figure 14 shows the pH variation over time for experiment 3:

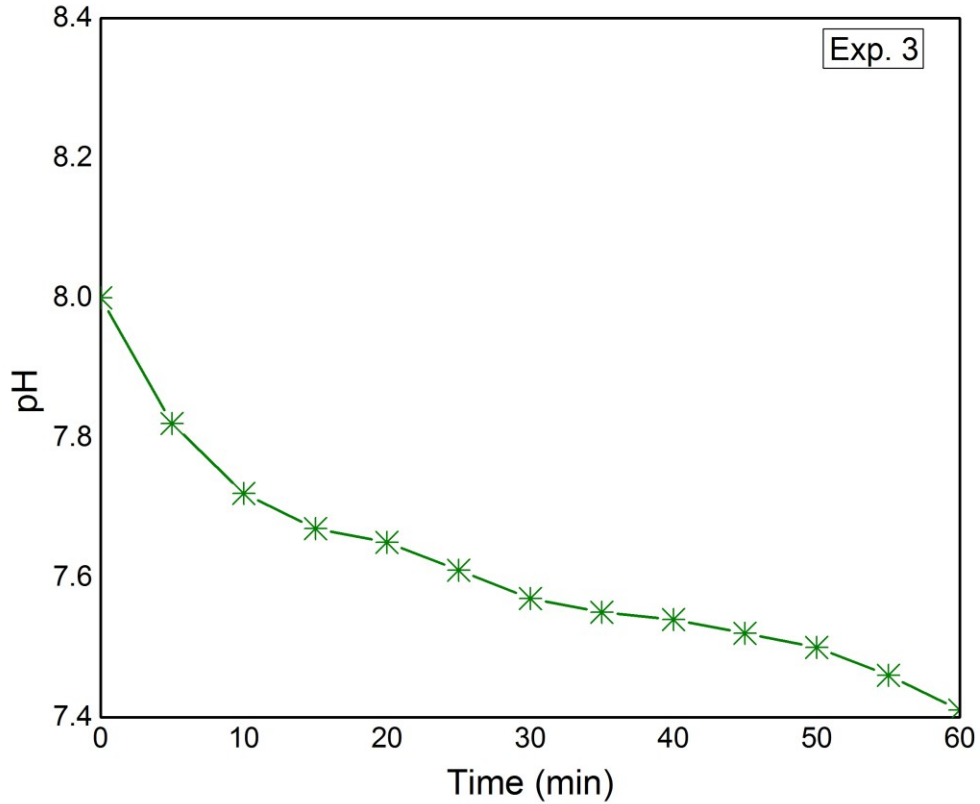


Figure 14 Experimental pH variation with the time

The decrease in the pH shows that precipitation does occur, since with precipitation, constituent ions will move from liquid phase to solid phase and changing the speciation of the solution. Based on equation (3-1), as struvite precipitates, it releases hydrogen ions in solution, causing a drop in pH.

Based on the pH measurements, the supersaturation index was attained at different experimental time intervals using thermodynamic model solver. Figure 15 shows the thermodynamic model results as compared with the CFD model.

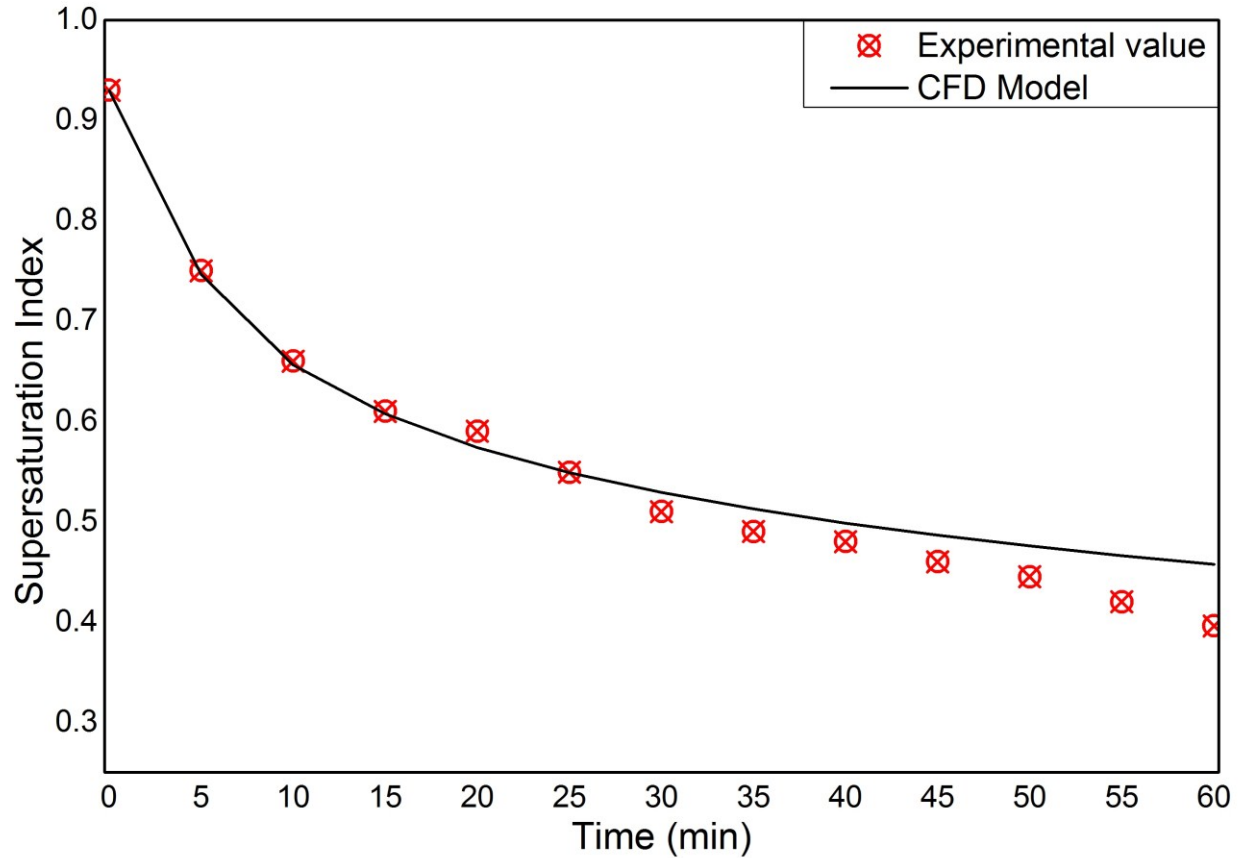


Figure 15 Experimental and CFD model predicted Supersaturation index

The developed model is successfully predictive of a number of items. First, the model predicts the SI values with an acceptable accuracy. This parameter is a key value as growth rate and particle size distribution are dependent on this parameter. The maximum amount of error was 24%, belonging to the supersaturation index at 60 min. Considering the error bars, this model predicts the supersaturation state of the solution correctly, barring the last value.

4.4 Crystal Size Distribution (CSD)

Further to SI prediction, the model successfully predicts the particle size distribution. As described in previous section, crystal size distribution was measured at a number of time intervals: after 3, 10, 20, 30, 40, 50 and 60 min from starting of precipitation (seeding). The crystal size distribution results and the CSD predicted by the model are shown below in figures 16 to 23.

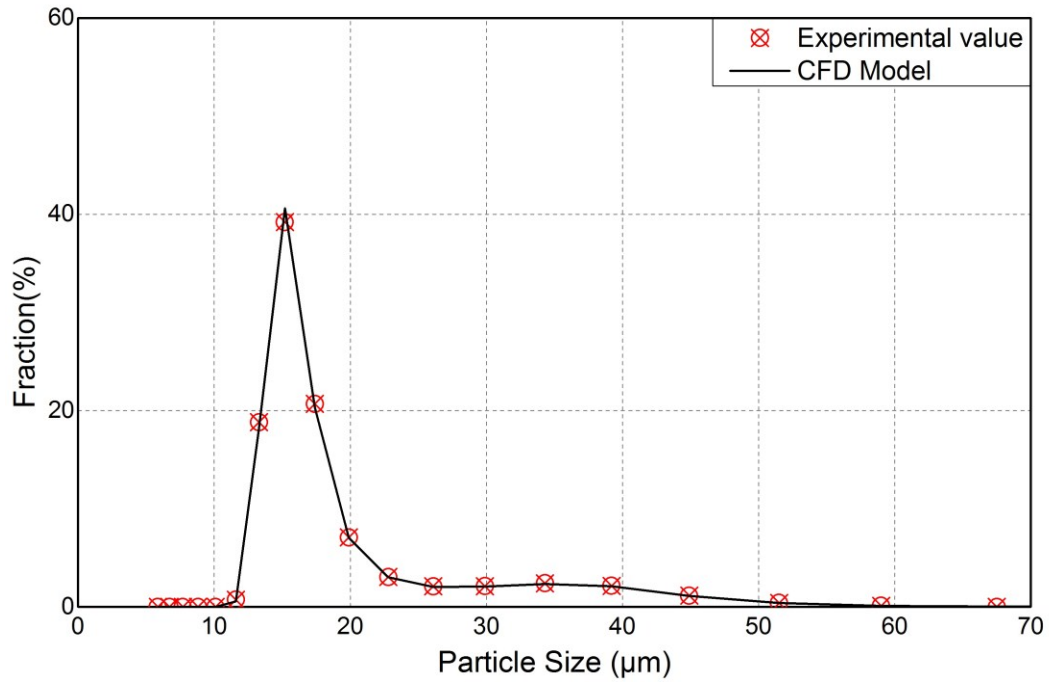


Figure 16 Experimental averaged and CFD model predicted CSD at time = 0 (seed) - Number based distribution

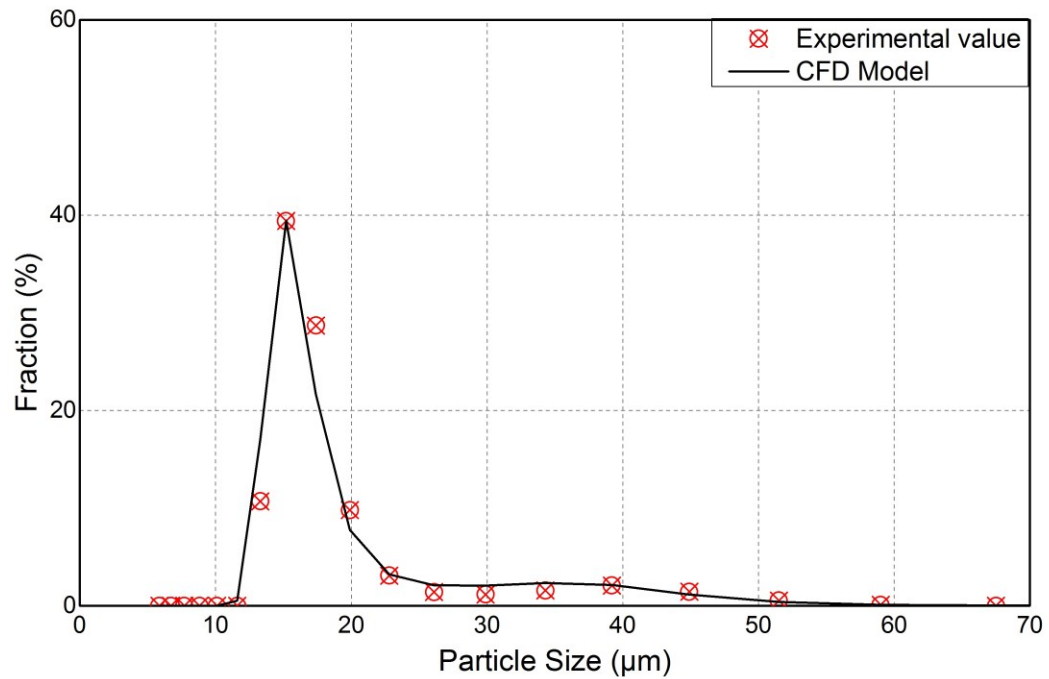


Figure 17 Experimental average and CFD model predicted CSD at time = 3min - Number based distribution

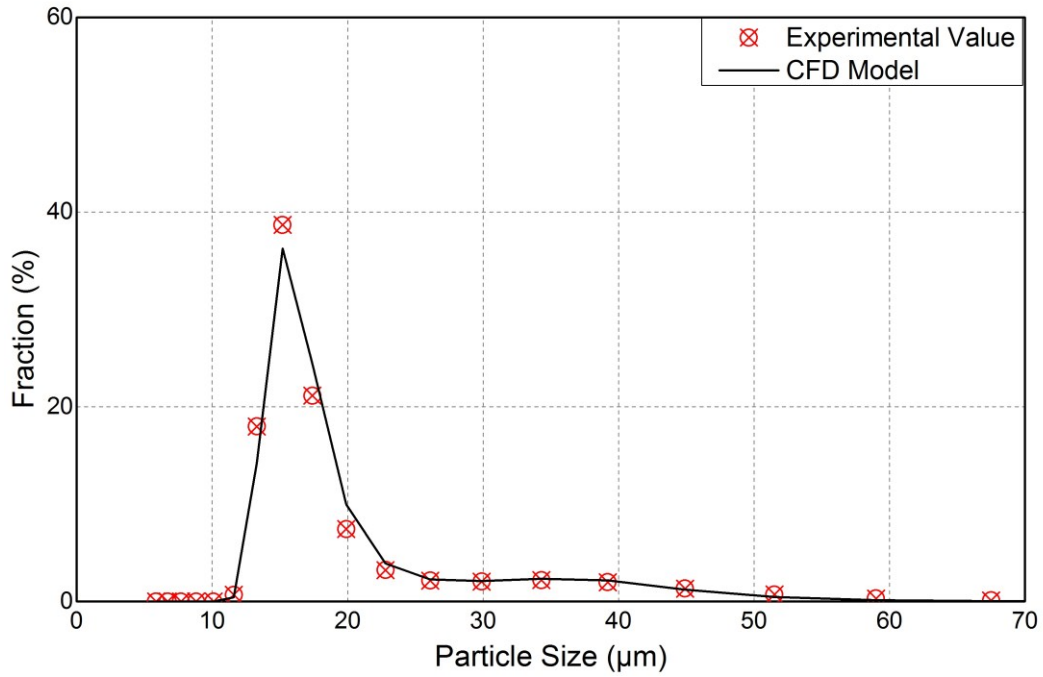


Figure 18 Experimental averaged and CFD model predicted CSD at time = 10 min - Number based distribution

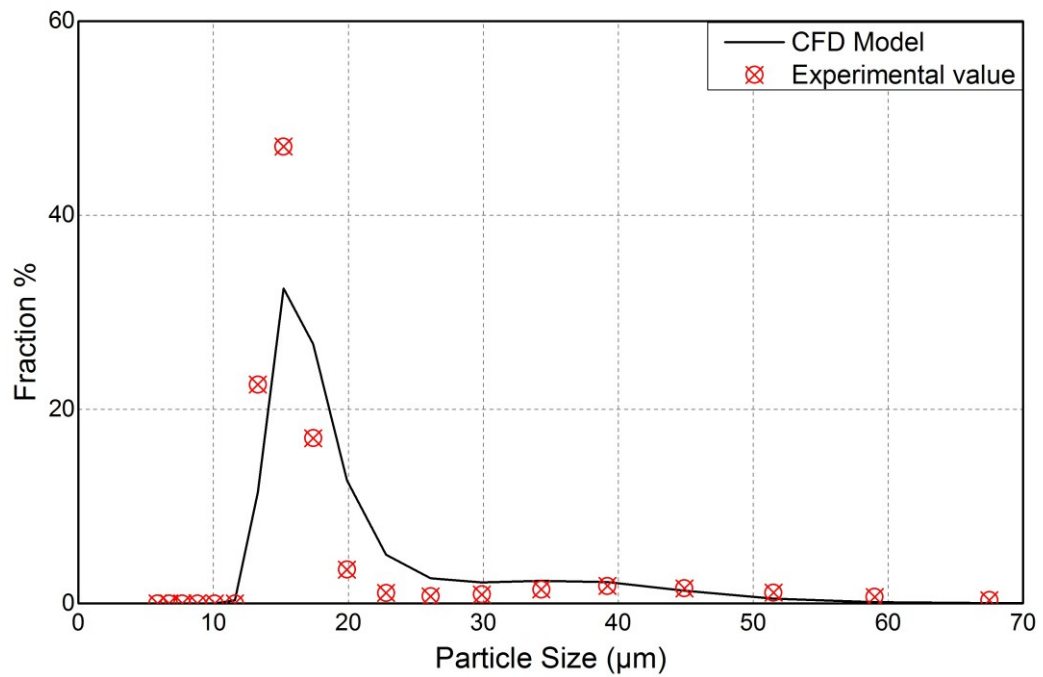


Figure 19 Experimental averaged and CFD model predicted CSD at time = 20 min - Number based distribution

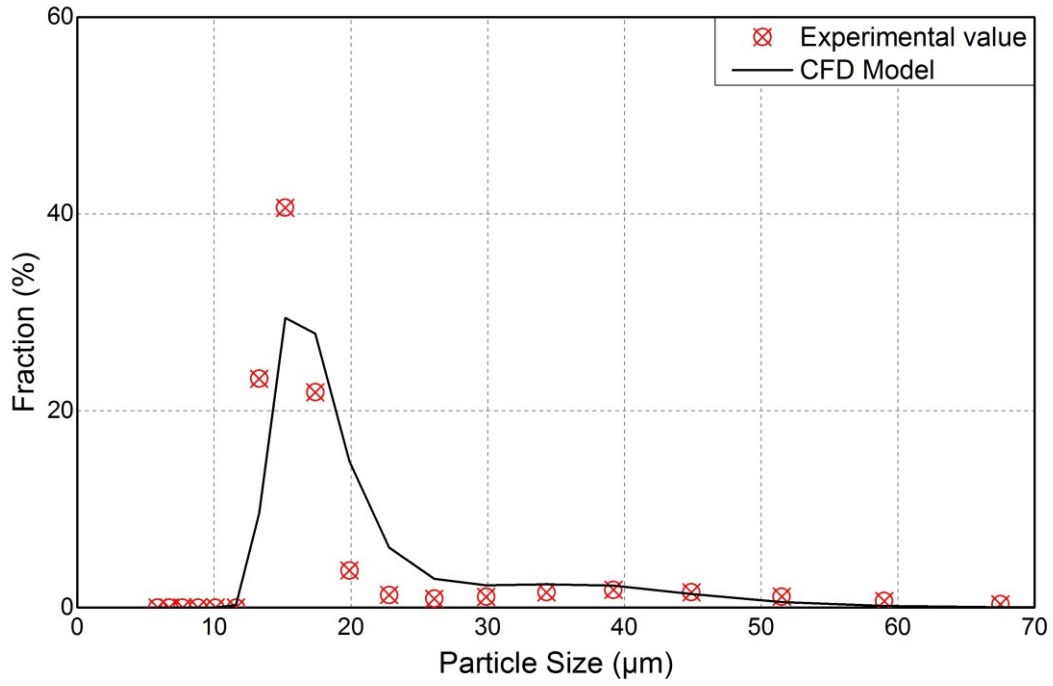


Figure 20 Experimental averaged and CFD model predicted CSD at time = 30 min - Number based distribution

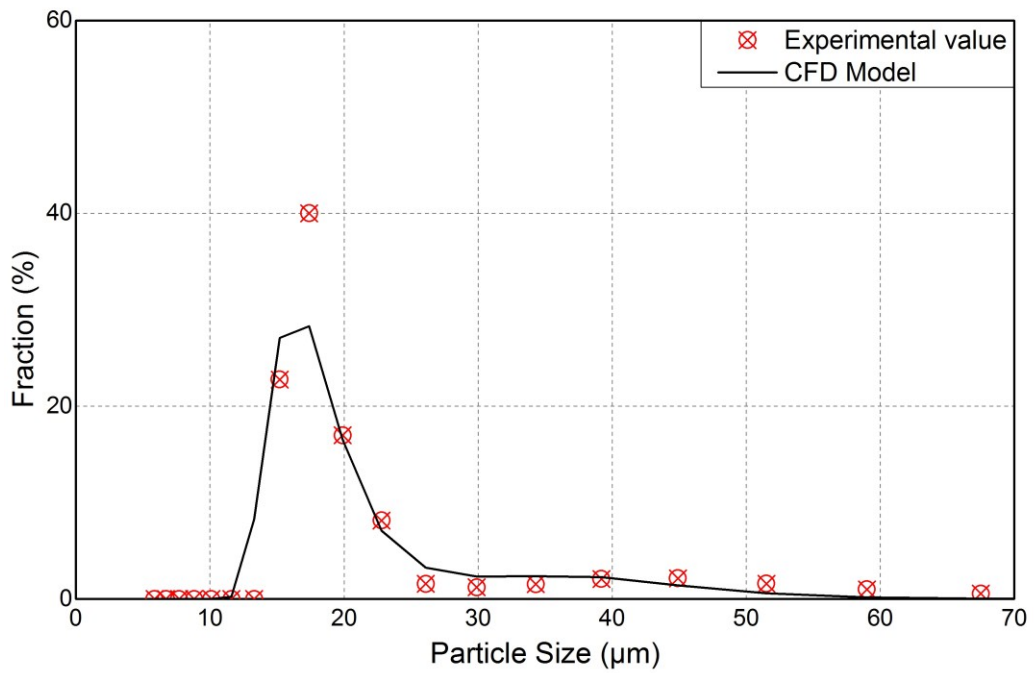


Figure 21 Experimental averaged and CFD model predicted CSD at time = 40 min - Number based distribution

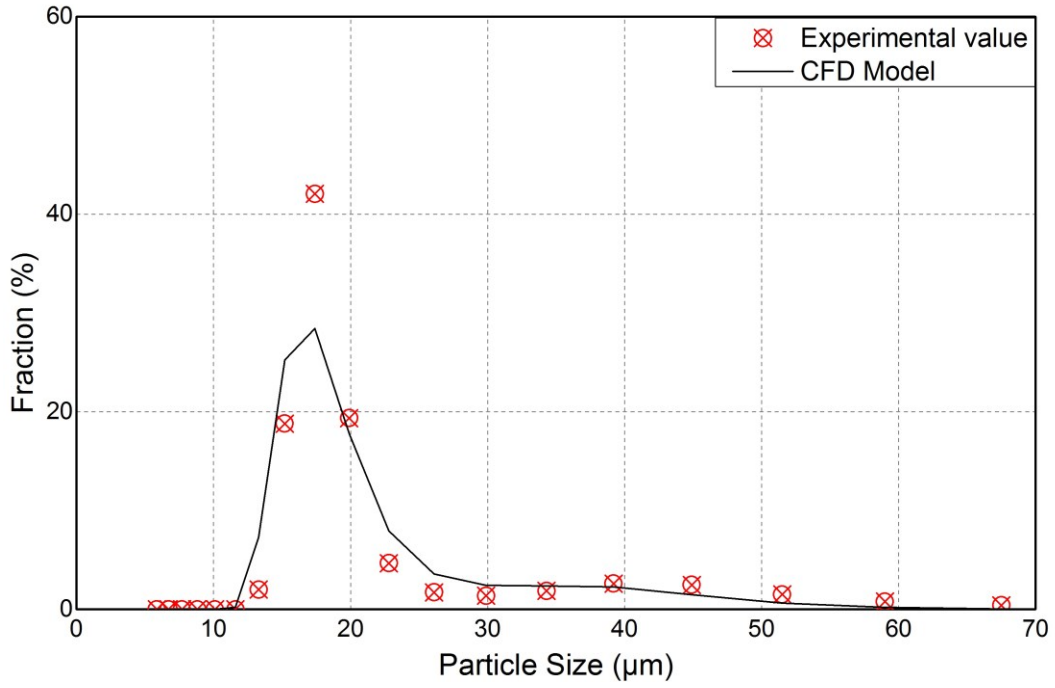


Figure 22 Experimental averaged and CFD model predicted CSD at time = 50 min - Number based distribution

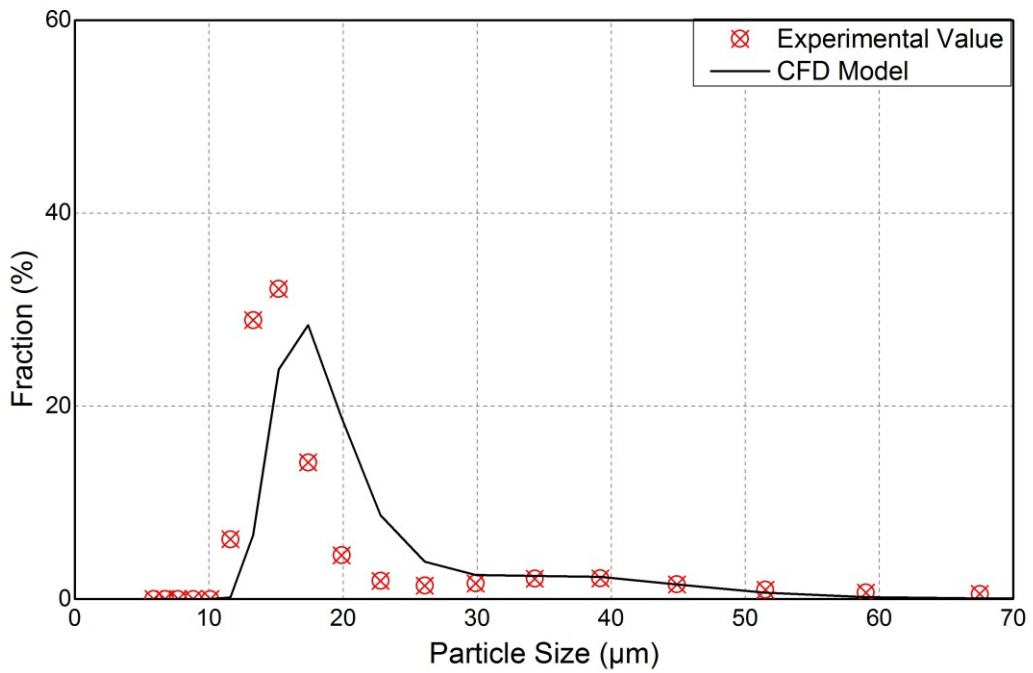


Figure 23 Experimental averaged and CFD model predicted CSD at time = 60 min - Number based distribution

As is dramatically shown, the results predicted by the model closely follow the same pattern as the experimental values. In figure 16 (seed distribution), there is a small discrepancy between model prediction and experimental measurements. This disagreement can be explained by the following reason: for initial distribution of particles (or seed size distribution), the software is limited to “volume based distribution” which was measured by the particle size analyzer. To report the “number based distribution”, the software should calculate this value number by using volume based distribution values and as discussed before, this caused some numerical errors. It is worth pointing out that this numerical error could be part of the errors in CSD results of the following time intervals.

While the magnitudes of the crystal size distribution fractions do not match the experimental results in every case, the shape of the model-predicted distributions is very similar to the experimental results. Also, the position of the peak in each graph—which shows the common size of crystals at each time interval—is in good agreement with the experimental data. The magnitudes of number fractions in most of the bins in every time interval are in the range of 30-40% experimental error, which is a reasonable result. For most cases, the model over-predicts the size of the crystals for the following reason: in real life, such a process includes nucleation and barely aggregated crystals. The nucleation mechanism results in creating finer crystals in comparison with the existing grown crystals. Overlooking nucleation and aggregation mechanisms, and assuming that all the mass transfer resulting from only crystal growth leads to over prediction of “*growth/growth+nucleation+aggregation*” ratio in mass transfer; this would result in predicting larger crystal sizes.

Generally, the experimental data uncertainties and crystal size distribution measurement fluctuations became more significant as time passes. In other words, the CSD measurements at times 50 min and 60 min in different experiments show relatively higher degrees of deviation. One possible reason for these variations in experimental data, especially at time 50 min and 60 min could be due to the use of the laser scattering technique to measuring crystal size distribution in the dilute solution. In other words, as time passes and precipitation matures, the solution becomes more cloudless and the laser scattering particle size technique offers less certainty.

4.5 Average Crystal Size

Another aspect that the model reasonably predicts is average crystal size. Since struvite crystals are the product of this process, knowing the average size of the product at different time intervals is an important parameter to control the process and produce products with desirable size. Figure 24 shows the experimental and model predicted average crystal size.

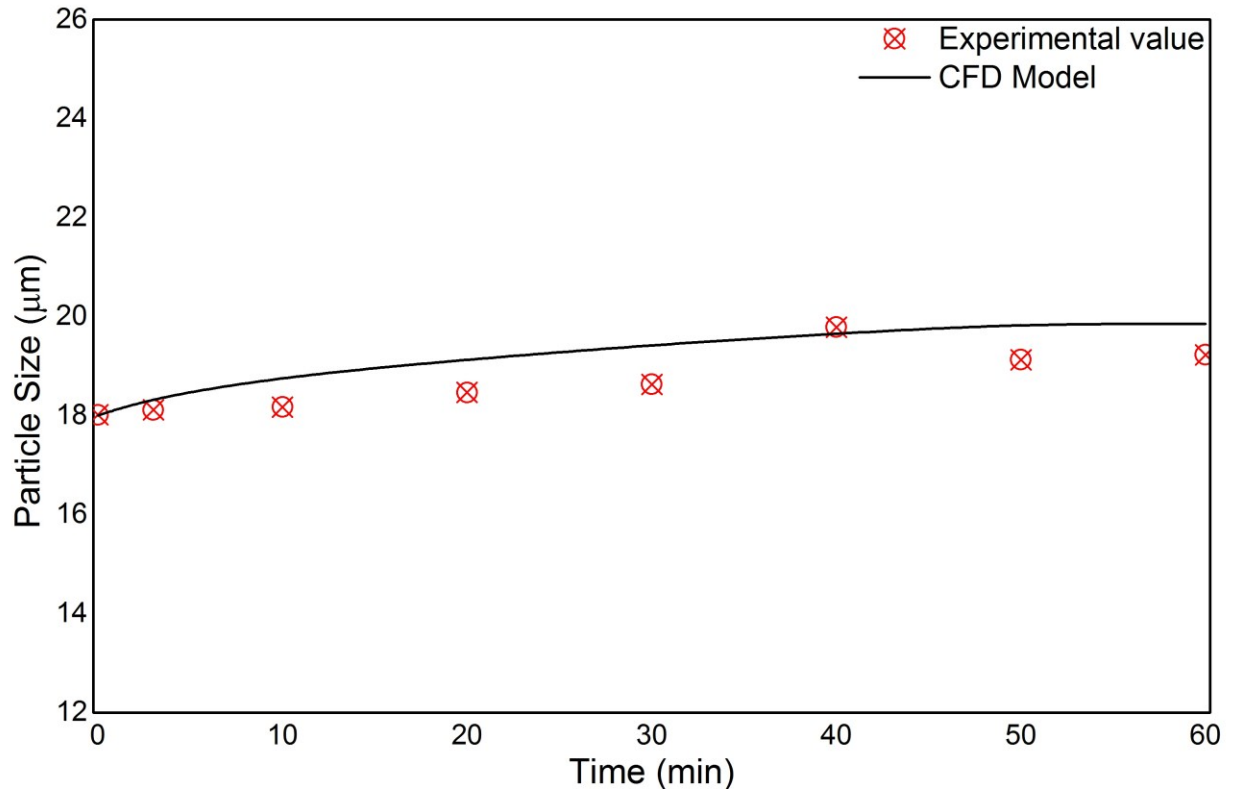


Figure 24 Experimental and CFD predicted crystal size results – number fraction weighted average size. Considering the range of experimental error, model prediction for average crystal size is in accordance with experimental results. Although average crystal size is over predicted in most cases, it follows the same pattern as real data and the highest error percentage, of about 10%, occurs at time 30 min.

5 CONCLUSIONS AND RECOMMENDATIONS FOR FUTURE WORKS

This work successfully fulfilled the research objectives, as defined in section 1.6, which are listed below:

- 1- The population balance equations were defined for the hydrodynamic model with the kinetic mechanism of crystal growth through the discretized population balance equation.
- 2- The presented model estimated the crystal size distribution of particles with an acceptable level of agreement with experimental measurements. Results showed just that while ignoring nucleation, aggregation, and breakage, and considering just the growth phenomena will affect the CSD prediction of the model and will cause over-prediction, the general trend and the position of peaks in CSD curves are in good agreement with the experimental measurements.

Additionally, some other conclusions were made while conducting this research are presented below:

A thermodynamic platform is presented which could calculate thermodynamic and chemical values such as species concentrations and pH value for a specific value of SI or vice versa.

Coupling the population balance model with CFD model with the same exact size groupings is an important feature of this work, which could minimize the distribution re-calculation errors. Also this model showed the possibility of applying all other precipitation mechanisms including nucleation rate, aggregation rate, and breakage kernel to the model simply by turning on the related options in the software, which can make this model a tool to test any suggested kinetics value for these mechanisms.

Finally, the following recommendations are made for future work:

- 1- Currently, the thermodynamic model was used separately from the CFD model and the outputs of the thermodynamic model were used as the inputs for the CFD model. It is recommended to connect the thermodynamic model to the CFD model through a UDF to run them simultaneously in order to make a dynamic interaction between the data from these models.

- 2- Future studies could improve the model by applying different suggested aggregation and nucleation rates to find the best model matched to actual data. It was desired to include different rates and different combinations of precipitation mechanisms and compare the results, however, due to time limitation, it should be considered for future works.

6 REFERENCES

1. Heffer, P., Prud'homme, M., *Fertilizer outlook 2014–2018*, in *82nd Annual Conference. International Fertilizer Industry Association*. 2014: Sydney, Australia.
2. Kataki, S., et al., *Phosphorus recovery as struvite: Recent concerns for use of seed, alternative Mg source, nitrogen conservation and fertilizer potential*. *Resources, Conservation and Recycling*, 2016. **107**: p. 142-156.
3. Zhou, Z., et al., *Effect of humic substances on phosphorus removal by struvite precipitation*. *Chemosphere*, 2015. **141**: p. 94-99.
4. Kim, B.U., et al., *Ammonium nitrogen removal from slurry-type swine wastewater by pretreatment using struvite crystallization for nitrogen control of anaerobic digestion*. *Water Science and Technology*, 2004. **49**(5-6): p. 215-222.
5. Ali, M.I. and P.A. Schneider, *A fed-batch design approach of struvite system in controlled supersaturation*. *Chemical Engineering Science*, 2006. **61**(12): p. 3951-3961.
6. Cho, J.-H., J.-E. Lee, and C.-S. Ra, *Microwave irradiation as a way to reutilize the recovered struvite slurry and to enhance system performance*. *Journal of Animal Science and Technology*, 2009. **51**(4): p. 337-342.
7. Le Corre, K.S., et al., *Struvite crystallisation and recovery using a stainless steel structure as a seed material*. *Water research*, 2007. **41**(11): p. 2449-2456.
8. Zhang, T., L. Ding, and H. Ren, *Pretreatment of ammonium removal from landfill leachate by chemical precipitation*. *Journal of Hazardous Materials*, 2009. **166**(2): p. 911-915.
9. Korchef, A., H. Saidou, and M.B. Amor, *Phosphate recovery through struvite precipitation by CO₂ removal: effect of magnesium, phosphate and ammonium concentrations*. *Journal of hazardous materials*, 2011. **186**(1): p. 602-613.
10. Merino-Jimenez, I., et al., *Enhanced MFC power production and struvite recovery by the addition of sea salts to urine*. *Water Research*, 2017. **109**: p. 46-53.
11. Moerman, W., et al., *Phosphate removal in agro-industry: Pilot- and full-scale operational considerations of struvite crystallization*. *Water Research*, 2009. **43**(7): p. 1887-1892.
12. Rahaman, M.S., D.S. Mavinic, and N. Ellis, *Fluidisation behaviour of struvite recovered from wastewater*. *Journal of Environmental Engineering and Science*, 2014. **9**(2): p. 137-149.
13. Johnston, A.E. and I.R. Richards, *Effectiveness of different precipitated phosphates as phosphorus sources for plants*. *Soil Use and Management*, 2003. **19**(1): p. 45-49.
14. Gaterell, M.R., et al., *An economic and environmental evaluation of the opportunities for substituting phosphorus recovered from wastewater treatment works in existing UK fertiliser markets*. *Environmental Technology*, 2000. **21**(9): p. 1067-1084.
15. Lee, J.E., M.M. Rahman, and C.S. Ra, *Dose effects of Mg and PO₄ sources on the composting of swine manure*. *Journal of hazardous materials*, 2009. **169**(1): p. 801-807.
16. Moussa, S.B., et al., *Electrochemical precipitation of struvite*. *Electrochemical and solid-state letters*, 2006. **9**(6): p. C97-C101.
17. Wang, C.C., et al., *Formation of pure struvite at neutral pH by electrochemical deposition*. *Chemical Engineering Journal*, 2010. **159**(1–3): p. 280-283.
18. Fischer, F., et al., *Microbial fuel cell enables phosphate recovery from digested sewage sludge as struvite*. *Bioresource Technology*, 2011. **102**(10): p. 5824-5830.
19. Cusick, R.D. and B.E. Logan, *Phosphate recovery as struvite within a single chamber microbial electrolysis cell*. *Bioresource Technology*, 2012. **107**: p. 110-115.
20. Liberti, L., et al., *The 10 m³ h⁻¹ rim-nut demonstration plant at West Bari for removing and recovering N and P from wastewater*. *Water Research*, 1986. **20**(6): p. 735-739.

21. Liberti, L., D. Petruzzelli, and L. De Florio, *REM NUT Ion Exchange Plus Struvite Precipitation Process*. Environmental Technology, 2001. **22**(11): p. 1313-1324.
22. Mijangos, F., et al., *Synthesis of struvite by ion exchange isothermal supersaturation technique*. Reactive and Functional Polymers, 2004. **60**: p. 151-161.
23. Petruzzelli, D., et al., *A phosphate-selective sorbent for the REM NUT® process: field experience at Massafra Wastewater Treatment Plant*. Reactive and Functional Polymers, 2004. **60**: p. 195-202.
24. Mijangos, F., et al., *Analysis of Ion Exchange Isothermal Supersaturation Process for Struvite Production*. Industrial & Engineering Chemistry Research, 2013. **52**(30): p. 10276-10283.
25. Ortueta, M., et al., *Ion Exchange Synthesis of Struvite Accompanied by Isothermal Supersaturation: Influence of Polymer Matrix and Functional Groups Type*. Solvent Extraction and Ion Exchange, 2015. **33**(1): p. 65-74.
26. González-Muñoz, M.T., et al., *Struvite and calcite crystallization induced by cellular membranes of Myxococcus xanthus*. Journal of Crystal Growth, 1996. **163**(4): p. 434-439.
27. Ben Omar, N., M.T. Gonzalez-Muñoz, and J.M.A. Peñalver, *Struvite crystallization on Myxococcus cells*. Chemosphere, 1998. **36**(3): p. 475-481.
28. Da Silva, S., et al., *Effect of culture conditions on the formation of struvite by Myxococcus xanthus*. Chemosphere, 2000. **40**(12): p. 1289-1296.
29. Jimenez-Lopez, C., et al., *Biom mineralization induced by Myxobacteria*. Communicating current research and educational topics and trends in applied microbiology, 2007. **1**: p. 143-154.
30. Tünay, O., et al., *Ammonia removal by magnesium ammonium phosphate precipitation in industrial wastewaters*. Water Science and Technology, 1997. **36**(2): p. 225-228.
31. Kabdasli, I., M. Gürel, and O. Tünay, *Characterization and Treatment of Textile Printing Wastewaters*. Environmental Technology, 2000. **21**(10): p. 1147-1155.
32. Chimenos, J.M., et al., *Removal of ammonium and phosphates from wastewater resulting from the process of cochineal extraction using MgO-containing by-product*. Water Research, 2003. **37**(7): p. 1601-1607.
33. Türker, M. and I. Çelen, *Removal of ammonia as struvite from anaerobic digester effluents and recycling of magnesium and phosphate*. Bioresource Technology, 2007. **98**(8): p. 1529-1534.
34. Ronteltap, M., M. Maurer, and W. Gujer, *Struvite precipitation thermodynamics in source-separated urine*. Water Research, 2007. **41**(5): p. 977-984.
35. Yu, R., et al., *Combination of struvite pyrolysate recycling with mixed-base technology for removing ammonium from fertilizer wastewater*. Bioresource Technology, 2012. **124**: p. 292-298.
36. Khai, N.M. and T.Q.T. Hoang, *Chemical Precipitation of Ammonia and Phosphate from Nam Son Landfill Leachate, Hanoi*. Iranica Journal of Energy & Environment, 2012. **3**: p. 32-36.
37. Xu, H., et al., *Recovery of phosphorus as struvite from sewage sludge ash*. Journal of Environmental Sciences, 2012. **24**(8): p. 1533-1538.
38. Foletto, E.L., et al., *Production of struvite from beverage waste as phosphorus source*. Materials Research, 2013. **16**: p. 242-245.
39. Wilsenach, J.A., C.A.H. Schuurbijs, and M.C.M. van Loosdrecht, *Phosphate and potassium recovery from source separated urine through struvite precipitation*. Water Research, 2007. **41**(2): p. 458-466.
40. Zhao, Q., et al., *Phosphorous recovery technology in conjunction with dairy anaerobic digestion*. CFF Final Report-AD Component, 2010.
41. Rahaman, M.S., et al., *Modeling phosphorus removal and recovery from anaerobic digester supernatant through struvite crystallization in a fluidized bed reactor*. Water Research, 2014. **51**: p. 1-10.

42. Guadie, A., et al., *Enhanced struvite recovery from wastewater using a novel cone-inserted fluidized bed reactor*. Journal of Environmental Sciences, 2014. **26**(4): p. 765-774.
43. Su, C.-C., et al., *Phosphate recovery from fluidized-bed wastewater by struvite crystallization technology*. Journal of the Taiwan Institute of Chemical Engineers, 2014. **45**(5): p. 2395-2402.
44. Ali, M.I. and P.A. Schneider, *An approach of estimating struvite growth kinetic incorporating thermodynamic and solution chemistry, kinetic and process description*. Chemical Engineering Science, 2008. **63**(13): p. 3514-3525.
45. Pastor, L., et al., *A pilot-scale study of struvite precipitation in a stirred tank reactor: Conditions influencing the process*. Bioresource Technology, 2008. **99**(14): p. 6285-6291.
46. Hanhoun, M., et al., *Simultaneous determination of nucleation and crystal growth kinetics of struvite using a thermodynamic modeling approach*. Chemical Engineering Journal, 2013. **215–216**: p. 903-912.
47. Kramer, H.J.M., et al., *Modeling of industrial crystallizers for control and design purposes*. Powder Technology, 2000. **108**(2–3): p. 185-191.
48. Rousseaux, J.M., et al., *CFD simulation of precipitation in the sliding-surface mixing device*. Chemical Engineering Science, 2001. **56**(4): p. 1677-1685.
49. Wang, Z., et al., *Computational Fluid Dynamics Approach to the Effect of Mixing and Draft Tube on the Precipitation of Barium Sulfate in a Continuous Stirred Tank1*. Chinese Journal of Chemical Engineering, 2006. **14**(6): p. 713-722.
50. Logashenko, D., et al., *Simulation of crystal growth and attrition in a stirred tank*. Computing and Visualization in Science, 2006. **9**(3): p. 175-183.
51. Sha, Z., et al., *Application of CFD simulation to suspension crystallization—factors affecting size-dependent classification*. Powder Technology, 2001. **121**(1): p. 20-25.
52. Zhu, Z. and H. Wei, *Flow field of stirred tank used in the crystallization process of ammonium sulphate*. Science Asia, 2008. **34**: p. 97-101.
53. Wantha, W. and A.E. Flood, *Numerical simulation and analysis of flow in a DTB crystallizer*. Chemical Engineering Communications, 2008. **195**(11): p. 1345-1370.
54. Plewik, R., et al., *Suspension flow in crystallizers with and without hydraulic classification*. Chemical Engineering Research and Design, 2010. **88**(9): p. 1194-1199.
55. Rahaman, M.S. and D.S. Mavinic, *Recovering nutrients from wastewater treatment plants through struvite crystallization: CFD modelling of the hydrodynamics of UBC MAP fluidized-bed crystallizer*. Water Science and Technology, 2009. **59**(10): p. 1887-1892.
56. Al-Rashed, M., et al., *Multiphase CFD modeling: Fluid dynamics aspects in scale-up of a fluidized-bed crystallizer*. Chemical Engineering and Processing: Process Intensification, 2013. **63**: p. 7-15.
57. Rane, C.V., et al., *CFD simulation and comparison of industrial crystallizers*. The Canadian Journal of Chemical Engineering, 2014. **92**(12): p. 2138-2156.
58. Ohlinger, K.N., T.M. Young, and E.D. Schroeder, *Predicting struvite formation in digestion*. Water Research, 1998. **32**(12): p. 3607-3614.
59. Bouropoulos, N.C. and P.G. Koutsoukos, *Spontaneous precipitation of struvite from aqueous solutions*. Journal of Crystal Growth, 2000. **213**(3): p. 381-388.
60. Harada, H., et al., *Predicting struvite formation for phosphorus recovery from human urine using an equilibrium model*. Water Science and Technology, 2006. **54**(8): p. 247-255.
61. Çelen, I., et al., *Using a chemical equilibrium model to predict amendments required to precipitate phosphorus as struvite in liquid swine manure*. Water Research, 2007. **41**(8): p. 1689-1696.
62. Rahaman, M.S., D.S. Mavinic, and N. Ellis, *Phosphorus recovery from anaerobic digester supernatant by struvite crystallization: model-based evaluation of a fluidized bed reactor*. Water Science and Technology, 2008. **58**(6): p. 1321-1327.

63. Gadekar, S. and P. Pullammanappallil, *Validation and applications of a chemical equilibrium model for struvite precipitation*. Environmental modeling & assessment, 2010. **15**(3): p. 201-209.
64. Hanhoun, M., et al., *Temperature impact assessment on struvite solubility product: a thermodynamic modeling approach*. Chemical engineering journal, 2011. **167**(1): p. 50-58.
65. Lee, S.-H., et al., *Development and validation of an equilibrium model for struvite formation with calcium co-precipitation*. Journal of Crystal Growth, 2013. **372**: p. 129-137.
66. Lee, S.-h., R. Kumar, and B.-H. Jeon, *Struvite precipitation under changing ionic conditions in synthetic wastewater: Experiment and modeling*. Journal of colloid and interface science, 2016. **474**: p. 93-102.
67. Barnes, N.J. and A.R. Bowers, *A probabilistic approach to modeling struvite precipitation with uncertain equilibrium parameters*. Chemical Engineering Science, 2017. **161**: p. 178-186.
68. Nelson, N.O., R.L. Mikkelsen, and D.L. Hesterberg, *Struvite precipitation in anaerobic swine lagoon liquid: effect of pH and Mg: P ratio and determination of rate constant*. Bioresource Technology, 2003. **89**(3): p. 229-236.
69. Quintana, M., et al., *Kinetics of phosphorus removal and struvite formation by the utilization of by-product of magnesium oxide production*. Chemical Engineering Journal, 2005. **111**(1): p. 45-52.
70. Le Corre, K.S., et al., *Kinetics of struvite precipitation: effect of the magnesium dose on induction times and precipitation rates*. Environmental technology, 2007. **28**(12): p. 1317-1324.
71. Quintana, M., et al., *Removal of phosphorus through struvite precipitation using a by-product of magnesium oxide production (BMP): Effect of the mode of BMP preparation*. Chemical Engineering Journal, 2008. **136**(2): p. 204-209.
72. Rahaman, M.S., N. Ellis, and D.S. Mavinic, *Effects of various process parameters on struvite precipitation kinetics and subsequent determination of rate constants*. Water Science and Technology, 2008. **57**(5): p. 647.
73. Ariyanto, E., T.K. Sen, and H.M. Ang, *The influence of various physico-chemical process parameters on kinetics and growth mechanism of struvite crystallisation*. Advanced Powder Technology, 2014. **25**(2): p. 682-694.
74. Capdevielle, A., et al., *Kinetics of struvite precipitation in synthetic biologically treated swine wastewaters*. Environmental Technology, 2014. **35**(10): p. 1250-1262.
75. Chong, N.-M. and Q.-M. Thai, *Optimization and kinetics of nutrient removal from wastewater by chemical precipitation of struvite*. Desalination and Water Treatment, 2015. **54**(12): p. 3422-3431.
76. Bhuiyan, M.I.H., D.S. Mavinic, and R.D. Beckie, *Nucleation and growth kinetics of struvite in a fluidized bed reactor*. Journal of Crystal Growth, 2008. **310**(6): p. 1187-1194.
77. Harrison, M.L., et al., *Growth rate kinetics for struvite crystallization*. Chem. Eng. Trans, 2011. **25**: p. 309-314.
78. Triger, A., J.-S. Pic, and C. Cabassud, *Determination of struvite crystallization mechanisms in urine using turbidity measurement*. Water Research, 2012. **46**(18): p. 6084-6094.
79. Mehta, C.M. and D.J. Batstone, *Nucleation and growth kinetics of struvite crystallization*. Water research, 2013. **47**(8): p. 2890-2900.
80. Galbraith, S.C., P.A. Schneider, and A.E. Flood, *Model-driven experimental evaluation of struvite nucleation, growth and aggregation kinetics*. Water Research, 2014. **56**: p. 122-132.
81. Crutchik, D. and J.M. Garrido, *Kinetics of the reversible reaction of struvite crystallisation*. Chemosphere, 2016. **154**: p. 567-572.
82. Childs, C.W., *Potentiometric study of equilibria in aqueous divalent metal orthophosphate solutions*. Inorganic Chemistry, 1970. **9**(11): p. 2465-2469.
83. François M. M. Morel, J.G.H., *Principles and Applications of Aquatic Chemistry*. 1993.

84. Taylor, A.W., A.W. Frazier, and E.L. Gurney, *Solubility products of magnesium ammonium and magnesium potassium phosphates*. Transactions of the Faraday Society, 1963. **59**(0): p. 1580-1584.
85. AE Martell, R.S., *Critical stability constants*. 1974.
86. Snoeyink, V.L., Jenkins, D., *Water Chemistry*. 1980, USA: Wiley.
87. Mullin, J.W., *Crystallization (3rd edn)*. 1993, Butterworth-Heinemann: Oxford, England.
88. Jones, A.G., *Crystallization Process Systems*. 2002, Boston: Butterworth-Heinemann, Oxford.
89. Le Corre, K.S., et al., *Impact of calcium on struvite crystal size, shape and purity*. Journal of Crystal Growth, 2005. **283**(3–4): p. 514-522.
90. Koralewska, J., et al., *Reaction-Crystallization of Struvite in a Continuous Liquid Jet-Pump DTM MSMR Crystallizer with Upward Circulation of Suspension in a Mixing Chamber – an SDG Kinetic Approach*. Chemical Engineering & Technology, 2007. **30**(11): p. 1576-1583.
91. Koralewska, J., et al., *Kinetics of Reaction-Crystallization of Struvite in the Continuous Draft Tube Magma Type Crystallizers—Influence of Different Internal Hydrodynamics*. Chinese Journal of Chemical Engineering, 2009. **17**(2): p. 330-339.
92. Ronteltap, M., et al., *Struvite precipitation from urine – Influencing factors on particle size*. Water Research, 2010. **44**(6): p. 2038-2046.
93. Rane, C.V., et al., *Effect of impeller design and power consumption on crystal size distribution*. AIChE Journal, 2014. **60**(10): p. 3596-3613.
94. Joshi, J.B. and V.V. Ranade, *Computational Fluid Dynamics for Designing Process Equipment: Expectations, Current Status, and Path Forward*. Industrial & Engineering Chemistry Research, 2003. **42**(6): p. 1115-1128.
95. Ramkrishna, D., *Population Balances: Theory and Applications to Particulate Systems in Engineering*. 2000, San Diego, CA: Academic Press.
96. Le Corre, K.S., et al., *Agglomeration of struvite crystals*. Water Research, 2007. **41**(2): p. 419-425.
97. Hounslow, M.J., et al., *A micro-mechanical model for the rate of aggregation during precipitation from solution*. Chemical Engineering Science, 2001. **56**(7): p. 2543-2552.
98. Hounslow, M.J., R.L. Ryall, and V.R. Marshall, *A discretized population balance for nucleation, growth, and aggregation*. AIChE Journal, 1988. **34**(11): p. 1821-1832.
99. Lister, J.D., D.J. Smit, and M.J. Hounslow, *Adjustable discretized population balance for growth and aggregation*. AIChE Journal, 1995. **41**(3): p. 591-603.
100. Brucato, A., et al., *Numerical prediction of flow fields in baffled stirred vessels: A comparison of alternative modelling approaches*. Chemical Engineering Science, 1998. **53**(21): p. 3653-3684.
101. Bartels, C., et al., *Computational fluid dynamics applications on parallel-vector computers: computations of stirred vessel flows*. Computers & Fluids, 2002. **31**(1): p. 69-97.
102. Deglon, D.A. and C.J. Meyer, *CFD modelling of stirred tanks: Numerical considerations*. Minerals Engineering, 2006. **19**(10): p. 1059-1068.
103. Rushton, J.H., Costich, E.W., Everett, H.J., *Power characteristics of mixing impellers -Part II*. Chemical Engineering Progress, 1950. **46**: p. 467-476.
104. Zalc, J.M., et al., *Extensive validation of computed laminar flow in a stirred tank with three Rushton turbines*. AIChE Journal, 2001. **47**(10): p. 2144-2154.
105. Costes, J. and J.P. Couderc, *Study by laser Doppler anemometry of the turbulent flow induced by a Rushton turbine in a stirred tank: Influence of the size of the units—I. Mean flow and turbulence*. Chemical Engineering Science, 1988. **43**(10): p. 2751-2764.
106. Wadnerkar, D., et al., *CFD simulation of solid–liquid stirred tanks for low to dense solid loading systems*. Particuology, 2016. **29**: p. 16-33.

Appendices

I. Numerical details

Table A1 Summary of simulation settings (Model parameters)

			Note/Unit	
Geometry	Shape	Cylinder		
	Volume	1		liter
	Size	Height	90	mm
		Diameter	124	mm
	Baffle	4		equal distance
Impeller	6	blades	Rushton blade	
Mesh	Mesh method	Tetrahedrons		
	Horizontal Cell growth	-		
	Elements	220000		
	Nodes	42000		
	Faces	450000		
General Setup	Time	Transient		
	Solver	Pressure-based		
Boundary Conditions	Outlet boundary condition	pressure outlet		
	Wall boundary condition	No slip		
	Gravitational acceleration	9.81		m/s ²
	Operation pressure	1.013*10 ⁵		pa
	Impeller speed	100		rpm
Model equations	Viscose Model	RNG k-e		
	Near wall treatment	standard wall functions		
	Multiphase model	Eulerian		2 phases
	Population balance model	Discrete		
Solution method	pressure-velocity coupling	SIMPLE		
	Spatial discretization	First order upwind		
Under relaxation factors	momentum	0.7		
	pressure	0.3		
Calculation setup	Convergence criteria	0.001		
	Max iteration/Time step	20		

II. Loading the Population Balance Module in Fluent

For using this module, it should be loaded into the model task page. This could be done through the text user interface (TUI). The text command for loading the population balance module is:

```
>/define/models/addon-module
```

Then the below list of ANSYS Fluent add-on modules will appear:

0. None
1. MHD Model
2. Fiber Model
3. Fuel Cell and Electrolysis Model
4. SOFC Model with Unresolved Electrolyte
5. Population Balance Model
6. Adjoint Solver
7. Single-Potential Battery Model
8. Dual-Potential MSMD Battery Model

Enter Module Number: [0]

By entering the module number, which is 5 for population balance model, this module will be activated.

III. Growth rate User Defined Function

```
#include "udf.h"
#include "sg_pb.h"
#include "sg_mphase.h"

DEFINE_PB_GROWTH_RATE(growth_rate, cell, thread, d_1)
{
    real G, SI;
    real Ng = 1.66; /*growth power*/
    real Kg = 1.307e-8; /*growth coefficient*/
    real Ksp = 5.49e-14; /*solubility product of struvite*/

    real gama_mg, m_mg, gama_nh4, m_nh4, gama_po4, m_po4;
    real mw_mg, mw_nh4, mw_po4, z_mg, z_nh4, z_po4, I, temp_gama_mg,
    temp_gama_nh4, temp_gama_po4;
    real A = 0.509; /*@ 25 C*/

    Thread *tc = THREAD_SUPER_THREAD(thread); /*primary phase thread*/
    Thread **pt = THREAD_SUB_THREADS(tc);
    Thread *tp = pt [P_PHASE];

    mw_mg = 24.305; /*molecular weight*/
    mw_nh4 = 18.038; /*molecular weight*/
    mw_po4 = 94.971; /*molecular weight*/
    z_nh4 = 1; /*nh4 ion electrical charge*/
    z_mg = 2; /*mg ion electrical charge*/
    z_po4 = 3; /*po4 ion electrical charge*/

    m_po4 = C_YI(cell, liq, 5)*999.4211 / mw_po4;
    m_nh4 = C_YI(cell, liq, 6)*999.4211 / mw_nh4;
    m_mg = C_YI(cell, liq, 7)*999.211 / mw_mg;

    I = 0.5*(m_mg*pow(z_mg, 2) + m_nh4*pow(z_nh4, 2) + m_po4*pow(z_po4, 2));

    temp_gama_mg = -(A*pow(z_mg, 2)*(pow(I, .5) / (1 + pow(I, .5)))) - .3*I);
    temp_gama_nh4 = -(A*pow(z_nh4, 2)*(pow(I, .5) / (1 + pow(I, .5)))) -
    .3*I);
    temp_gama_po4 = -(A*pow(z_po4, 2)*(pow(I, .5) / (1 + pow(I, .5)))) -
    .3*I);

    gama_mg = pow(10, temp_gama_mg);
    gama_nh4 = pow(10, temp_gama_nh4);
    gama_po4 = pow(10, temp_gama_po4);
}
```

```
SI = log10(gama_mg*m_mg* gama_nh4* m_nh4* gama_po4* m_po4/Ksp);
```

```
if (SI <= 1e-99.)  
{  
    G = 0.;  
}  
else  
{  
    G = Kg*pow(SI, Ng);  
}  
return G;  
}
```

IV. Thermodynamic model

Input						
Total Mg	121.52 mg/L Mg		Reset Variables			
Total N	70.033 mg/L N		Go to Variables			
Total P	154.86 mg/L P					
Conductivity (µS/cm)	2050 Cond					
Activity Coeff Method (0 = none, 1 = Debye, 2 = Guntel.)	1 Debye-Huckel: Ionic Strength < 0.005					
Ionic Strength Method (1 = Calculated, 2 = Conductivity)	1 Calculated from ions present					
Temperature	25 Celcius	New				
Output						
Ionic Strength (µ)	0.0136					
pH	8.000	Set SSR and Solve for pH				
[Mg ²⁺][NH ₄ ⁺][PO ₄ ³⁻] x Activity coefficients	4.78E-13					
SSR	8.70	Set pH and Solve for SSR	SI	0.93975		
pPs	11.49					
Solver Solution Indicator	Solved					
Constants						
Atomic Weights (g/mol)						
Hydrogen (AWH)	1.00794					
Oxygen (AWO)	15.9994					
Phosphorus (AWP)	30.97376					
Nitrogen (AWN)	14.0067					
Magnesium (AWMg)	24.305					
Stability Constants (pK values)						
MgNH ₄ PO ₄ ·6H ₂ O <> Mg ²⁺ + NH ₄ ⁺ + PO ₄ ³⁻ + 6H ₂ O	13.260	pKSO	from Ohlinger Ph.D. 1999			
MgOH ⁺ <> Mg ²⁺ + OH ⁻	2.560	pKMgOH	from Ohlinger, ref. Morel and Hering 1993			
NH ₄ ⁺ <> H ⁺ + NH ₃	9.300	pKN	from Snoeyink and Jenkins 1980			
H ₂ PO ₄ ⁻ <> H ⁺ + HPO ₄ ²⁻	2.150	pKP1	from Ohlinger, ref. Martell and Smith 1989			
H ₂ PO ₄ ⁻ <> H ⁺ + HPO ₄ ²⁻	7.200	pKP2	from Ohlinger, ref. Martell and Smith 1989			
HPO ₄ ²⁻ <> H ⁺ + PO ₄ ³⁻	12.350	pKP3	from Ohlinger, ref. Martell and Smith 1989			
MgH ₂ PO ₄ ⁺ <> Mg ²⁺ + H ₂ PO ₄ ⁻	0.450	pKMg1	from Ohlinger, ref. Morel and Hering 1993			
MgHPO ₄ ⁻ <> Mg ²⁺ + HPO ₄ ²⁻	2.910	pKMg2	from Ohlinger, ref. Taylor et al. 1963b			
MgPO ₄ ⁻ <> Mg ²⁺ + PO ₄ ³⁻	4.800	pKMg3	from Ohlinger, ref. Childs 1970			
H ₂ O <> H ⁺ + OH ⁻	14.000	pKwater				
Debye-Huckel Parameters						
A	0.5085					
B	32810000					
Ionic Strength Factor	0.000016					
Variables		Guesses for Reset			Guesses for Reset	
Go to Top of Page						
Guessed Ionic Strength	0.014					0.05
Species						
	-log{ }	[] mol/L	MW (g/mol)	Chg (Z)	Δμ	γ _i
Mg ²⁺	2.774	2.91E-03	24.31	2	5.81E-03	0.579
NH ₄ ⁺	2.379	4.79E-03	18.04	1	2.40E-03	0.872
PO ₄ ³⁻	7.167	2.33E-07	94.97	-3	1.05E-06	0.292
H ⁺	8.000	1.15E-08	1.01	1	5.73E-09	0.872
Calculations						
	-log{ }	[] mol/L	MW (g/mol)	Chg (Z)	Δμ	γ _i
MgOH ⁺	6.214	7.00E-07	41.31	1	3.50E-07	0.872
OH ⁻	6.000	1.15E-06	17.01	-1	5.73E-07	0.872
NH ₃	3.679	2.09E-04	17.03	0	0.00E+00	1.000
HPO ₄ ²⁻	2.817	2.63E-03	95.98	-2	5.26E-03	0.579
H ₂ PO ₄ ⁻	3.617	2.77E-04	96.99	-1	1.38E-04	0.872
H ₃ PO ₄	9.467	3.41E-10	98.00	0	0.00E+00	1.000
MgPO ₄ ⁻	5.141	8.28E-06	119.28	-1	4.14E-06	0.872
MgHPO ₄	2.681	2.08E-03	120.28	0	0.00E+00	1.000
MgH ₂ PO ₄ ⁺	5.941	1.31E-06	121.29	1	6.56E-07	0.872
Concentrations						
	[] mol/L	[] mg/L				
Total Mg	5.00E-03	122				
Total N	5.00E-03	70				
Total P	5.00E-03	155				
Safety Ionic Strength (avoids #NUM! errors)	0.014					
Constraints						
Go to Top of Page						
Guessed Ionic Strength	0.00000	Guessed right				
Total Mg	0.00000	OK				
Total N	0.00000	OK				
Total P	0.00000	OK				

Figure A7 Schematic view of the Spreadsheet Thermodynamic Model

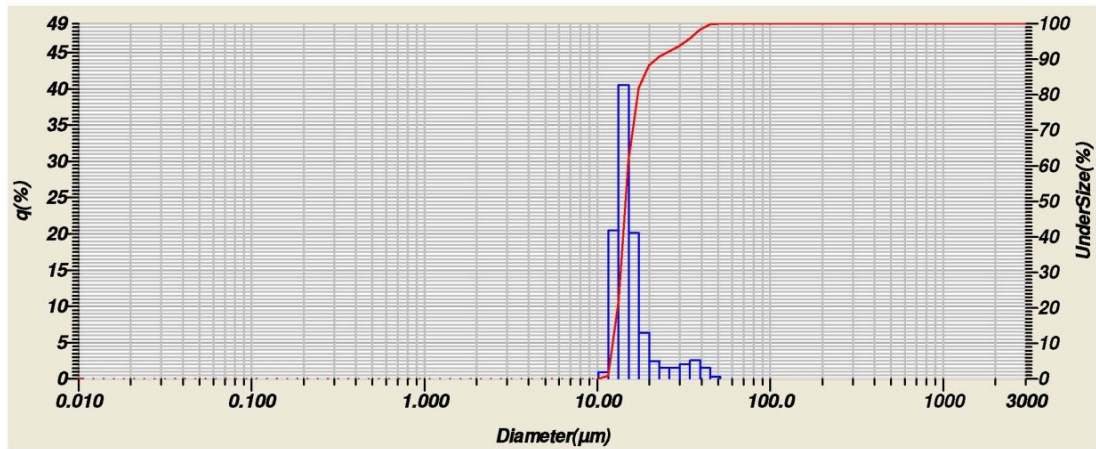
V. Raw experimental crystal size distributions data

2017.02.03 11:34:18

HORIBA Laser Scattering Particle Size Distribution Analyzer LA-950

Sample Name	: Crystal Struvite	Median Size	: 14.58104(μm)
ID#	: 201607181215121	Mean Size	: 16.43722(μm)
Data Name	: 201607181215121	Std.Dev.	: 6.0891(μm)
Transmittance(R)	: 86.4(%)	Geo.Mean Size	: 15.7047(μm)
Transmittance(B)	: 90.4(%)	Geo.Std.Dev.	: 1.3158(μm)
Circulation Speed	: 5	Mode Size	: 14.1672(μm)
Agitation Speed	: 3	Span	: OFF
Ultra Sonic	: OFF	Diameter on Cumulative %	: (2)10.00 (%) - 12.2868(μm)
Form of Distribution	: Manual		: (4)30.00 (%) - 13.6359(μm)
Distribution Base	: Number		: (6)60.00 (%) - 15.0779(μm)
Refractive Index (R)	: Crystal struvite Crystal struvite(1.500 - 0.000i),Water(1.333)		: (9)90.00 (%) - 21.9394(μm)
Refractive Index (B)	: Crystal struvite Crystal struvite(1.500 - 0.000i),Water(1.333)		
Material	: Mg NH4 PO4		
Source	: fertilizer		
Sample Number	: 1		
Test or Assay. Number	: 1		

Diameter (μm)	ASTM Mesh	Frequency %	Cumulative %
20.000	635	3.365	88.344
25.000	500	2.994	91.710
32.000	450	2.951	94.703
38.000	400	2.104	97.654
45.000	325	0.241	99.759
53.000	270	0.000	100.000
63.000	230	0.000	100.000
75.000	200	0.000	100.000
90.000	170	0.000	100.000
106.000	140	0.000	100.000
125.000	120	0.000	100.000
150.000	100	0.000	100.000
180.000	80	0.000	100.000
212.000	70	0.000	100.000
250.000	60	0.000	100.000
300.000	50	0.000	100.000
355.000	45	0.000	100.000
425.000	40	0.000	100.000
500.000	35	0.000	100.000
600.000	30	0.000	100.000
710.000	25	0.000	100.000
850.000	20	0.000	100.000
1000.000	18	0.000	100.000
1180.000	16	0.000	100.000
1400.000	14	0.000	100.000
1700.000	12	0.000	100.000
2000.000	10	0.000	100.000
2360.000	8	0.000	100.000
2800.000	7	0.000	100.000
3350.000	6	0.000	100.000
4000.000	5	0.000	100.000



1 / 1

Figure A8 Particle Size Distribution- Seed crystals(Time = 0)

HORIBA Laser Scattering Particle Size Distribution Analyzer LA-950

Sample Name	: Crystal Struvite	Median Size	: 15.36288(μm)
ID#	: 201608160938176	Mean Size	: 17.04076(μm)
Data Name	: 201608160938176	Std.Dev.	: 5.5140(μm)
Transmittance(R)	: 98.2(%)	Geo.Mean Size	: 16.4189(μm)
Transmittance(B)	: 98.9(%)	Geo.Std.Dev.	: 1.2870(μm)
Circulation Speed	: 5	Mode Size	: 14.6271(μm)
Agitation Speed	: 3	Span	: OFF
Ultra Sonic	: OFF	Diameter on Cumulative %	: (2)10.00 (%) - 13.1627(μm)
Form of Distribution	: Manual		: (4)30.00 (%) - 14.2298(μm)
Distribution Base	: Number		: (6)60.00 (%) - 16.1390(μm)
Refractive Index (R)	: Crystal struvite[Crystal struvite(1.500 - 0.000i),Water(1.333)]		: (9)90.00 (%) - 22.7169(μm)
Refractive Index (B)	: Crystal struvite[Crystal struvite(1.500 - 0.000i),Water(1.333)]		
Material	: Mg NH4 PO4		
Source	: fertilizer		
Sample Number	: 1		
Test or Assay. Number	: 1		

Diameter (μm)	ASTM Mesh	Frequency %	Cumulative %
20.000	635	3.365	88.344
25.000	500	2.994	91.710
32.000	450	2.951	94.703
38.000	400	2.104	97.654
45.000	325	0.241	99.759
53.000	270	0.000	100.000
63.000	230	0.000	100.000
75.000	200	0.000	100.000
90.000	170	0.000	100.000
106.000	140	0.000	100.000
125.000	120	0.000	100.000
150.000	100	0.000	100.000
180.000	80	0.000	100.000
212.000	70	0.000	100.000
250.000	60	0.000	100.000
300.000	50	0.000	100.000
355.000	45	0.000	100.000
425.000	40	0.000	100.000
500.000	35	0.000	100.000
600.000	30	0.000	100.000
710.000	25	0.000	100.000
850.000	20	0.000	100.000
1000.000	18	0.000	100.000
1180.000	16	0.000	100.000
1400.000	14	0.000	100.000
1700.000	12	0.000	100.000
2000.000	10	0.000	100.000
2360.000	8	0.000	100.000
2800.000	7	0.000	100.000
3350.000	6	0.000	100.000
4000.000	5	0.000	100.000

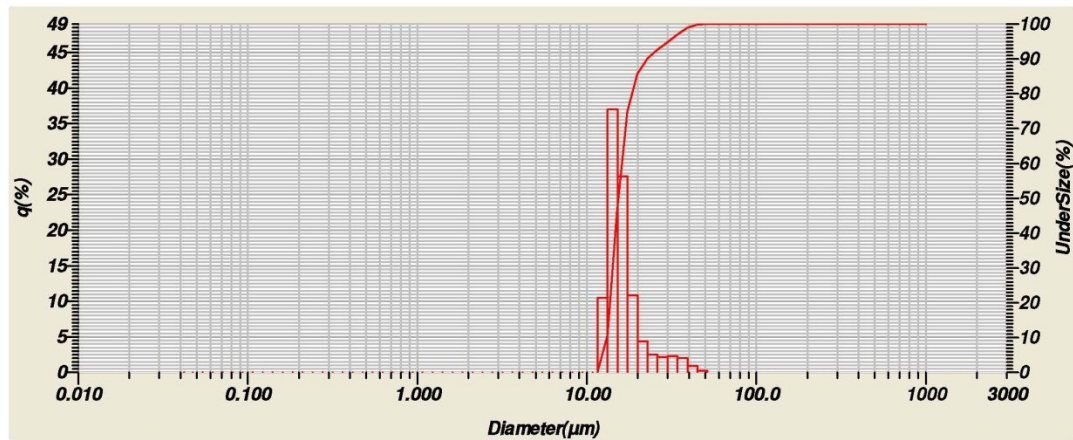


Figure A9 Particle Size Distribution – Time = 3min

HORIBA Laser Scattering Particle Size Distribution Analyzer LA-950

Sample Name	: Crystal Struvite	Median Size	: 14.7855(μm)
ID#	: 201608160946177	Mean Size	: 17.95650(μm)
Data Name	: 201608160946177	Std.Dev.	: 6.8098(μm)
Transmittance(R)	: 98.3(%)	Geo.Mean Size	: 16.0976(μm)
Transmittance(B)	: 99.0(%)	Geo.Std.Dev.	: 1.3388(μm)
Circulation Speed	: 5	Mode Size	: 15.2551(μm)
Agitation Speed	: 3	Span	: OFF
Ultra Sonic	: OFF	Diameter on Cumulative %	: (2)10.00 (%) - 12.4072(μm)
Form of Distribution	: Manual		: (4)30.00 (%) - 13.7835(μm)
Distribution Base	: Number		: (6)60.00 (%) - 15.4322(μm)
Refractive Index (R)	: Crystal struvite[Crystal struvite(1.500 - 0.000i),Water(1.333)]		: (9)90.00 (%) - 24.0490(μm)
Refractive Index (B)	: Crystal struvite[Crystal struvite(1.500 - 0.000i),Water(1.333)]		
Material	: Mg NH4 PO4		
Source	: fertilizer		
Sample Number	: 1		
Test or Assay. Number	: 1		

Diameter (μm)	ASTM Mesh	Frequency %	Cumulative %
20.000	635	4.565	86.048
25.000	500	3.835	90.613
32.000	450	2.622	94.448
38.000	400	1.805	97.070
45.000	325	0.773	98.875
53.000	270	0.296	99.648
63.000	230	0.056	99.944
75.000	200	0.000	100.000
90.000	170	0.000	100.000
106.000	140	0.000	100.000
125.000	120	0.000	100.000
150.000	100	0.000	100.000
180.000	80	0.000	100.000
212.000	70	0.000	100.000
250.000	60	0.000	100.000
300.000	50	0.000	100.000
355.000	45	0.000	100.000
425.000	40	0.000	100.000
500.000	35	0.000	100.000
600.000	30	0.000	100.000
710.000	25	0.000	100.000
850.000	20	0.000	100.000
1000.000	18	0.000	100.000
1180.000	16	0.000	100.000
1400.000	14	0.000	100.000
1700.000	12	0.000	100.000
2000.000	10	0.000	100.000
2360.000	8	0.000	100.000
2800.000	7	0.000	100.000
3350.000	6	0.000	100.000
4000.000	5	0.000	100.000

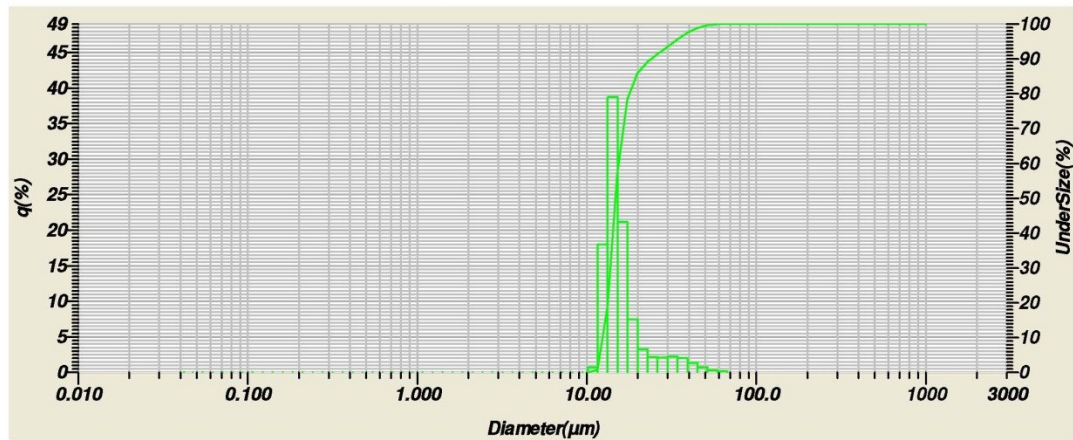


Figure A10 Particle Size Distribution – Time = 10min

HORIBA Laser Scattering Particle Size Distribution Analyzer LA-950

Sample Name	: Crystal Struvite	Median Size	: 12.29814(μm)
ID#	: 201608161727183	Mean Size	: 15.46132(μm)
Data Name	: 201608161727183	Std.Dev.	: 6.9214(μm)
Transmittance(R)	: 99.2(%)	Geo.Mean Size	: 12.7939(μm)
Transmittance(B)	: 99.4(%)	Geo.Std.Dev.	: 1.2943(μm)
Circulation Speed	: 5	Mode Size	: 15.2001(μm)
Agitation Speed	: 3	Span	: OFF
Ultra Sonic	: OFF	Diameter on Cumulative %	: (2)10.00 (%) - 10.4891(μm)
Form of Distribution	: Manual		: (4)30.00 (%) - 11.5732(μm)
Distribution Base	: Number		: (6)60.00 (%) - 12.6775(μm)
Refractive Index (R)	: Crystal struvite[Crystal struvite(1.500 - 0.000i),Water(1.333)]		: (9)90.00 (%) - 14.8952(μm)
Refractive Index (B)	: Crystal struvite[Crystal struvite(1.500 - 0.000i),Water(1.333)]		
Material	: Mg NH4 PO4		
Source	: fertilizer		
Sample Number	: 1		
Test or Assay. Number	: 1		

Diameter (μm)	ASTM Mesh	Frequency %	Cumulative %
20.000	635	0.425	96.796
25.000	500	0.503	97.221
32.000	450	0.429	97.724
38.000	400	0.391	98.153
45.000	325	0.365	98.544
53.000	270	0.402	98.909
63.000	230	0.401	99.311
75.000	200	0.288	99.712
90.000	170	0.000	100.000
106.000	140	0.000	100.000
125.000	120	0.000	100.000
150.000	100	0.000	100.000
180.000	80	0.000	100.000
212.000	70	0.000	100.000
250.000	60	0.000	100.000
300.000	50	0.000	100.000
355.000	45	0.000	100.000
425.000	40	0.000	100.000
500.000	35	0.000	100.000
600.000	30	0.000	100.000
710.000	25	0.000	100.000
850.000	20	0.000	100.000
1000.000	18	0.000	100.000
1180.000	16	0.000	100.000
1400.000	14	0.000	100.000
1700.000	12	0.000	100.000
2000.000	10	0.000	100.000
2360.000	8	0.000	100.000
2800.000	7	0.000	100.000
3350.000	6	0.000	100.000
4000.000	5	0.000	100.000

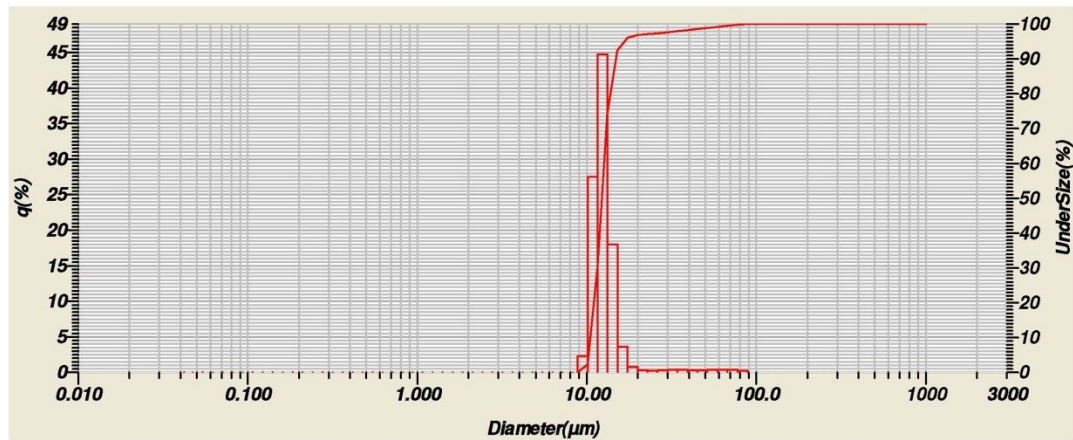


Figure A11 Particle Size Distribution – Time = 20min

HORIBA Laser Scattering Particle Size Distribution Analyzer LA-950

Sample Name	: Crystal Struvite	Median Size	: 14.33714(μm)
ID#	: 201608161005178	Mean Size	: 17.80092(μm)
Data Name	: 201608161005178	Std.Dev.	: 8.0603(μm)
Transmittance(R)	: 98.2(%)	Geo.Mean Size	: 15.7211(μm)
Transmittance(B)	: 98.9(%)	Geo.Std.Dev.	: 1.3770(μm)
Circulation Speed	: 5	Mode Size	: 15.0254(μm)
Agitation Speed	: 3	Span	: OFF
Ultra Sonic	: OFF	Diameter on Cumulative %	: (2)10.00 (%) - 12.2619(μm)
Form of Distribution	: Manual		: (4)30.00 (%) - 13.5150(μm)
Distribution Base	: Number		: (6)60.00 (%) - 14.7667(μm)
Refractive Index (R)	: Crystal struvite[Crystal struvite(1.500 - 0.000i),Water(1.333)]		: (9)90.00 (%) - 24.2657(μm)
Refractive Index (B)	: Crystal struvite[Crystal struvite(1.500 - 0.000i),Water(1.333)]		
Material	: Mg NH4 PO4		
Source	: fertilizer		
Sample Number	: 1		
Test or Assay. Number	: 1		

Diameter (μm)	ASTM Mesh	Frequency %	Cumulative %
20.000	635	1.708	88.488
25.000	500	2.519	90.196
32.000	450	2.752	92.715
38.000	400	2.388	95.467
45.000	325	1.284	97.856
53.000	270	0.613	99.140
63.000	230	0.223	99.753
75.000	200	0.024	99.976
90.000	170	0.000	100.000
106.000	140	0.000	100.000
125.000	120	0.000	100.000
150.000	100	0.000	100.000
180.000	80	0.000	100.000
212.000	70	0.000	100.000
250.000	60	0.000	100.000
300.000	50	0.000	100.000
355.000	45	0.000	100.000
425.000	40	0.000	100.000
500.000	35	0.000	100.000
600.000	30	0.000	100.000
710.000	25	0.000	100.000
850.000	20	0.000	100.000
1000.000	18	0.000	100.000
1180.000	16	0.000	100.000
1400.000	14	0.000	100.000
1700.000	12	0.000	100.000
2000.000	10	0.000	100.000
2360.000	8	0.000	100.000
2800.000	7	0.000	100.000
3350.000	6	0.000	100.000
4000.000	5	0.000	100.000

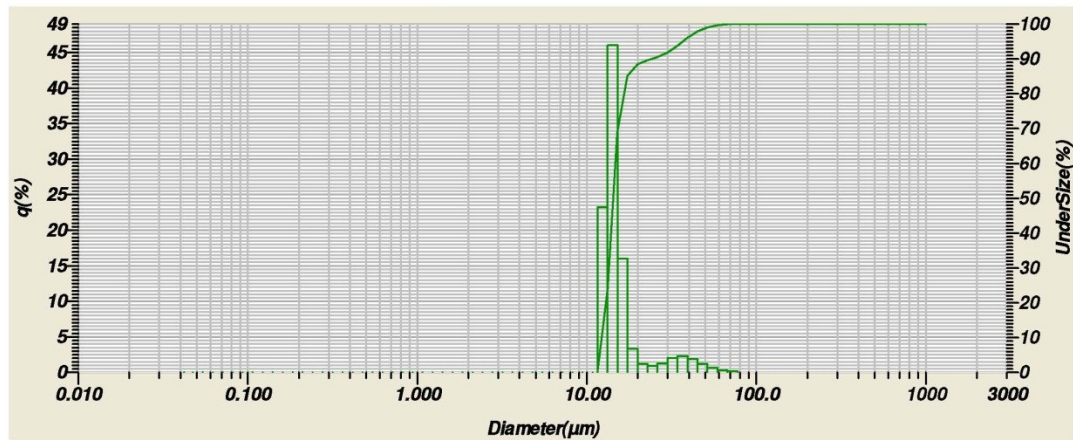


Figure A12 Particle Size Distribution – Time = 30min

HORIBA Laser Scattering Particle Size Distribution Analyzer LA-950

Sample Name	: Crystal Struvite	Median Size	: 14.34266(μm)
ID#	: 201611241255300	Mean Size	: 19.62482(μm)
Data Name	: 201611241255300	Std.Dev.	: 7.9443(μm)
Transmittance(R)	: 97.5(%)	Geo.Mean Size	: 15.6035(μm)
Transmittance(B)	: 98.4(%)	Geo.Std.Dev.	: 1.3636(μm)
Circulation Speed	: 5	Mode Size	: 16.0426(μm)
Agitation Speed	: 3	Span	: OFF
Ultra Sonic	: OFF	Diameter on Cumulative %	: (2)10.00 (%) - 12.2599(μm)
Form of Distribution	: Manual		: (4)30.00 (%) - 13.5144(μm)
Distribution Base	: Number		: (6)60.00 (%) - 14.7757(μm)
Refractive Index (R)	: Crystal struvite[Crystal struvite(1.500 - 0.000i),Water(1.333)]		: (9)90.00 (%) - 20.8801(μm)
Refractive Index (B)	: Crystal struvite[Crystal struvite(1.500 - 0.000i),Water(1.333)]		
Material	: Mg NH4 PO4		
Source	: fertilizer		
Sample Number	: 1		
Test or Assay. Number	: 1		

Diameter (μm)	ASTM Mesh	Frequency %	Cumulative %
20.000	635	1.840	89.595
25.000	500	2.156	91.436
32.000	450	2.152	93.592
38.000	400	1.991	95.744
45.000	325	1.253	97.735
53.000	270	0.692	98.988
63.000	230	0.287	99.680
75.000	200	0.033	99.967
90.000	170	0.000	100.000
106.000	140	0.000	100.000
125.000	120	0.000	100.000
150.000	100	0.000	100.000
180.000	80	0.000	100.000
212.000	70	0.000	100.000
250.000	60	0.000	100.000
300.000	50	0.000	100.000
355.000	45	0.000	100.000
425.000	40	0.000	100.000
500.000	35	0.000	100.000
600.000	30	0.000	100.000
710.000	25	0.000	100.000
850.000	20	0.000	100.000
1000.000	18	0.000	100.000
1180.000	16	0.000	100.000
1400.000	14	0.000	100.000
1700.000	12	0.000	100.000
2000.000	10	0.000	100.000
2360.000	8	0.000	100.000
2800.000	7	0.000	100.000
3350.000	6	0.000	100.000
4000.000	5	0.000	100.000

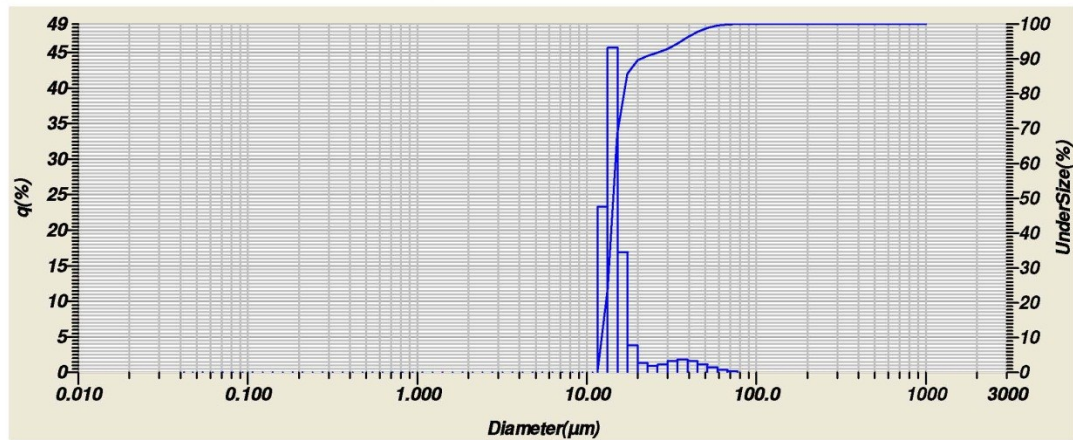


Figure A13 Particle Size Distribution – Time = 40min

HORIBA Laser Scattering Particle Size Distribution Analyzer LA-950

Sample Name	: Crystal Struvite	Median Size	: 14.59532(μm)
ID#	: 201611241315302	Mean Size	: 18.04835(μm)
Data Name	: 201611241315302	Std.Dev.	: 7.6403(μm)
Transmittance(R)	: 98.3(%)	Geo.Mean Size	: 16.0458(μm)
Transmittance(B)	: 98.9(%)	Geo.Std.Dev.	: 1.3630(μm)
Circulation Speed	: 5	Mode Size	: 16.2096(μm)
Agitation Speed	: 3	Span	: OFF
Ultra Sonic	: OFF	Diameter on Cumulative %	: (2)10.00 (%) - 12.4811(μm)
Form of Distribution	: Manual		: (4)30.00 (%) - 13.7419(μm)
Distribution Base	: Number		: (6)60.00 (%) - 15.0417(μm)
Refractive Index (R)	: Crystal struvite[Crystal struvite(1.500 - 0.000i),Water(1.333)]		: (9)90.00 (%) - 26.1480(μm)
Refractive Index (B)	: Crystal struvite[Crystal struvite(1.500 - 0.000i),Water(1.333)]		
Material	: Mg NH4 PO4		
Source	: fertilizer		
Sample Number	: 1		
Test or Assay. Number	: 1		

Diameter (μm)	ASTM Mesh	Frequency %	Cumulative %
20.000	635	2.595	86.944
25.000	500	3.610	89.539
32.000	450	3.198	93.149
38.000	400	2.093	96.347
45.000	325	0.870	98.440
53.000	270	0.437	99.311
63.000	230	0.222	99.748
75.000	200	0.030	99.970
90.000	170	0.000	100.000
106.000	140	0.000	100.000
125.000	120	0.000	100.000
150.000	100	0.000	100.000
180.000	80	0.000	100.000
212.000	70	0.000	100.000
250.000	60	0.000	100.000
300.000	50	0.000	100.000
355.000	45	0.000	100.000
425.000	40	0.000	100.000
500.000	35	0.000	100.000
600.000	30	0.000	100.000
710.000	25	0.000	100.000
850.000	20	0.000	100.000
1000.000	18	0.000	100.000
1180.000	16	0.000	100.000
1400.000	14	0.000	100.000
1700.000	12	0.000	100.000
2000.000	10	0.000	100.000
2360.000	8	0.000	100.000
2800.000	7	0.000	100.000
3350.000	6	0.000	100.000
4000.000	5	0.000	100.000

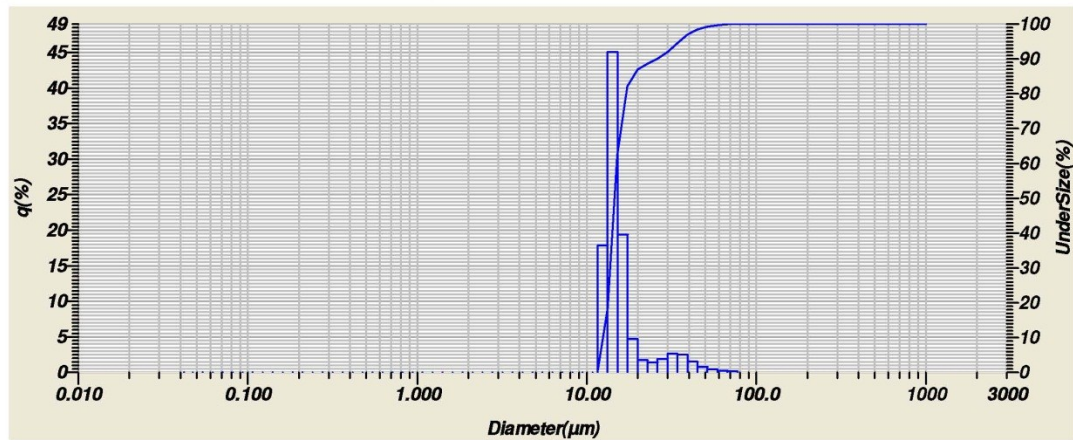


Figure A14 Particle Size Distribution – Time = 50min

HORIBA Laser Scattering Particle Size Distribution Analyzer LA-950

Sample Name	: Crystal Struvite	Median Size	: 12.31608(μm)
ID#	: 201611241325303	Mean Size	: 17.22932(μm)
Data Name	: 201611241325303	Std.Dev.	: 9.7677(μm)
Transmittance(R)	: 99.2(%)	Geo.Mean Size	: 13.7650(μm)
Transmittance(B)	: 99.4(%)	Geo.Std.Dev.	: 1.4689(μm)
Circulation Speed	: 5	Mode Size	: 14.9975(μm)
Agitation Speed	: 3	Span	: OFF
Ultra Sonic	: OFF	Diameter on Cumulative %	: (2)10.00 (%) - 10.2794(μm)
Form of Distribution	: Manual		: (4)30.00 (%) - 11.2914(μm)
Distribution Base	: Number		: (6)60.00 (%) - 12.8473(μm)
Refractive Index (R)	: Crystal struvite[Crystal struvite(1.500 - 0.000i),Water(1.333)]		: (9)90.00 (%) - 24.3420(μm)
Refractive Index (B)	: Crystal struvite[Crystal struvite(1.500 - 0.000i),Water(1.333)]		
Material	: Mg NH4 PO4		
Source	: fertilizer		
Sample Number	: 1		
Test or Assay. Number	: 1		

Diameter (μm)	ASTM Mesh	Frequency %	Cumulative %
20.000	635	2.446	87.874
25.000	500	3.705	90.320
32.000	450	2.239	94.024
38.000	400	1.335	96.263
45.000	325	0.784	97.598
53.000	270	0.621	98.381
63.000	230	0.488	99.003
75.000	200	0.363	99.490
90.000	170	0.147	99.853
106.000	140	0.000	100.000
125.000	120	0.000	100.000
150.000	100	0.000	100.000
180.000	80	0.000	100.000
212.000	70	0.000	100.000
250.000	60	0.000	100.000
300.000	50	0.000	100.000
355.000	45	0.000	100.000
425.000	40	0.000	100.000
500.000	35	0.000	100.000
600.000	30	0.000	100.000
710.000	25	0.000	100.000
850.000	20	0.000	100.000
1000.000	18	0.000	100.000
1180.000	16	0.000	100.000
1400.000	14	0.000	100.000
1700.000	12	0.000	100.000
2000.000	10	0.000	100.000
2360.000	8	0.000	100.000
2800.000	7	0.000	100.000
3350.000	6	0.000	100.000
4000.000	5	0.000	100.000

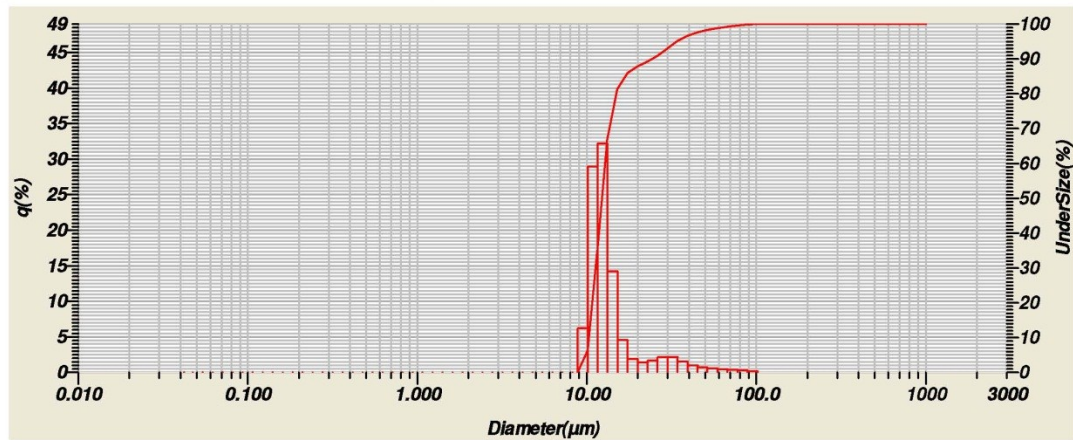


Figure A15 Particle Size Distribution – Time = 60min